Studies of Intermolecular Interactions

by

Karen L. Randall

A Thesis submitted in conformity with the requirements
for the Degree of Doctor of Philosophy in the
Graduate Department of Chemistry at the
University of Toronto

Studies of Intermolecular Interactions

Karen L. Randall

A Ph.D. thesis submitted to the Department of Chemistry at the Unversity of Toronto, 1997

In this thesis results from three separate experiments are reported. In the first experiment, the resolved fluorescence spectra of I_2, clustered with Ar, Kr and Xe and excited at 193 nm to the first ion pair manifold is measured. In Ar and Kr clusters, a broad, featureless emission band is seen, which shifts to lower energies as the cluster size increases. In Xe clusters, this band is not observed: there is very efficient quenching of all emission. Under some expansion conditions, XeI^* excimer emission is observed with a 2-photon dependence on the intensity of the 193 nm excitation laser. These results are all explained by a model in which excitation of I_2 into the ion pair manifold is followed by a harpooning-type electron transfer and formation of an excited charge transfer complex between I_2 and a rare gas atom.

In the second experiment, emission from ion-pair states of I_2 is observed when HI clusters are photolyzed at 248 nm. The emission depends quadratically on the laser intensity and quartically on the stagnation pressure of neat HI. The results strongly suggest that the four-center photoinduced reaction $(HI)_2 \rightarrow H_2 + I_2^*$ takes place in HI clusters, followed by excitation of the I_2^* to the ion-pair levels.

The third experiment studies the scattering of an atomic beam of helium from the surface of an aligned nematic liquid crystal film (4'-pentyl-4-cyano biphenyl, 5CB). Collisions of atoms with the surface initiate a transient loss of order in the film. The

magnitude of this change depends on the momentum direction of the atomic beam with respect to the liquid crystal alignment director. The effect is significantly more pronounced when the incoming beam is perpendicular to the director than when it is parallel. This anisotropy may be due to a more efficient alignment-changing torque exerted by He atoms colliding perpendicular to the long axis of the 5CB molecules.

Acknowledgements

There are many people who have contributed to the completion of this thesis, it would be impossible for me to mention everyone to whom I am thankful. Some of the people to whom I am the most indebted are:

- My supervisor, Jamie Donaldson, for all the time he spent teaching me the mysteries of chemistry and spectroscopy; and for giving me an interesting set of projects to work on.
- Cynthia Goh for giving me the chance to work in her group and for getting me to come to the University of Toronto in the first place.
- The University of Toronto for providing me with an Open Fellowship.
- Dr. Elizabeth Bishenden for answering all of my questions no matter how trivial; and for always coming up with the low tech solution to all of my high tech problems.
- Yibing Fan for teaching me how to run the cluster experiments and building the liquid crystal experimental chambers.
- Olivier Michel for his contribution to the liquid crystal experiments.
- The Tree Fort Gang (David, David, Steve, Rob, and Stephen) for giving me a new home, helpful advice (professional and personal), and for all the abuse ("The abuse is always free.").
- All the members of the Devil House (Darrick, Richard, Marcel, Erica, Andrew, Emmanuel, Tanya, and Miloš) for all the good times we had and the lively conversations/debates. Especially, Erica and Tanya for all the late evenings of "girl talk".
- Martin Moskovits and Sue McClelland for their advice in times of crisis.
- My family for their love, support, and understanding. I specially acknowledge my grandmother, Grace Sorensen, whose unwavering love will be a source of strength for me throughout my life. It is to her that this thesis is dedicated.
- Miloš, my future husband, in the completion of this thesis you were in turns my computer consultant, proofreader, graphic artist, secretary, psychiatrist, cook, and housekeeper. My life was never so rich before I met you. I look forward to facing new challenges with you.

Contents

List of Figures

List of Tables

Chapter 1

Effects of intermolecular interactions on chemistry

1.1 Historical background

The idea that molecules are indivisible point sources of attractive and repulsive intermolecular forces was first formulated by Boscovich in 1783[1]. His theory was that at small separation the molecules repel one another and as the separation increases the attractive and repulsive forces alternate a number of times. By the mid-nineteenth century, the modern view that molecules repel one another at short distances and attract one another at long distances became established[2].

The kinetic theory of gases describes a gas as a large number of sub-microscopic particles in rapid motion which interact with one another. Initially, the molecules were assumed to be a perfect spheres which only interact during contact with one another. Maxwell incorporated into the kinetic theory of gases an intermolecular force between molecules based on incorrect measurements of the temperature dependence of viscosity between molecules[2]. As a result of the incorrect data, Maxwell included a repulsive force which decayed with the inverse fifth power of the intermolecular

separation.

In 1873, van der Waals modeled gas molecules as impenetrable rigid spheres surrounded by an attractive force field[1]. He then showed that the pressure exerted by this gas was less than that for a gas whose molecules are non-interacting points, because the field reduces the velocity of the molecules which collide with the wall. Furthermore, the non-zero volume of the gas molecules reduces the volume available for molecular motion[1]. The importance of this formulation is that, in contrast to the ideal gas theory, it predicts a gas-liquid transition and a critical point for a pure substance. Thus van der Waals showed that the existence of condensed phase of matter is the result of the attractive forces between molecules and the small compressibility of the condensed phases results from repulsive forces which act at short range. Since the end of the nineteenth century considerable work has gone into determining the connection between intermolecular forces and bulk properties of matter[1].

1.2 Intermolecular energy

The force between atoms and/or molecules is related to the potential energy function:

$$F = -\frac{dU(r)}{dr}$$

where U is the intermolecular pair potential energy and r is the distance between the two species. The simplest system is that consisting of two interacting atoms. When two atoms (a and b) are at infinite separation they do not interact. The total energy of the system, E_{tot}, is the sum of the energies of the individual atoms: $E_{tot}(\infty) = E_a + E_b$. As the separation decreases to some finite distance, r, the interaction between the atoms provides an additional contribution to the total energy of the system. If this energy depends only on the separation of the two atoms, the total energy becomes $E_{tot}(r) = E_a + E_b + U(r)$. This equation may be written in terms of the intermolecular pair potential:

$$U(r) = E_{tot}(r) - E_a - E_b = E_{tot}(r) - E_{tot}(\infty).$$

The intermolecular pair potential describes the change in the energy of the two atom system from that of the two atoms infinitely separated.

The energy of interaction between the two atoms arises from the electrical forces between the charged entities which make up the atoms. In the semi-classical picture of an atom, the electrons oscillate rapidly about the nucleus. The electric forces associated with the electron must fluctuate on the time scale of the electron motion. Since the time scale on which the atoms move is long compared to the time scale of the electron motion, the Born-Oppenheimer approximation states that the nuclei can be considered stationary with respect to the electron motion. When this approximation is valid, the force between the atoms at a given separation is the sum of the forces between the nuclei at that separation and an average over the forces resultant from the fluctuation of the electrons.

For closed shell systems, the general form of the intermolecular potential energy function, $U(r)$, is shown in Figure 1.1. This potential is characterized by two important values: r_m, the separation at which the energy attains its minimum value, and $-\varepsilon$, the minimum energy. The intermolecular potential is the sum of a strong repulsive force at short distances and an attractive force at long distances. The source of the repulsive potential is the overlap of the electron clouds at small internuclear separation. The Pauli exclusion principle prohibits electrons in closed shell systems from occupying the same region. This leads to a distortion in the electron clouds, which leaves the nuclei incompletely shielded from one another. As a result the nuclei exert a repulsive force on each other.

The long range attractive potential, U_{attr}, is the consequence of the summation of several electrostatic forces and is generally written as

$$U_{\text{attr}} = U_{\text{el}} + U_{\text{ind}} + U_{\text{disp}} + U_{\text{I}} \tag{1.1}$$

where the first three terms on the right hand side are potentials due to the electrostatic energy, the induction energy, and the dispersion energy, and the fourth term is the ionic energy. If one or both of the molecules in the pair are ions then the ionic potential term, U_{I}, accounts for the interaction between the two ions or between an

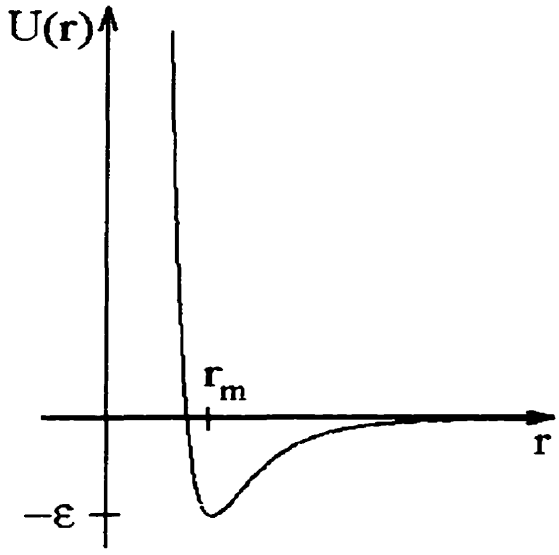

Figure 1.1: *Intermolecular potential energy*

ion and a neutral molecule.

In the rest of this section, the total intermolecular potential for neutral molecules in their ground state with axially symmetric charge distributions will be shown, after which the additional terms necessary to account for the presence of a charged species will be discussed. For molecules at separation, r, which each possess a permanent dipole moment, one component of the interaction potential arises from electrostatic interaction between the dipole moments, as follows

$$U_{\rm el}(r,\theta_1,\theta_2,\phi) = \frac{-\mu\mu'}{4\pi\epsilon_0 r^3}\zeta(\theta_1,\theta_2,\phi)$$

where

$$\zeta(\theta_1,\theta_2,\phi) = 2\cos\theta_1\,\cos\theta_2 - \sin\theta_1\sin\theta_2\cos\phi$$

describes the dependence on the orientation, as indicated in Figure 1.2, and μ and μ' represent the dipole moments of the first and second molecules respectively. This equation is strictly true only in the limit of large separation. If all orientations are equally probable, then the average of this function over all orientations is zero. However, the probability of observing a configuration of energy U is proportional to the

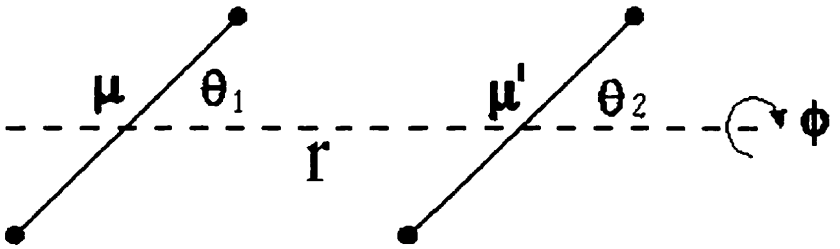

Figure 1.2: *The interaction of two dipolar molecules*

Boltzmann factor, $e^{-U/kT}$, where k is Boltzmann's constant and T is the temperature. This factor preferentially weights configurations with a lower energy. The Taylor polynomial expansion for the Boltzmann factor is

$$e^{-U/kT} = 1 - \frac{U}{kT} + \frac{1}{2}\left(\frac{U}{kT}\right)^2 - \ldots$$

If the temperature is sufficiently large, this can be approximated by the first two terms on the right hand side. Then the potential energy averaged over all angles becomes

$$U_{el}(r) = \int \frac{-\mu\mu'}{4\pi\epsilon_0 r^3}\zeta(\theta_1,\theta_2,\phi)d\Omega - \int \left(\frac{-\mu\mu'}{4\pi\epsilon_0 r^3}\zeta(\theta_1,\theta_2,\phi)\right)^2 d\Omega \,.$$

Upon integrating this expression the Boltzmann weighted average of the potential for significantly high temperatures is

$$< U_{el} > = -\frac{2}{3}\frac{\mu^2\mu'^2}{(4\pi\epsilon_0)^2 kT\, r^6} + \ldots$$

This potential is attractive and inversely proportional to the sixth power of the internuclear separation.

The interaction between one molecule with a permanent dipole moment and one without a permanent dipole moment results in an induced dipole moment in the second molecule. The energy of interaction between the dipole and the induced dipole is given by

$$U_{ind} = -\frac{1}{2}\frac{\alpha'\mu^2\,(3\cos^2\theta + 1)}{(4\pi\epsilon_0)^2\, r^6}$$

where μ is the dipole moment of the first molecule, α' is the polarizability of the second molecule, and the angle, θ, is shown in Figure 1.3. This potential is attractive for all configurations and inversely proportional to the sixth power of the intermolecular separation. When this potential is averaged over all possible orientations using a Boltzmann weighting, the potential becomes

$$< U_{ind} > = -\frac{\alpha' \mu^2}{(4\pi\epsilon_0)^2 r^6} + ...$$

The leading term for this orientation averaged potential is not temperature dependent.

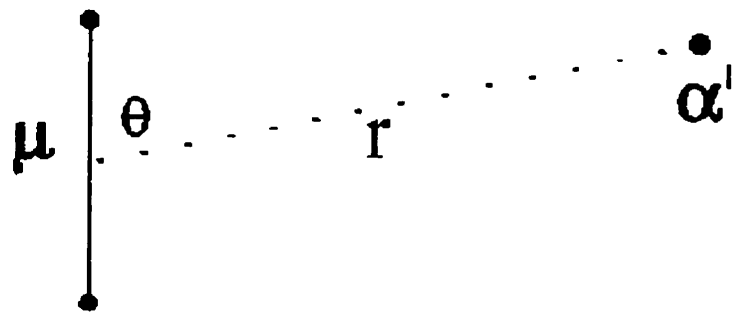

Figure 1.3: *Interaction of a dipolar molecule with a non-polar molecule*

The third attractive potential term between two spherical molecules is the dispersion term. The interaction between two spherically symmetric atoms possessing no permanent electric dipole or higher order moments arises from the dispersion energy. The dispersion energy arises from the instantaneous dipoles of the molecules. One formulation[3] of the dispersion energy is

$$U_{disp} = -\frac{3}{2}\left(\frac{(IP)(IP')}{(IP+IP')}\right)\frac{\alpha\alpha'}{(4\pi\epsilon_0)^2 r^6}$$

where IP and IP′ are the ionization potentials of the two molecules. The dispersion potential is also attractive and inversely proportional to the sixth power of the intermolecular separation. For non-spherical molecules the dispersion energy is also a function of the relative orientations of the molecules. For spherically symmetric molecules, the total long range attractive potential of neutral species is inversely proportional to the sixth power of the internuclear separation.

The short range repulsive potential is much more difficult to quantify. This potential originates from the partly incomplete screening of the nuclei which results from the overlap of the electron clouds at short distances and the repulsion between the electrons. This results in a large perturbation to the electron distribution of the separated molecules. As well, the usual expansions used for long range forces are not valid, when the separation between the molecules is not large compared to the separation between the nucleus and the average position of the electrons. One form for the repulsive energy[4] is given by

$$U_{rep} = Ae^{-Br}$$

where A and B are empirical parameters.

The short range repulsive and long range attractive forces have been separately obtained. However, these methods cannot be used directly to study the intermediate regions of separation by adding the two contributions together. The inability to obtain a proper potential has led to a heuristic approach to determine the potential energy between two molecules.

The simplest function views the molecule as a hard sphere of diameter, σ, this leads to a potential energy

$$U(r) = \begin{cases} \infty & r \leq \sigma \\ 0 & r > \sigma \end{cases} .$$

This form of the potential is generally too simple to model real systems. A model which is more accurate is the Lennard-Jones potential. It is the most frequently used model and has the form

$$U(r) = \varepsilon \left\{ \frac{6}{n-6} \left(\frac{r_m}{r}\right)^n - \frac{n}{n-6} \left(\frac{r_m}{r}\right)^6 \right\}.$$

This potential has the general characteristics of the true intermolecular potential energy. There is a short-range repulsive term combined with a long-range attractive term. The sum of the two curves shows a minimum at r_m, where the energy is $-\varepsilon$, as was shown in Figure 1.1. The attractive component of the potential is based on the dispersion potential. The mathematical form of the repulsive potential, however, has

no justification. The most common form of the Lennard-Jones potential used is with n = 12, for which the potential simplifies to

$$U(r) = 4\varepsilon\left\{\left(\frac{\sigma}{r}\right)^{12} - \left(\frac{\sigma}{r}\right)^{6}\right\}$$

where $\sigma = 2^{-1/6}r_m$ is the intermolecular separation for which the energy is zero. The values for σ and ε are determined empirically. Many other simple forms for the intermolecular pair potential have been used. No form has reproduced all of the experimental data over a wide temperature range. this indicates that none of these forms represents the exact potential. For modeling the interatomic pair potential for rare gas atoms. the Lennard-Jones potential is a reasonable approximation to use and the coefficients have been determined for many species[5].

If one or both of the pair of species is charged. then there are additional long range interactions between the molecules which must be included in the interaction potential. The potential between two ions is dominated by the Coulomb potential

$$U_c = \frac{qq'}{4\pi\epsilon_o r}$$

where q and q' are the charge on the two species and r is the intermolecular separation. This potential is attractive if the two species are oppositely charged and repulsive if the species have the same charge. If only one of the species of the pair potential is an ion. then the ion will interact with the dipole moment of the second species. In this case the intermolecular potential is given by

$$U_{I-D} = \frac{q\mu\cos\theta}{4\pi\epsilon_o r^2}$$

where μ is the dipole moment of the second species and the angle θ is defined in Figure 1.4. If the neutral species does not have a dipole moment. then the dominant term in the interaction will be that between the ion and the induced dipole

$$U_{I-ID} = \frac{\alpha q^2}{2(4\pi\epsilon_o)^2 r^4}$$

where α is the polarizability of the neutral species. There are also additional higher order contributions to the potential which result from the presence of a charged

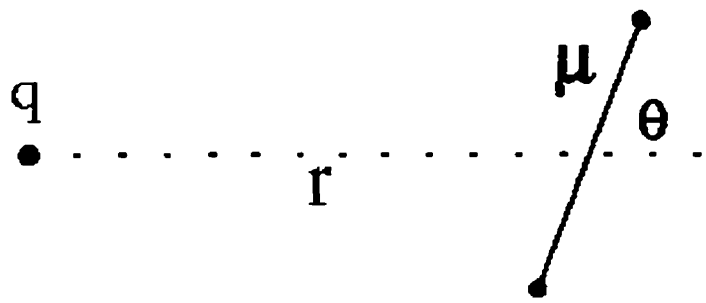

Figure 1.4: *Interaction of an ion with a dipolar molecule*

species, which need not be considered here because their contributions to the potential is often negligible.

As was initially stated, the total energy of the system at separation, r, is given by $E_{tot}(r) = E_a + E_b + U(r)$. Therefore, the total energy of the system is also determined by the initial energy of the two molecules depending on their initial electronic, vibrational and rotational energy. A full description of the energy levels of a two atom system includes calculations of each of the possible energy states.

In the above discussion, only interactions between pairs of molecules have been considered. The total interaction energy between of a group of more than two molecules is equal to the sum of the pairwise potentials plus an additional term. The pairwise potentials are the dominant term in the intermolecular interactions. As a result, in this thesis the calculations of potential energies of two species interacting with a single solvent atom will consist only of adding pairwise potentials. It should be noted that the true intermolecular potential well is deeper than the calculations given here.

When a pair of molecules are in a liquid the electromagnetic interaction energy of the molecules is modified by the solvent molecules. The electrostatic energies of interaction are reduced by a factor ϵ_s, the dielectric constant of the solvent. This factor takes into account all of the interactions between the pair of molecules and the neighboring solvent molecules. In the calculations presented here for the potential

energies for two species in a "fully solvated" environment, the potential due to the dielectric constant of the solvent will be calculated.

1.3 Synopsis of thesis

The underlying focus of this research project is to understand the dynamics of chemical reactions occurring at a liquid surface. In order to unravel the dynamics it is important first to understand the effect of the solvent medium on the reacting partners and the dynamics of collisions of gas phase molecules with a surface in the absence of reaction. Upon acquiring some understanding of these more simple processes one can then address the complex problem. Understanding the dynamics of chemical reactions occurring at surfaces is important for many areas of study including chemical reactions in clouds[6].

The initial work involved studying the interactions between reactant molecules and the surrounding solvent medium. The effect of the solvated environment on the energetics of a probe molecule, generally in the absence of chemical reaction, was initially studied in clusters. Clusters are a useful medium in which to study the effects of solvation since the size of the cluster and hence the number of solvating molecules may be controlled.

The resolved fluorescence spectra of iodine molecule in rare gas cluster, which have been excited to their ion pair state, I_2^{ip}, was measured. This system was chosen as a model system to study for two reasons: the spectroscopy of I_2^{ip} is known in the gas phase[7][8] as well as in the condensed phase (matrix)[9], and the use of rare gas atoms as the solvating medium simplifies the solvation mechanism such that calculations can be made of the potential energy surface. In these experiments the cluster size, and hence degree of solvation, was changed to observe the shift of the emission spectrum from that of the isolated gas to that of the fully solvated system. An interesting finding of the experiment is that XeI^* is produced by reactions between I_2 and Xe in clusters by a different mechanism than that which occurs in the gas phase.

In order to further study the effects of solvation on chemical reaction, clusters of only HI were photolyzed at 248 nm and the resolved emission from the I_2^* product was measured. The dependence of the the reaction probability on the cluster size was determined. Previously the H_2[10] and I_2[11][12][13] products have been measured. However, this is the first work in which the I_2^* product was measured directly. In the work by Young and co-workers[11][12] they determined that ground state I_2 is formed when two photons break two HI bonds. In previous work from this group[13] only the I_2 formed in the ground state was measured. The present measurements provide a more complete understanding of this system. Furthermore, the dependence of the emission of I_2^* on the cluster size reveals insight into the role of the cluster size on the reaction mechanism.

In order to understand the processes which occur at a liquid surface, the dynamics of gas phase molecules colliding with a liquid crystal surface were studied by measuring the change in the polarization of light transmitted through the liquid crystal as a function of time. Collisions between gas and condensed phase molecules mediate energy transfer, mass transport and chemical reactions between the two phases. Understanding the processes involved in the collision of a gas phase molecule with a liquid surface in itself is important to many processes such as the uptake of pollutants by water droplets in clouds, gas phase chromatography and heterogeneous catalysis[14]. After colliding with the surface the molecule may scatter inelastically from the surface or bind momentarily to the surface before desorbing back into the gas phase or dissolving into the bulk. If it has been trapped at the surface the molecule may desorb, remain adsorbed at the surface or diffuse into the bulk. The molecule may also react with liquid molecules at the surface or in the bulk.

The liquid crystal 4'-pentyl-4-biphenylcarbonitrile (5CB) was chosen as the surface constituent. There are a number of reasons that using a liquid crystal and specifically 5CB is beneficial. The reasons why 5CB is useful in brief are: its nematic isotropic phase transition is at a convenient temperature, it has a low vapor pressure, the director axis is simple to define, and the molecules are birefringent. In these experiments it is the change in the polarization retardation of an aligned liquid crystal with gas

beam impact which is measured. It is found that the orientation of the liquid crystal molecules at the surface determines the ability of the gas beam to influence the observed polarization signal.

Chapter 2

van der Waals clusters

2.1 Clusters

Clusters are finite aggregates whose composition can be changed by adding or removing units of the species of which they are comprised. They are entities which have neither the well defined compositions, geometries, and strong bonds of conventional molecules nor the boundary-independent properties of bulk matter. Clusters provide a unique physical environment which is intermediate between that of an isolated molecule and a macroscopic system.

The bonding of the molecules within clusters is determined by the type of atoms or molecules of which the cluster is composed. Clusters are categorized based on the type of bonding: those held together by "weak interactions" - dispersive and weak electrostatic forces as well as hydrogen bonding - and "strong interactions" - ionic bonds, chemical bonds, and metallic bonds. This thesis will only be concerned with van der Waals clusters which are held together by dispersive and weak electrostatic forces. These clusters typically have binding energies less than 0.1 eV. As a result of the small binding energy clusters generally do not have long lifetimes in equilibrium environments where random thermal collisions take place.

Clusters may be neutral or charged; insulating, conducting or semiconducting; liq-

uid, solid or intermediate between liquid and solid; chemically inert or highly reactive. One of the interesting features of clusters is that all of these properties of clusters depend on the size of the cluster. By increasing the cluster size the properties change from those of an isolated molecule to the bulk value. One goal of cluster science is to determine how many atoms or molecules are required for a substance to display bulk phase properties, such as ionization potential, specific heat, and conductivity. An interesting finding is that the size of the cluster at which a particular property reaches its bulk limit is determined by that particular property's sensitivity to the proximity of the surface[15]. Van der Waals forces have a profound affect on bulk properties of matter, even at temperatures where bound van der Waals molecules are unstable.[4]

One difficulty in the study of clusters containing more than a few atoms is measuring the actual cluster size in beams produced by free jet expansions. The method for obtaining information on the average cluster size of Ar clusters used in this work was to compare our expansion conditions to those for which Fargas *et al.*[16][17] made electron diffraction measurements. Fargas *et al.* expanded neat argon in a free jet at a number of stagnation pressures. They took photographs of the electron diffraction patterns resulting from the clusters within the gas jet. The average cluster size was determined by comparing these photographs to calculated diffraction patterns based on models of the cluster geometry for a range of cluster sizes. Although it was not done for these experiments, the results of Fargas, *et al*[16][17] can be generalized to different expansion conditions and different carrier gases by using the scaling laws derived by Hagena[18].

2.2 Solvation in clusters

Solvation is defined[4] as the lowering of the potential energy of a molecule or atom as a result of interactions with neighboring atoms or molecules. In the condensed phase each molecule is surrounded by a substantial number of relatively near neighbors

and its potential energy surface is the result of all of the interactions among all of the molecules. The potential energy surface is not only a summation over all of the two body interactions, but also of the interactions due to three molecules interacting with each other as well as to higher order interaction terms. The bonding within clusters is similarly a summation over two, three, and more body interactions. However, the primary contribution to the intermolecular interactions is the two body interactions[1].

The interaction between two gas phase molecules is described in terms of the intermolecular potential between the two molecules. Within a gas phase system molecules interact and exchange energy through isolated binary collisions. In condensed phase systems, energy flows between the molecules via the weak bonds between the molecules. Condensed phase systems are characterized by solvent shifts, diffusion control, and caging effects[19]. Solvent shifts describe how the absorption and emission differ for the condensed phase species compared to that for an isolated molecule. Diffusive systems are controlled by the random thermal motions of the molecules within the system and are at equilibrium. The cage effect is the process in which the solvent prevents direct dissociation of a molecular solute and promotes geminate recombination.

Clusters may be homogeneous (composed of only one kind of atom or molecule) or heterogeneous (composed of two or more types of atoms or molecules). If one of the species is present in a very low concentration in the cluster then that species is called the guest species and the cluster is called a doped cluster. The primary species is often referred to as the solvent. Systems such as this are used to study the effect of solvation on a specific (guest) molecule. The effect of the intermolecular forces between the guest and the solvent molecules can be studied by measuring the change in the emission or absorption spectrum of the guest species. The solvent allows intramolecular energy redistribution of the guest species by transfering energy into vibrational modes of the van der Waals bonds between the guest and the solvent molecules. Interstate electronic relaxation of the guest molecule may occur as a result of the solvent molecule changing the symmetry of the system and allowing access

to previously symmetry-forbidden states. Noble gas clusters with a probe molecule are used in the work here, because the interaction potentials are well known, the production is simple, and there exists accurate information on their solid, liquid and gas phases.[15]

Caging effects have been observed in matrices[20][21], solutions[22][23][24], dense gases[25], and van der Waals clusters[26][27][28]. The caging of halogen molecules which are excited to a repulsive potential energy surface or above the dissociation limit of a bound state is very effective in the condensed phase. It was assumed[20][21] that the halogen atoms born on the repulsive molecular potential lose their nascent kinetic energy by collisions with the repulsive wall of the cage, such that they are prevented from dissociation. The relaxed atoms then recombine within the cage[21]. However, Valentini and Cross[27] observed a cage effect under collision-free conditions. They observed the hindered dissociation of I_2·Ar. Although it was not known at the time of their experiments, the geometry of the I_2·Ar cluster is T-shaped, thus a collision of the Ar atom with a dissociating I atom would not be possible based on conservation of angular momentum laws. Valentini and Cross[27] proposed that energy transfer to the van der Waals bond followed by its dissociation was responsible for stabilizing the normally dissociative iodine molecule.

2.3 Reactions in clusters

The effects of a solvent on a chemical reaction are either chemical or physical. A chemical effect means that the solvent molecule participates directly in the reaction, and appears in the stoichiometric equations as either a reactant or a product. The solvent molecule may also affect a reaction physically either by altering the collision distribution or by acting as a catalyst for the reaction. If the effect is catalytic, the solvent appears in the kinetic equations but not in stoichiometric equations. By adding the solvent molecules in the cluster one at a time, the influence of the solvent on the chemical reactivity of the constituent molecules can be determined[29].

Clusters allow liquid- or solid-phase reactions to be studied under controlled conditions.[30] By varying the number of atoms in the complex, the effects of solvents may be studied in detail. The existence of a solvating molecule opens up new channels for energy transfer to van der Waals vibrational modes of the cluster. Molecules other than the reactants may act as a catalyst by changing the reaction probability or the reaction rate. The presence of the solvent can also relax restrictions due to momentum and energy conservation laws, by opening up new channels for momentum and energy transfer.

Examining chemical reactions on a molecular level is a major focus of modern physical chemistry[31]. To understand a chemical reaction on a molecular level, the internal and translational energy of the reactants and products, the impact parameter and orientation of the reacting species, the transition state of the reaction and how each of these properties changes with solvation must be known. Clusters formed in supersonic expansions allow many of these characteristics to be studied. For small clusters the number of molecules, the geometry and the energy levels available to the molecules within the cluster can be determined[32].

In order to gain information about chemical reactions several groups have designed experiments in which each reactant is oriented relative to a common set of fixed axis and therefore relative to each other[33][34]. These experiments are both difficult to perform as well as limited in which reactants can be used. Van der Waals clusters have proven to be an easier and better controlled environment for this type of experiment. Using bimolecular van der Waals clusters with a well defined equilibrium geometry, a reaction in which the initial orientation and energy are known can be studied. The reactions are initiated either by photoexcitation of one component[35][36] or photodissociation of one component[37][38]. In experiments where one component is photodissociated; one fragment of the dissociated molecule often approaches the second component of the cluster with a defined impact parameter and velocity. To determine the effect of the alignment on the reactions, comparisons are made with bulk reactions of the same species. In experiments with CO_2·HBr Wittig and coworkers[37] found very different rotational energy in the products compared to energy

of the products produced in bulk reactions.

Another type of reaction which has been studied in clusters and in condensed phase is harpooning reactions. Harpooning reactions are common between alkali metals and halogen compounds[39]. These reactions are fast exoergic reactions with no minimum energy required for the reaction to occur. The first stage of the reaction is envisaged as the transfer of the valence electron of the alkali metal atoms to the halogen molecule.[39] This transfer is possible even when the reactants are several Angstroms apart, because Coulomb forces are important over a long range. Once the transfer takes place and an ion-pair species, $A^+R_2^-$, is produced, the strongly attractive Coulomb force brings the two ions together. This results in the formation of a stable molecule, AR, and ejection of the R atom. The metal atom uses its valence electron as a 'harpoon' to pull in the halogen molecule. Although this reaction is most typically observed in alkali metal-halogen reactions, it is not limited to such species. In the work presented here a harpooning mechanism is inferred in reactions between iodine molecules and rare gas atoms. The harpooning reaction is written as

$$A + R_2 \longrightarrow (A^+ + R_2^-) \longrightarrow A^+R^- + R.$$

The reaction occurs at the distance at surface crossing between the covalent and ionic surfaces of the reacting species (see Figure 2.1). This same type of reaction has been inferred in systems with halogen molecules in rare gas solids[40], liquids[21], van der Waals clusters[35][36], and dense gas[41][42].

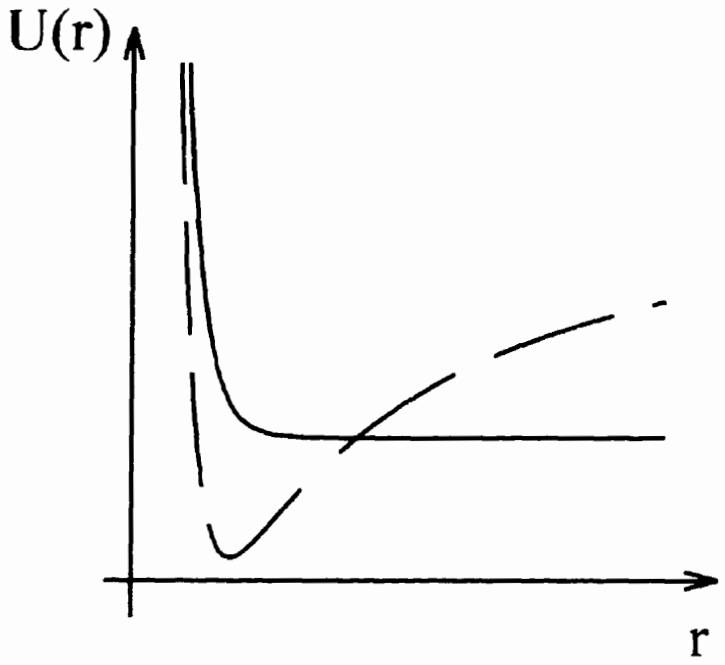

Figure 2.1: *Neutral (solid line) and ionic (dashed line) surface potentials for a harpooning reaction. The electron transfer will occur at the curve crossing, that is where the energy of the neutral potential is equal to that of the ionic potential.*

Chapter 3

Liquid crystals

3.1 Introduction

Understanding the solvation and reaction of gas-phase molecules with the liquid phase is important to many areas of chemistry. A number of groups[43][44][45][46][47] have studied the energy transfer in the scattering of low molecular weight gases off of liquid monolayers and surfaces by measuring the resultant internal or external energy of the scattered species. What is unique and interesting about the experiments performed in this thesis with liquid crystals is that the effect of the collision on the liquid crystal is measured. By measuring a bulk property of the liquid crystal, its polarization retardation[48], the consequence of the collision on the surface may be inferred.

Scattering experiments with liquid crystals can be performed in vacuum since liquid crystals have a low vapor pressure. The surface of the liquid crystal in the vacuum is in a steady state rather than at equilibrium. There is a constant slow rate of evaporation of molecules from the liquid crystal resulting from the vacuum pumping. For the liquid crystal studied in these experiments, 4'-pentyl-4-biphenylcarbonitrile (5CB), the sample loss over the 3-4 hours that the experiments are run is less than three percent. The low vapor pressure reduces the number of collisions of the incident gas molecules with liquid crystal molecules in the gas phase. This in turn means that

the momentum of the gas particles striking the surface is better defined.

The gas beam may affect the optical transmission through the liquid crystal by changing: its thickness, its temperature, its density, or the order parameter by other means than by density or temperature changes. In this chapter, the order parameter will be described and the effects of temperature and pressure on it will be discussed. A description of the effect of the thickness on the optical transmission is found in Apendix B.

3.2 Liquid crystal mesophases

Some organic materials undergo more than one phase transition between their crystalline solid and liquid phases[49][50][51]. Crystalline solid phases have translational and orientational order while liquids are homogeneous and isotropic. The intermediate phases between the solid and liquid phases are called "mesomorphic" phases (or mesophases). Molecules in these mesophases demonstrate translational and orientational order intermediate between those of a crystal and those of an isotropic liquid. The mesophases are divided into disordered crystal mesophases and ordered fluid mesophases based on the type of ordering which they exhibit.

Materials which exhibit a disordered crystal mesophase (also called plastic crystals) are usually composed of spherical molecules in which the barrier to rotation is small compared to the lattice energy[50]. In these materials raising the temperature initially results in attaining a phase in which the molecules are energetic enough to rotate, but not energetic enough to break up the lattice structure. The result is a phase in which the molecules are translationally well ordered but orientationally disordered. Further increasing the temperature results in the molecules becoming energetic enough to destroy the lattice, at which point the molecules enter the isotropic liquid state. Some examples of plastic crystals are solid hydrogen and ammonium halides.

Liquid crystal is the common name for the order fluid mesophase as well as for

molecules which possess an ordered fluid mesophase. Liquid crystals generally consist of elongated molecules for which the barrier to rotation (at least in one axis) is large compared to the lattice energy. In these materials raising the temperature initially results in attaining a phase which shows some degree of rotational order (and in some cases partial translational order) even though the crystal lattice has been destroyed. Further raising the temperature destroys the rotational order and the material becomes an isotropic liquid. Liquid crystals are classified as either lyotropic or thermotropic.

Lyotropic liquid crystals consist of solutions of rod-like entities in an isotropic solvent[52]. The interaction of the rod-like entities with the aqueous solvent that is crucial in proving the stability of the ordered phases[53]. These liquid crystals consist of mixtures of amphiphilic compounds and a polar solvent, frequently water. Amphiphilic compounds are characterized by having within one molecule both hydrophobic and hydrophilic parts. In dilute solution the amphiphilic molecules are randomly distributed throughout the solution. As the concentration of the amphiphilic molecules is increased, the molecules aggregate and form micelles, which have structure. A well known lyotropic liquid crystal is DNA in water.

Materials which exhibit various liquid crystalline phases as a function of temperature are called thermotropic liquid crystals. These molecules are usually organic molecules with axial ratios (the ratio of the length of the molecule to its width) of 4 - 8 and molecular weights on the order of 200 - 500 gm/mol[50]. These molecules show the liquid crystal phase in pure solutions, where each molecule contributes equally to the long range ordering. Examples of thermotropic liquid crystals are pure organic p-azoxyanisole (PAA) and N-(p-methoxybenzylidene)-p'-n-butylaniline (MBBA).

Thermotropic liquid crystalline mesophases are further classified by their degree of translational alignment. The three major mesophases of liquid crystals are smectic, cholesteric, and nematic. Liquid crystals having more than one mesophase between the solid and liquid phases are called "polymorphous". Since raising the temperature of any material decreases the molecular order, the less ordered the mesophase, the higher the temperature.

Nematic liquid crystals have long range orientational order, but no order to the center of mass positions[51] (see Figure 3.1). Due to intermolecular forces between

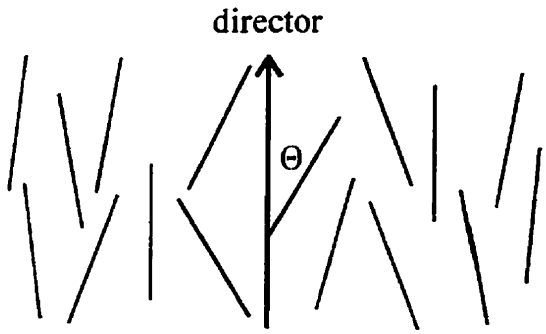

Figure 3.1: *The arrangement of molecules in a nematic liquid crystal mesophase. The director is indicated by an arrow and the orientational angle of a liquid crystal molecule to the director is indicated by the angle* Θ.

the molecules they tend to align parallel to a common axis called a director, $\vec{n}$, which is arbitrary in space. The molecules only rotate freely about the axis of the director. The director states $\vec{n}$ and $-\vec{n}$ are indistinguishable. If the molecules are dipolar there are as many dipoles "up" as there are "down" and the resulting dipole for the system is zero. Nematic phases only occur with materials which do not distinguish "chirality"[51]. This is accomplished when each constituent molecule of the system is achiral (identical to its mirror image) or when the system consists of an even mixture of right- and left-handed chiral species.

The chiral nematic liquid crystal phase is similar to the nematic phase on a local scale, since the orientation with respect to the director is the same[50]. It is similarly fluid-like in having no long range translational order, however, the chiral nematic director is not constant in space; it follows a helix, as shown in Figure 3.2. The structure is periodic along the z-axis. Chiral nematics consist of chiral molecules (different from their mirror image). Chiral nematic liquid crystals are often called cholesteric liquid crystal since most of the molecules of this category are cholesteric molecules such as cholesteryl decanate and cholesteryl nonnoate.

Smectic liquid crystals have layered structures, with well defined inter-layer spacing[49].

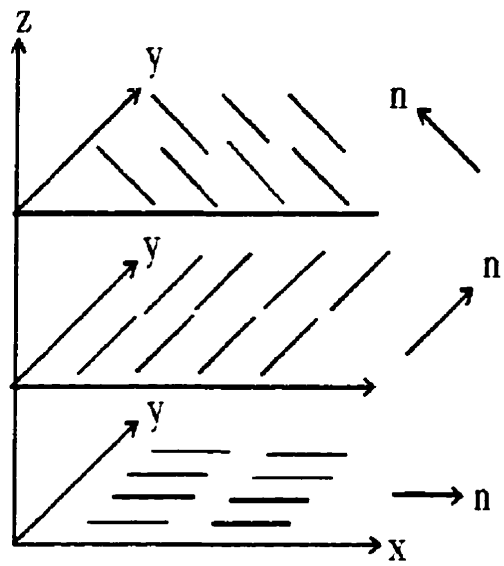

Figure 3.2: *The arrangement of molecules in the cholesteric mesophase. The successive planes have been drawn to indicate the helical rotation of the director and have no physical meaning.*

The ordering for the smectic A liquid crystal is shown in Figure 3.3. The smectic phases are much more viscous than either the nematic or cholesteric liquid crystals as a result of the this ordering[51]. Smectic liquid crystals are further classified by the orientation of the director and the ordering of the molecules within this layered structure. An example of a liquid crystal which exhibits a smectic mesophase is terephthal-bis (-p-butylaniline) (TBBA).

The remainder of this chapter will discuss the characterization of liquid crystals. Only nematic liquid crystals will be considered, since the experimental work used only a nematic liquid crystal.

3.3 The order parameter

The order parameter[49][54][51] is used as a way to quantitatively characterize the alignment of a system. It is defined such that it has a value of unity for a perfectly ordered system and vanishes for a completely isotropic phase. In order to define a

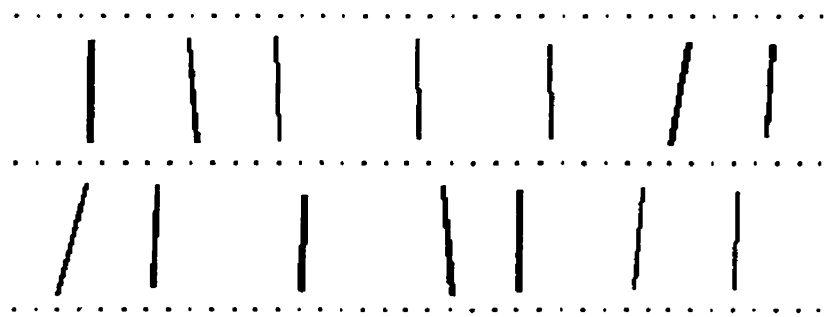

Figure 3.3: *The arrangement of molecules in a smectic A mesophase*

simple order parameter for a nematic liquid crystal, the molecules are considered to be cylindrically symmetric rigid rods and the director axis, $\vec{n}$, is the z-axis. The axis of one rod is defined by the unit vector $\vec{a}$. The polar angles θ and φ are used to define $\vec{a} = (\sin\theta\cos\varphi)\hat{x} + (\sin\theta\sin\varphi)\hat{y} + \cos\theta\hat{z}$. The order parameter, S, is therefore defined as $S = \langle \vec{a} \cdot \vec{n} \rangle$. The alignment of the rods is given by the distribution function $f(\theta,\varphi)\mathrm{d}\Omega$. Since the molecules have complete cylindrical symmetry about the director axis $\vec{n}$, then $f(\theta,\varphi)$ is independent of φ. Also, since the directions n and -n are equivalent $f(\theta) = f(\pi - \theta)$. A function which fulfills the above criterion[51] (gives an order parameter of zero for a completely isotropic system and an order parameter of 1 for a completely aligned system) is

$$S = \frac{1}{2}\left\langle\left(3\cos^2\theta - 1\right)\right\rangle = \int f(\theta)\frac{1}{2}(3\cos^2\theta - 1)d\Omega. \tag{3.1}$$

where the integration is over all of the molecules in the system. The order parameter is equal to $\langle P_2 \rangle$, the second order Legendre polynomial averaged over all of the molecules in the system.

In nematic liquid crystals the temperature affects the order parameter, which in turn changes the refractive index according to the three band model[55]. In this model the density has little effect on the index of refraction. Figure 3.4 shows the temperature dependence of n_e and n_o the extraordinary and ordinary indices of refraction of

5CB as measured by Horn[56].

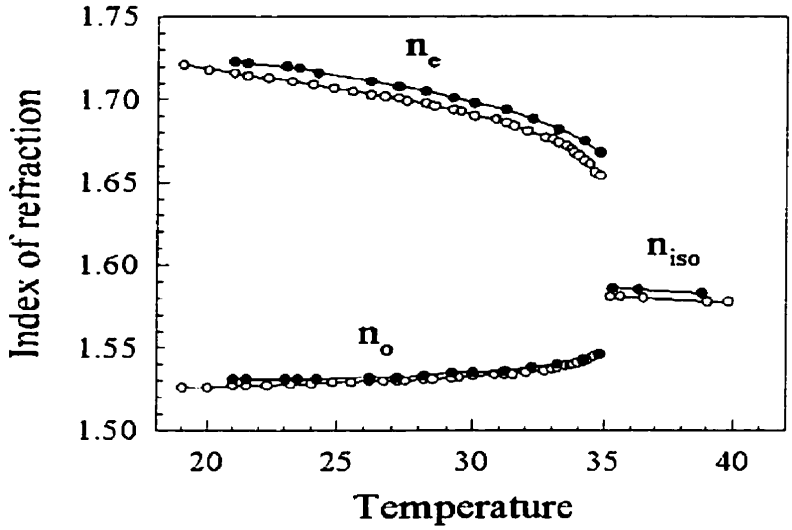

Figure 3.4: *The refractive indices for 5CB measured at 589 nm (•) and at 633 nm (o). The upper curve represents the extraordinary index of refraction, n_e, the lower curve is the ordinary index of refraction, n_o, and the curve on the right hand side, n_{iso}, is the index of refraction for 5CB in its isotropic phase.*

Horn[56] used the Vuks[57] assumption,

$$S = \left(\frac{\bar{\alpha}}{\alpha_{\parallel} + \alpha_{\perp}}\right)\frac{n_e^2 - n_o^2}{\overline{n^2} - 1}$$

where $\overline{n^2} = \frac{1}{3}(n_e^2 + 2n_o^2)$, $\alpha_{\parallel}$ and $\alpha_{\perp}$ are the molecular polarizabilities parallel and perpendicular to the long axis of the molecule and $\bar{\alpha} = \frac{1}{3}(\alpha_e^2 + 2\alpha_o^2)$, to calculate a quantity proportional to the order parameter for 5CB. The order parameter itself could not be calculated since the molecular polarizabilities for 5CB were not at that time known. However, by including in his calculations the Haller and Obert approximation[58],

$$S = \left(1 - \frac{T}{T_{N-I}}\right)^{\beta}$$

where T is the temperature, T_{N-I} is the temperature of the nematic-isotropic transition, and β is a property of the particular liquid crystal used, Horn[56] was able to calculate the order parameter as a function of the index of refraction (see Figure 3.5).

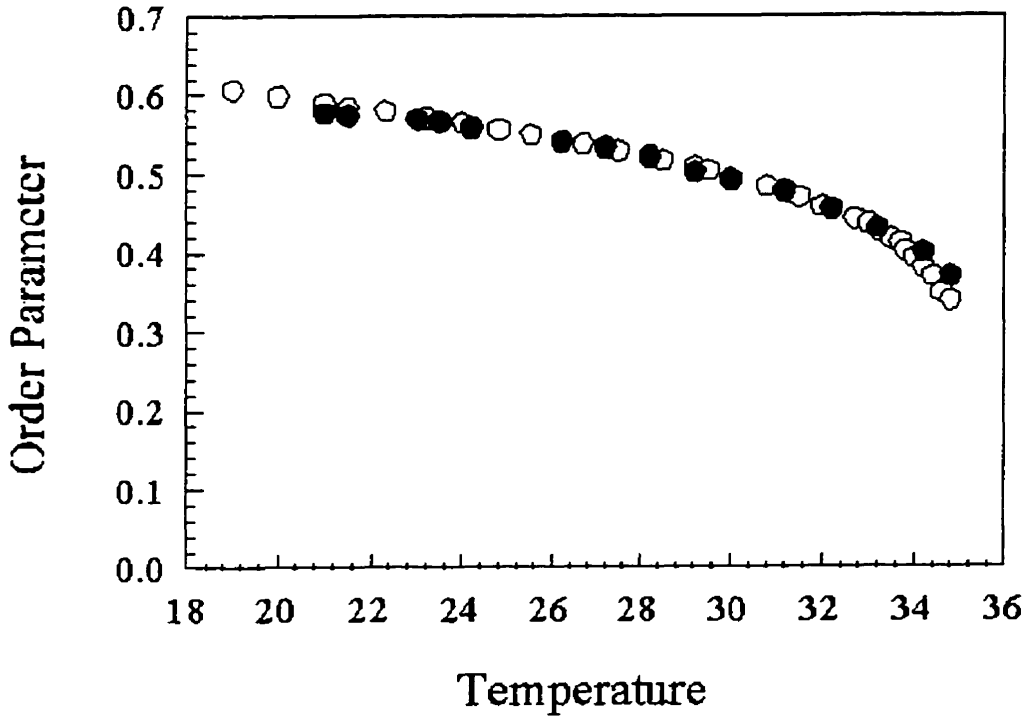

Figure 3.5: *Order parameter for 5CB as a function of temperature from values calculated at 589 nm (•) and 633 nm (○).*

These calculations for the order parameter as a function of temperature neglected the contributions of the density change of the liquid crystal. The density is related to the order parameter through the optical dielectric constant, ϵ, where $\epsilon = n^2$. However, the density change over the nematic range is usually no more than 5%[55] and the order parameter is much more sensitive to the temperature.

The order parameter is a measure of the orientational potential energy function. The stability of the liquid crystal molecule is determined by the interactions with the surrounding molecules. The force experienced by one molecule is on average the same for all molecules according to the mean field approximation[49]. The

mean field approximation of the orientational potential energy function is $V(\cos\theta) = -\upsilon P_2(\cos\theta)S$ where υ describes the overall strength of the intermolecular interaction. Using $S = \langle P_2(\cos\theta)\rangle$, the potential becomes $V(\cos\theta) = -\upsilon P_2(\cos\theta)\langle P_2(\cos\theta)\rangle$. The stability of the nematic liquid crystal phase arises from the interactions between the individual molecules[54]. The forces between the molecules depend not only on their separation, but also on their mutual orientation. These molecules act in a manner that favors the parallel alignment of neighboring molecules[54] because that corresponds to the lowest energy configuration.

Chapter 4

Experimental apparatus

4.1 Introduction

The experiments performed for this thesis used two different sets of experimental apparatus. The first set-up was built to measure fluorescence emitted from gas-phase clustered molecules. The second set-up was designed for measuring the changes in polarization of a liquid crystal film due to an impinging gas beam.

In the fluorescence experiments, gas is expanded through a pulsed nozzle to create a supersonic jet. The molecules in the expansion are excited by either 193 nm (ArF) or 248 nm (KrF) light from an excimer laser. The emission resulting from this excitation is dispersed with a monochromator and measured with a photomultiplier tube.

The effect of the gas beam on the liquid crystal film was measured by monitoring the polarization of a laser beam passing through the liquid crystal film. The gas beam was a skimmed supersonic jet expansion. The polarization is monitored by measuring the amount a light from an argon ion laser which is transmitted through a polarization measurement apparatus with a Si photodiode.

This chapter will begin with a discussion of supersonic free jet expansions since they are used in both experimental apparatus. After this the details of each of the two experiments will be discussed separately.

4.2 Supersonic free jet expansions

Under ordinary laboratory conditions the existence of van der Waals molecules is transitory and studies of their properties is difficult. Most recent work on clusters has been done by preparing a sample which is not at thermodynamic equilibrium using a supersonic free jet expansion[59].

There are a number of advantages in using a supersonic atomic or molecular beam, all of which result from the cooling produced by the jet expansion. A supersonic jet allows for the preparation of internally cold, isolated gas phase molecules. The cooling of the molecular beam produces molecules in the beam that are well defined in terms of translational and internal energy. The molecules have little internal energy which means that fewer internal states are populated. The spectra of molecules in molecular beams are simplified due to the few initial states populated. Downstream from the supersonic nozzle is a region in which the molecules are in a collision free environment. In this region the molecules can be studied without complication due to collisions with other gas molecules. It is possible to create van der Waals molecules in a supersonic jet expansion.

4.2.1 Free jet source

A gas beam is produced when gas from a high pressure region is allowed to enter a low pressure region through a small nozzle. When the mean free path of the gas is much smaller than the nozzle diameter then a supersonic jet expansion is produced as a result of collisions at the nozzle. In a supersonic jet expansion the random thermal energy of the gas behind the nozzle is converted into a directed motion. This is accomplished via the collisions at the nozzle and downstream from the nozzle.

A schematic of a free jet expansion is shown in Figure 4.1. The gas within the nozzle is at a pressure, P_0, temperature, T_0, and has a small random thermal energy, $\frac{3}{2}RT_0$. The gas flows toward the nozzle exit as a result of the pressure difference. The gas discharge through the nozzle and therefore the required pumping speed increases as P_0D^2,where D is the diameter of the nozzle[60]. A pulsed nozzle is used in the

experiments here to decrease the load on the pumps by over 90%. In the liquid crystal experiments a skimmer is used both to select out only the gas molecules which are traveling in the forward direction and also to reduce the load on the scattering chamber pump.

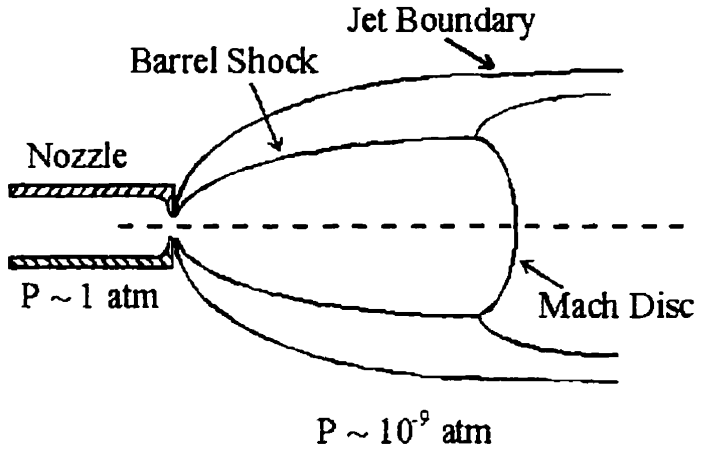

Figure 4.1: *Schematic of free jet expansion*

At the nozzle the velocity of the gas equals the local speed of sound (Mach number, M = 1). For

$$\frac{P_0}{P_b} > \left(\frac{\gamma+1}{2}\right)^{\frac{\gamma}{\gamma-1}} \tag{4.1}$$

where P_b is the background pressure within the chamber and γ is the ratio of the heat capacity at constant pressure over the heat capacity at constant volume, the exit pressure from the expansion is independent of the background pressure. The ratio on the right hand side of Equation 4.1 is less than 2.1 for all gases, therefore this condition is generally met. Downstream from the nozzle, the velocity (or Mach number) increases. Since the gas is traveling at velocities greater than the local speed of sound, it cannot have information about downstream boundary conditions. At this point the gas is in the "zone of silence". Eventually the gas jet "collides" with the background gas. At this point a shock boundary is formed, called the Mach disk, which changes the direction of the flow and reduces the Mach number. The Mach

disk location[60] is

$$x_M = 0.67 \left(\frac{P_0}{P_b}\right)^{\frac{1}{2}} D.$$

For the jet expansions described in this thesis, $x_M = 1 - 10$ m which is always longer than the distance to the vacuum pumps and the width of the barrel shock is on the order of $0.5\,x_M$[60]. If the gas beam collides with some physical object in the chamber at some smaller distance that object will define the Mach disk. In the fluorescence experiments described below the fiber optic, to be described later, defines the width of the barrel shock. For the fluorescence experiments, the gas is studied 0.35-0.65 cm downstream from the nozzle, which is within the zone of silence for the expansion. The gas-surface collisions take place 7-8 cm downstream from the skimmer in the liquid crystal experiments. If the gas beam is skimmed properly, the skimmer will not interfere with the molecules in the centerline of the expansion and these molecules will be within the zone of silence up until they reach the liquid surface. The gas beam sampling therefore is well within the zone of silence in both experiments.

It is possible to calculate the theoretical maximum velocity of the molecules in the gas jet as well as the temperature of the beam and the nozzle flow rate. By knowing the nozzle flow rate and the velocity of the beam the kinetic energy of the beam may be determined. The internal energy of the gas molecules in the beam is determined by the internal energy states occupied by molecules of the beam. A means of measuring the internal energy of the gas beam is described in Appendix A.

The gas flow is described[5][32] in terms of thermodynamics if we consider gas segments large enough for continuum thermodynamics to apply, yet small enough for the thermodynamic quantities to be constant within the segment. As long as there are no sources or sinks of entropy (viscous force, heat conductivity, shock waves, or chemical reactions) then the system remains isentropic. From Maxwell's relationships for isentropic systems[32],

$$\left(\frac{\partial T}{\partial V}\right)_S < 0$$

where T is the temperature and V is the volume, thus as the gas is expanded it also cools. As the gas is expanded, the flow velocity increases. The enthalpy of this

directed flow comes from the initial random thermal energy of the gas. From the principle of conservation of enthalpy the relationship between the enthalpy and flow velocity is given by[32]

$$\bar{H}_0 = \bar{H} + \frac{u^2}{2}$$

where $\bar{H}_0$ and $\bar{H}$ are respectively the molar enthalpies for the gas before and after the expansion, and u is the velocity of the gas leaving the expansion. This may be written in terms of the velocity as: $u^2 = 2(\bar{H}_0 - \bar{H})$. From introductory thermodynamics[3] the molar heat capacity ideal gas for an ideal gas at constant pressure may be defined as

$$\bar{C}_p = \frac{\gamma}{\gamma - 1}\frac{R}{W}$$

where R is the gas constant and W is the molar mass of the gas. Then for the jet expansion

$$u^2 = 2\left(\bar{H}_0 - \bar{H}\right) = 2\int_T^{T_0} \bar{C}_p\, dT = 2\int_T^{T_0} \frac{\gamma}{\gamma - 1}\frac{R}{W}\, dT$$

$$u^2 = 2\frac{\gamma}{\gamma - 1}\frac{R}{W}\left(T_0 - T\right). \tag{4.2}$$

In the limit that the temperature of the gas beam after the expansion is zero. The maximum for the velocity of the beam once it has entered the collision free zone is determined to be

$$u_{\max} = \sqrt{2\frac{\gamma}{\gamma - 1}\frac{R}{W}T_0}.$$

The temperature of the beam is a function of the Mach number of the beam, $M = u/a$, where a is the local speed of sound [32]. For an ideal gas the local speed of sound is related to the local temperature by

$$a = \sqrt{\gamma\frac{R}{W}T}. \tag{4.3}$$

The Mach number for distances greater than a few nozzle diameters downstream from the nozzle was shown[61] from hydrodynamics equations to be

$$M = A\left(\frac{X}{D}\right)^{\gamma - 1}$$

where $\frac{X}{D}$ is the distance downstream in units of nozzle diameters and A is a function of γ. This equation breaks down when the density becomes so low that there are no

binary collisions. When there are no binary collisions, the individual gas atoms can no longer exchange information and the temperature of the expanding gas cannot change. From Equations 4.2 and 4.3 an expression for the relative temperatures is found

$$\frac{T}{T_0} = \left(1 + \frac{\gamma - 1}{2} M^2\right)^{-1}$$

The temperature of gas in the expansion is related to the pressure of the gas in the expansion by the following formula[60].

$$\frac{P}{P_0} = \left(\frac{T}{T_0}\right)^{\gamma/(\gamma-1)} = \left(1 + \frac{\gamma - 1}{2} M^2\right)^{-\gamma/(\gamma-1)}$$

This allows one to determine the pressure of the expansion and in turn the collision frequency. For the I_2 cluster experiments, the interaction region is 17.5 nozzle diameters downstream. For an expansion of neat rare gas with an initial pressure of 760 Torr at 298 K, the Mach number is 22, the temperature is 1.8 K, and pressure is 2.2×10^{-3}Torr at the interaction region. The pressure dependence implies that the time between collisions will be on the order of $50\mu s$.

The nozzle flow rate is the rate at which molecules leave the nozzle, this is an upper limit on the flow rate of molecules in the beam at the interaction region. The nozzle flow rate of molecules leaving the nozzle is given by Miller[60] as

$$\begin{aligned} \dot{N} &= F(\gamma)\, n_0 \sqrt{\frac{2kT_0}{m}} \left(\frac{\pi D^2}{4}\right) \\ F(\gamma) &= \left(\frac{\gamma}{\gamma+1}\right)^{\frac{1}{2}} \left(\frac{2}{\gamma+1}\right)^{\frac{1}{\gamma-1}} \end{aligned}$$

where n_0 is the number density for the gas.

Past the nozzle, the pressure decreases such that after a distance of a few nozzle diameters there are no collisions. The binary collisions which scale as $P_0 D/T_0$, increase the flow velocity while decreasing the translational temperature. The translational temperature is defined as the width of the velocity distribution about the flow velocity. In a free jet there are typically 10^2 to 10^3 collisions[60]. Rotational to translational energy transfer is usually rapid and generally 10 - 100 collisions are sufficient for rotational relaxation of diatomics.[60]. Vibrational to translational energy

transfer is usually much slower, as a result on the order of 10^4 collisions are necessary for vibrational relaxation of diatomics.[60]. For the experiments discussed here the calculated vibrational temperature is on the order of 100K and the calculated rotational temperature is on the order of 10-15K, where the temperature is defined at the Boltzmann temperature which is associated with the vibrational (rotational) population of the molecules in the beam (see Appendix A).

4.2.2 Clusters

Clusters form from the condensation of the beam gas in the expansion. Cluster formation is favored by low nozzle temperature and high stagnation pressure. The high stagnation pressure provides more multi-body collisions which are neccesary for the formation of clusters. The lower the temperature of the nozzle the lower the energy of the gas, which makes condensation more probable. The temperature of noble gas clusters produced in a supersonic expansion is primarily a function of the molar energy of evaporation and not the expansion conditions. The temperature of argon clusters formed in an expansion similar to ours is 32 ± 2 K[16][17]. The production of clusters may be controlled by varying the physical expansion conditions, the complexing gas or the partial pressures of the gases in the expansion.

In order for two molecules to form a stable van der Waals molecule, there must be a third body in the collision to carry off the excess energy to stabilize the dimer. The kinetics for the production of I_2·RG is written as[32]

$$I_2 + RG + (\text{third body}) \longrightarrow I_2 \cdot RG + (\text{third body})$$

where RG is a rare gas atom. In the case of the clusters produced for this project the ratio of I_2/RG is always less than 0.2%, therefore the third body will almost certainly be another rare gas atom. Thus the rate of production of I_2·RG dimers is

$$\frac{d\,[I_2 \cdot RG]}{dt} = k\,[I_2]\,[RG]^2$$

where k is a constant which is determined by the specific molecules in producing the dimer. The specific heat ratio of molecules as well as the nature of the bonds which

they form affects the size and number of clusters formed. Gases with larger thermal accommodation coefficient (a large interaction energy) are more effective per collision at transferring energy to relax the excited state complex. As an example xenon is more effective than helium at forming larger van der Waals clusters. Xenon has a larger polarizability which effectively increases the interaction time of Xe with the $[I_2 \cdot RG]^{\ddagger}$ complex, which enhances the ability to transfer energy to relax the excited state complex.

4.3 Fluorescence experiments

4.3.1 Cluster experimental set-up

The cluster experiments are performed in a 12 inch long, 10 inch diameter cylindrical chamber, which is sketched in Figure 4.2[62][63]. This chamber is pumped by a 5000 L/s diffusion pump which is backed by a 50 cubic feet per minute mechanical pump. The pressure inside the chamber is measured with a cold cathode ion gauge. The base pressure is measured with the supersonic jet off and has a value of 5×10^{-7} Torr. With the supersonic jet operating at 20 Hz with a 0.2 or 0.5 mm nozzle and 2 atm backing pressure, the pressure in the chamber is between 10^{-5} and 10^{-4} Torr. A General Valves pulsed solenoid nozzle is suspended from the top of the chamber. Attached to the bottom of the pulsed nozzle is a black Delrin alignment bracket. The bracket is designed to align the fiber optic with the interaction region where the laser crosses the gas beam. The alignment bracket (see Figure 4.3) consists of two C-shaped pieces and two baffle arms. A UV-visible fiber optic bundle is mounted through a hole in one of the C-pieces such that its center is aligned with the center of the 2.5 mm inner diameter baffle arms and the fiber optic is held perpendicular to the axis defined by the baffle arms. The fiber optic end is 6 mm from the center of the bracket. The fiber optic has a 4.3 mm aperture, this allows for solid angle for light collection of 0.041 steradian. The alignment bracket is designed so that the

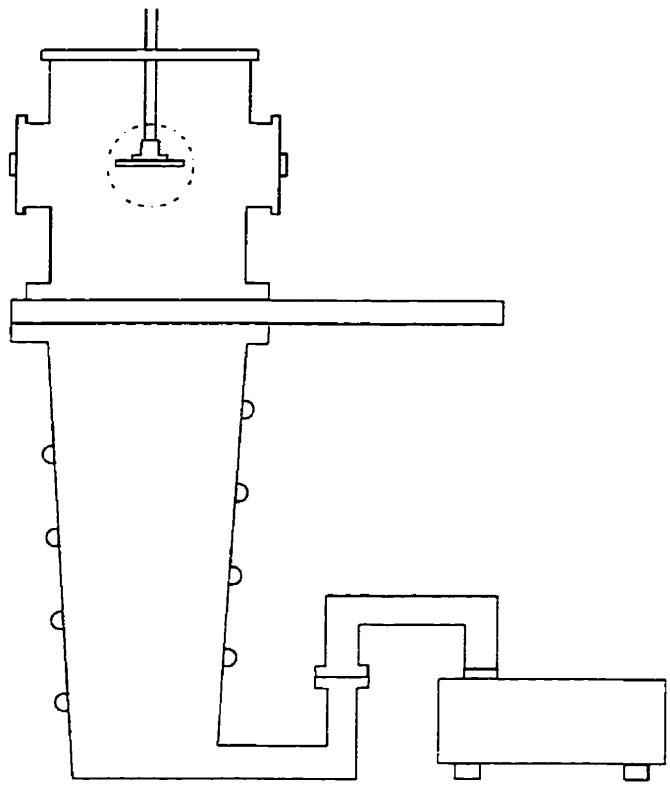

Figure 4.2: *The chamber in which the cluster experiments are performed.*

baffle arms are either centered 3 mm or 6.5 mm below the pulsed nozzle.

The optical arrangement of the experiment is shown in Figure 4.4. The output of an ArF (193 nm) or KrF (248 nm) excimer laser enters the chamber through a Suprasil window and is directed through the baffle arms. The excimer laser beam is focused with a 0.5 m focal length lens to a point approximately 10 cm beyond the intersection with the gas jet.

The result is a laser spot size of about 30 mm^2 at the interaction region between the laser and the gas beam. The 2.5 mm diameter baffle arms are smaller than the laser spot size, therefore about 50% of the laser light entering the chamber enters the interaction region with the gas beam. The laser energy going into the chamber is on the order of 3 mJ per 10 ns pulse. An upper limit to the duration of the excimer laser pulse was measured by observing the fluorescence off of a business card and is shown

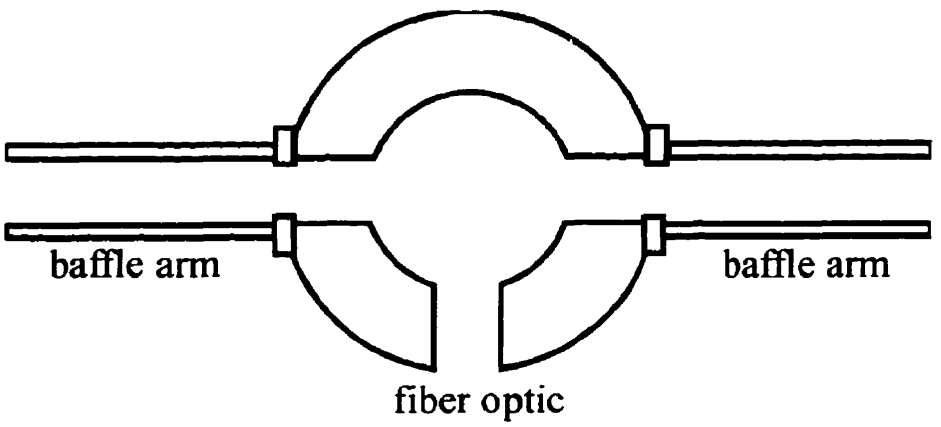

Figure 4.3: *Cross sectional view of the alignment bracket*

in Figure 4.5.

The fraction of emission resulting from the excitation of molecules in the gas jet which is collected by the fiber optic is transmitted through the fiber optic out of the vacuum chamber and onto the entrance slit of the monochromator. The light which passes through the monochromator is detected by a red sensitive photomultiplier tube (PMT) whose output is directed to both a boxcar integrator and a digital storage oscilloscope.

The timing, shown in Figure 4.6, for the laser, the pulsed nozzle, the oscilloscope, and the boxcar averager trigger are regulated with a Stanford Research Systems 510 digital delay generator. The time for the excimer is arbitrarily set at 5.0000 ms. The timing for the pulsed nozzle, the oscilloscope, and the boxcar averager are set based on this time. The boxcar and the oscilloscope are set at the same time delay. To find the appropriate time delay for the boxcar/oscilloscope, a business card is placed in the alignment bracket to reflect a small amount of laser light into the fiber optic and in turn the monochromator and thus to produce a signal at the PMT. The time delay for the boxcar/oscilloscope is varied until this signal (including the "front edge") is clearly displayed on the oscilloscope with the scope at its maximum time resolution. For these experiments the delay time was 5.0008 ms. In order to determine the delay time for the pulsed nozzle an expansion of I_2 in helium is excited with 193 nm light

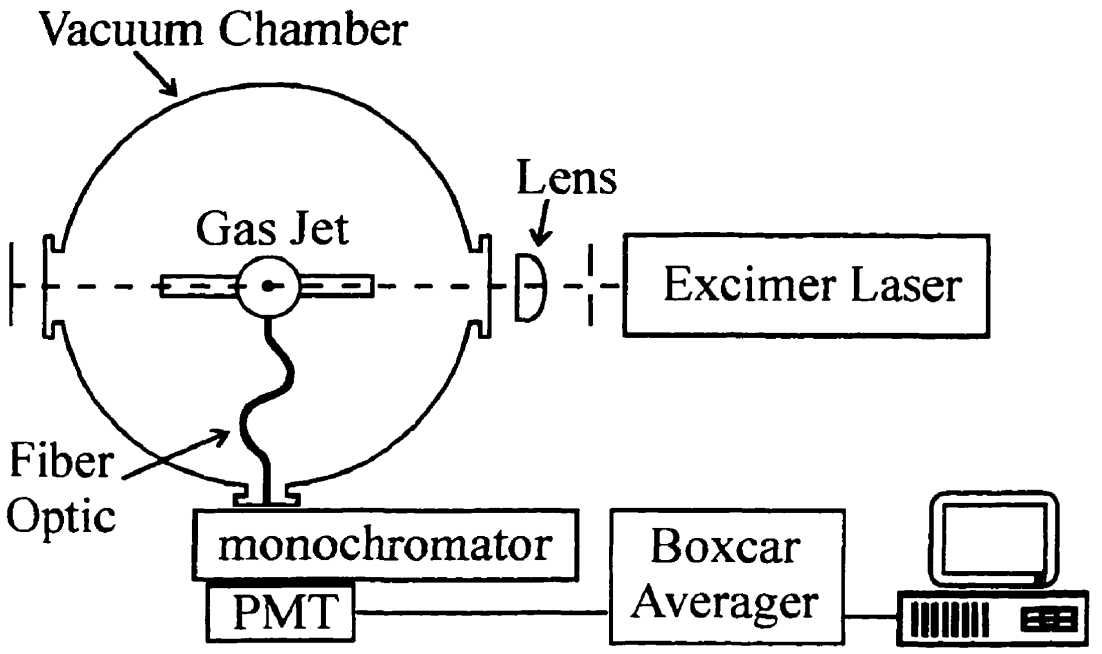

Figure 4.4: *Cluster experimental set-up*

and the monochromator is set to the D → A transition. The time for the pulsed nozzle is changed to find the minimum and maximum time for which a signal is measured. The delay time for the pulsed nozzle is set at the middle of the range for which signals were observed, which in these experiments was 4.0000 ms.

A spectrum is measured by stepping the monochromator in 1 or 2 nm increments and measuring the signal from the PMT. (The monochromator was generally used with entrance and exit slits which result in a 2 nm resolution.) The PMT signal was input to the boxcar averager. The delay time for the boxcar was set so that the maximum signal would be measured, this time was on the order of 100 ns. The boxcar gate width was generally set at 30ns and its sensitivity varied between 1 and 50 mV depending on the specific experiment. Each point on the spectra was averaged over 30 laser shots. The output from the boxcar was sent to a GPIB computer interface and in turn to the laboratory computer for processing. The computer program used to collect the data from the computer interface through the GPIB port was a modification of the program written by Dr. Elizabeth Bishenden. The modifications were made

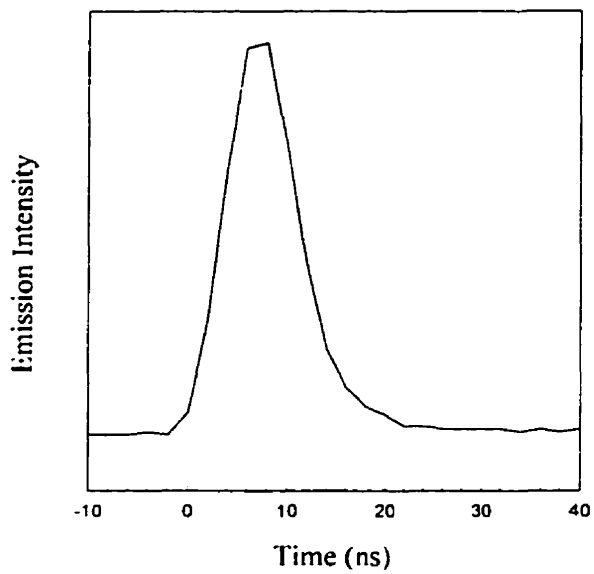

Figure 4.5: *The ArF excimer laser fluence as a funcion of time.*

to interface with the monochromator. No attempts were made to normalize the resulting signal based on the response of the fiber optic, the monochromator, or the photomultiplier tube.

4.3.2 Fluorescence lifetimes

In this set-up, the lifetimes of the emission bands are measured. The only difference between the experimental set-up for the these experiments from those previously described is in the electronics. The monochromator is set to the wavelength corresponding to the emission band. The signal at the PMT is measured for a single laser pulse as a function of time. This signal is collected with an Iwatsu Digital Storage Scope DS8631. The scope is used in single trace storage mode to preserve the emission signal. The signal collected by the oscilloscope is transferred to the laboratory computer via the GPIB board using a program written by Dr. Yibing Fan.

The manufacturer's specification of the oscilloscope rise time is 1.2 ns and the minimum time between data points is 2 ns. The laser pulse is of 8-10 ns duration.

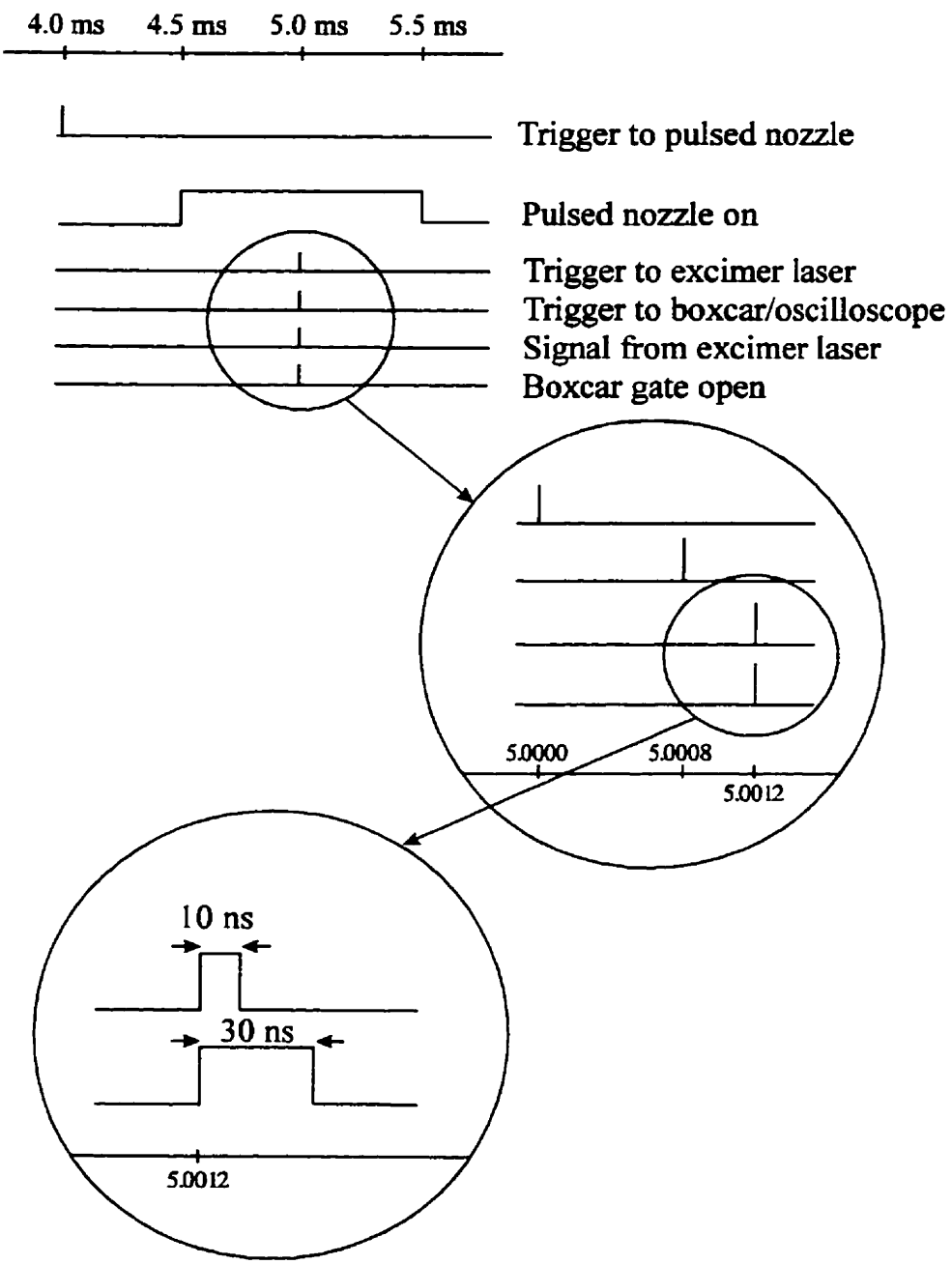

Figure 4.6: *Timing scheme for the cluster experiment.*

This is one limitation on the resolution of the measurements. The data for the laser light scattering consists of 5 or 6 data points and the rise time for the oscilloscope is one tenth of the laser fluence time. This makes fitting an appropriate function to the laser pulse nearly impossible. As a result the lowest lifetime which can be assigned is 20 ns and the best resolution possible for the emission lifetime is ±4 ns. The emission lifetime is measured to be the time between the onset of the emission and the time at which the signal decays to 1/e of the emission maximum.

4.3.3 Fluorescence collection

Fiber bundle

The fiber bundle used is an Oriel High Grade Fused Silica Fiber Optic Bundle. It has a 3.2 mm diameter and an acceptance cone of 25°. At 250 nm the fiber bundle transmits only 10% of the incident light. Between 350 and 1150 nm it transmits 55 to 60% of the incident light (see Figure 4.7).

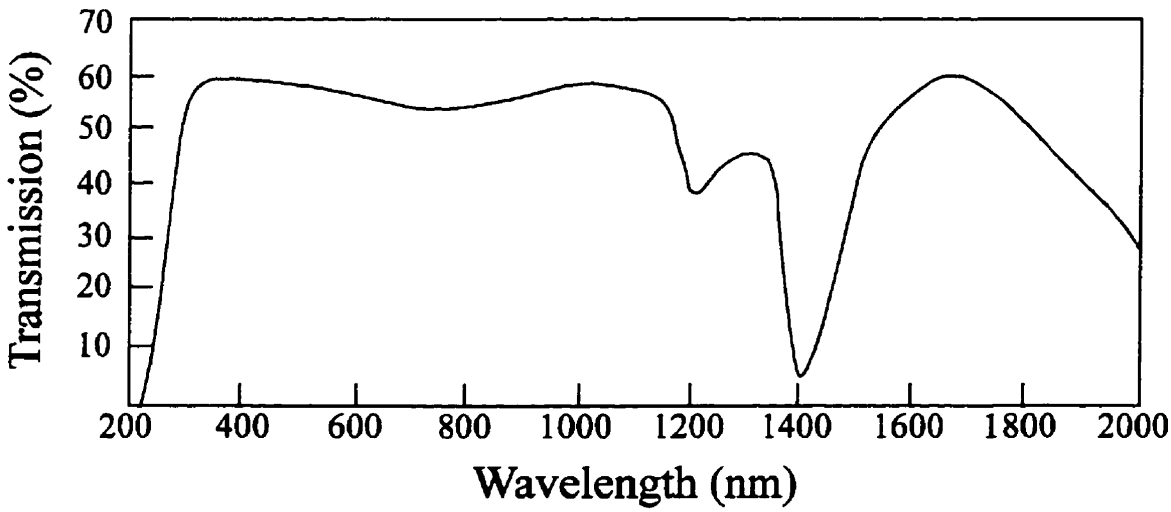

Figure 4.7: *Transmission coefficient for the Oriel High Grade Fused Silica Fiber Optic Bundle.*

Monochromator

The monochromator[64][65] used in these experiments is a CVI Digikron 120 Monochromator with a one-eighth meter pathlength. This monochromators is a Fastie Ebert design[65] and consists of a diffraction grating and several mirrors. The wavelength of light which is transmitted is determined from

$$n\lambda = 2d\cos\phi\sin\theta$$

where n is the order of diffraction, λ is the wavelength of the transmitted light, d is the grating groove width, ϕ is the Ebert Angle, and θ is the angle of grating rotation measured from the point at which light is specularly reflected through the monochromator. The Ebert angle is the half angle between the incident and diffracted beams. it is a fixed angle determined by the positions of the grating, the collimating laser and the imaging mirror.

The grating in the monochromator was blazed at 300 nm and optimized for wavelengths between 200 and 750 nm, with 2 or 8 nm resolution depending on which slits are used. The monochromator was wavelength calibrated using the 455, 477, 488, 497, and 515 nm lines from an argon ion laser.

A computer program (see Appendix C) was written in QuickBasic to interface the monochromator to the laboratory computer via the RS-232 port. The commands needed to be sent to the monochromator to perform various functions are described in the manual[65]

4.4 Liquid crystal polarization measurements

4.4.1 Liquid crystal experimental set-up

The experimental set-up consists of two vacuum chambers (see Figure 4.8). The first chamber is an 8 inch T-joint, which is the source chamber for the gas jet. This chamber is pumped with a Varian VHS-6 diffusion pump with a pumping speed of

2,400 L/s which is backed by a Welsh 1397 mechanical pump. The gas jet is produced with a General Valves solenoid nozzle with a 0.2 mm aperture. The nozzle is affixed to a translating mount which changes the distance between the gas jet and the skimmer. this distance is generally 2-3 mm. The nozzle is generally operated at 10 Hz with a 1 atm backing pressure of He, N_2, or Ar. The skimmer is the entrance to the scattering chamber; it has a 0.75 mm orifice.

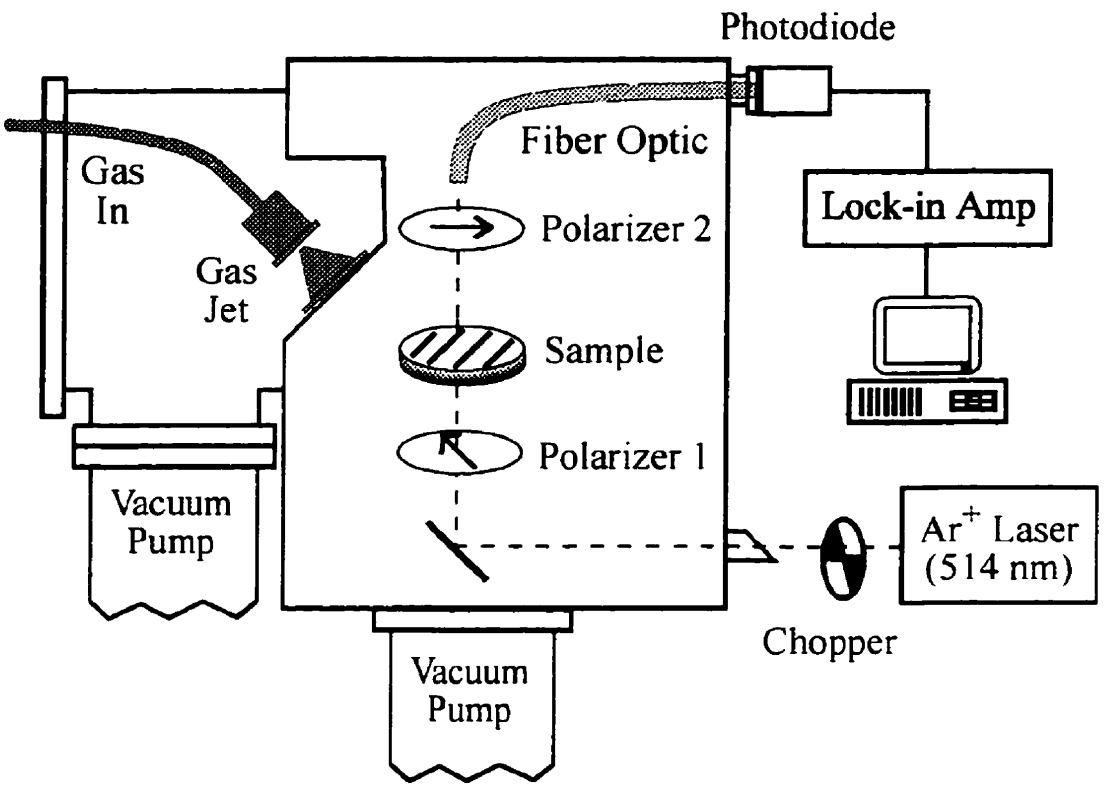

Figure 4.8: *Liquid crystal experimental setup.*

The scattering chamber is a 19" cube chamber in which the liquid crystal, the polarizers and the optics are mounted. There is a baffle between this chamber and the diffusion pump. The diffusion pump is identical to that on the source chamber. The backing pump is a Welsh 1402 mechanical pump. There is no valve between the chamber and the diffusion pump. The mechanical pump is warmed up with the valve between it and the diffusion pump closed. Then this valve is slowly opened to avoid

blowing the liquid crystal sample out of the sample holder. The background pressure in the scattering chamber is $\backsim 10^{-5}$Torr as measured by a cold cathode ion gauge.

The sample is placed on a rotating mount which is affixed to a temperature control mount, see Figure 4.9. The temperature control mount is a 3.5" long hollow copper cylinder with a 0.75" inner diameter and a 2.25" outer diameter, through which water flows. The angle between the gas jet and the sample surface normal is fixed at 45°. The temperature of the mount is determined by setting the temperature of the water bath. The rotating mount is controlled by a worm gear. This gear is affixed to a knob on the outside of the chamber, so that the sample may be rotated without opening up the chamber.

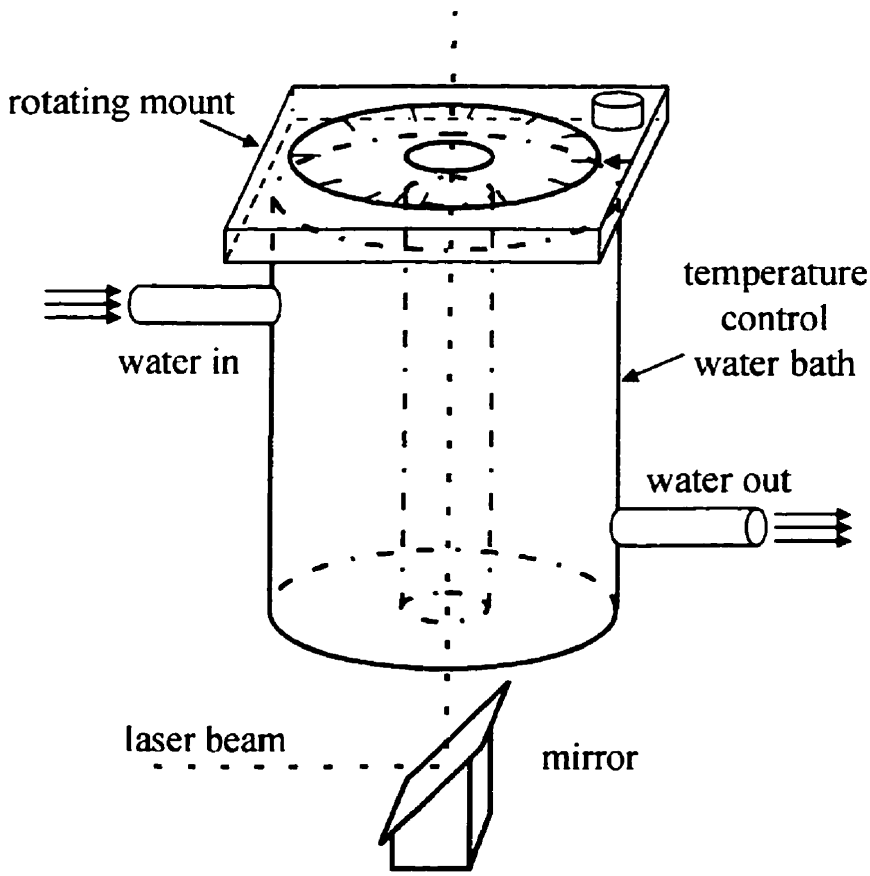

Figure 4.9: *Water control bath for the liquid crystal experiments shown with the mirror used for directing light through the sample.*

A 25 mW argon ion laser (Uniphase 2501) is used for the polarization measure-

ments. The light first passes through a monochromator to select out the 514 nm line and it is then chopped at 1.5 kHz. Next it is attenuated by a neutral density filter with an optical density of 2. The beam is reflected off a mirror into the chamber through a Brewster's angle window. Once inside the chamber the light is reflected off two steering mirrors to the polarization detection apparatus. The argon ion laser was chosen for its high stability in polarization and for its wavelength range. It is important that the light is not absorbed by the liquid crystal, 5CB only absorbs light between 190 and 315 nm[55].

The polarization detection apparatus consist of three optical elements. The laser light passes through the first element a linear polarizer and is reflected off of two mirrors. The polarization of the light leaving the second mirror is defined to be -45°. The light next passes through the liquid crystal sample. The liquid crystal sample is aligned at 0° by convention. The light transmitted throught the liquid crystal is then incident on the second polarizer, which is aligned perpendicular to the first polarizer, at +45°. The intensity of the light transmitted through polarization detection apparatus depends on a number of factors, which are described in Appendix B.

The light which is transmitted through the polarization detection apparatus is incident on a fiber optic bundle, from which it is carried outside the chamber. The light leaving the fiber optic bundle is measured with a Si photodiode.

The signal from the photodiode is used as the input to an SRS 510 lockin amplifier. The chopping signal from the laser is used as the reference signal. The signal on the lockin amplifier is monitored by a laboratory computer which communicates with the lockin amplifier via its RS-232 port. A computer program written in QuickBasic (see Appendix D) is used to collect a data point from the lockin amplifier every 5 seconds and displays the data in real time on the computer screen and saves the data to a a file.

4.4.2 Sample preparation

The liquid crystal samples are prepared on a glass plate (Hellma 210.003, os-0.1) which has a 0.1 mm high ring with a 1.5 cm inner diameter, based on the method of DeJeu[66]. This ring holds the sample in place and facilitates estimating the sample depth. The sample plate is washed with orvus soap and distilled water. A bottle brush is used to gently scrub away any residue from the previous sample. The plate is then rinsed thoroughly with distilled water to remove any traces of soap. The plate is either air dried or dried with a KimWipe, after which the plate is rinsed with spectroscopic grade acetone. In order to align the liquid crystal parallel to the surface of the plate, the surface of the plate is coated with poly-vinyl alcohol (PVA). The PVA coating is aligned in a specific direction and the liquid crystal aligns itself with the PVA.

A saturated solution of PVA in distilled water should be prepared two days in advance to ensure that the PVA has dissolved. Thirty microliters of this solution is dispensed onto the sample plate. The drop of PVA is spread to fill the sample plate by tipping the sample plate and/or by using the disposable plastic end of the microliter syringe. Care is taken to ensure that no long unsaturated PVA strands are on the sample plate. In order to allow for the water to evaporate from the PVA solution, the sample is either air dried overnight or set in a petri dish on a hot plate at a low setting for 5 minutes. The method of drying the sample makes no difference to the quality of the sample. When the PVA coating is dried, the normal direction is defined by rubbing the coating with a folded KimWipe in one direction about 100 times.

Approximately 20 μL of liquid crystal are dispensed onto the sample plate, which essentially fills the sample plate. The liquid crystal is very viscous and the aliquoted sample is checked for air bubbles before dropping on the sample plate. The sample is spread out to over the sample plate by the same method used for the PVA solution. For a volume of 20 μL the samples are on the order of 100 μm thick.

In order to verify that the sample is aligned, the sample is placed between the two

polarizers and the signal is measured at 0° (at a 45° angle to each of the polarizers) and at 45° (aligned with one of the polarizers). If for instance the liquid crystal is aligned with the first polarizer, then no light will be transmitted through the second polarizer. The maximum signal which will be transmitted through this set up is when the liquid crystal is oriented at an angle of 45° to each of the polarizers as in Figure 4.10, which is here defined as at an angle of 0°. The signal at 45° is generally twice

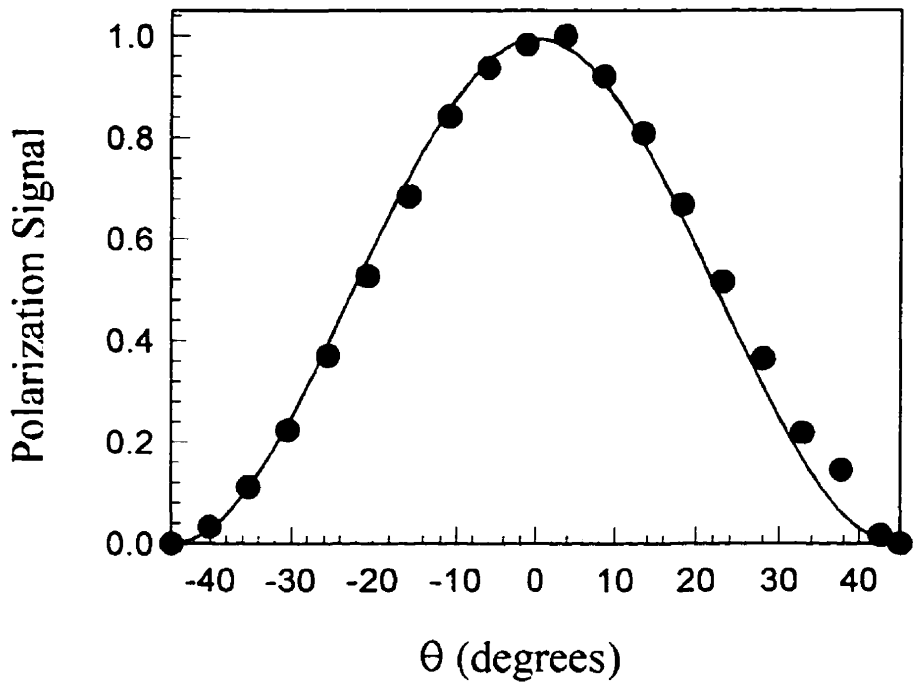

Figure 4.10: *Amount of light passing through the polarization detection apparatus as a function of the angle of the liquid crystal. The dots represent the data collected by Olivier Michel[109]. The line is drawn is the theoretical signal as a function of the angle.*

that of the signal with no sample and the signal at 0° is generally 5 or 10 times larger than the background signal with no sample.

The alignment of the liquid crystal results from making scratches in the PVA coating[66]. The first layer of liquid crystal molecules align with the scratches on the surface and subsequent layers align to lower layers of the liquid crystal. As a result of this method of alignment, the degree of alignment decreases as the thickness of the sample increases. If more than about 40 μL of sample is used (200 μm thickness) the

alignment is poor.

Chapter 5

Photophysics of I_2 in van der Waals clusters

5.1 Introduction

It has long been known that I_2 absorbs light in the region of 183 nm[67]. Absorption of light at 193 nm populates high vibrational levels (v $\backsim$150) of the D (0_u^+) state[8]. Fluorescence and collisional quenching of this state by rare gases has been studied by various groups[68][69][42]. The D′ state is the lowest energy state of the first tier ion-pair states which have a dissociation limit at I^+ ($^3P_2$)+I^- ($^1S_0$). Collisions of I_2 (D) with buffer gases results in a complex collisional cascade to the D′ (2_g) state. which rapidly emits to the A′ (2_u) state[70][71]. For high pressure buffer gas (e.g. 100 Torr of argon). interstate relaxation is fast enough to almost completely quench the D→X emission in favor of D′ →A′ emission[72].

Macler and Heaven[9] studied the spectroscopy and relaxation dynamics of I_2 isolated in rare gas matrices. Upon excitation of I_2 at 193 nm they observed an intense vibrationless emission feature centered at 380 nm in argon and 423 nm in krypton matrices. These results were interpreted as being due to the D′ → A′ transition.

by analogy to the gas phase work of Tellinghuisen and Phillips[72]. However, upon further analysis, the spectrum was determined to originate from an admixture of the lowest tier ion-pair states[73] rather than from a single ion pair state. The close nesting of the I_2 ion-pair states along with the relaxation dynamics would allow interactions with argon to readily admix these states. This analysis is substantiated by emission from the ion-pair states populating both the A and A′ states in solid argon[9]. Population of the A state would be unlikely if the emission had originated either from the original unperturbed D state, as a result of the $\Delta\Omega = 0$ propensity rule and the $g \Leftrightarrow u$ selection rule[74], or the D′ state, as a result of the $\Delta\Omega = 0$ propensity rule.

Fei, Zheng, Heaven, and Tellinghuisen[73] studied clusters of I_2 in argon. These clusters were excited at 193 nm and a broad emission feature was observed at 400 nm which was analogous to that observed in the matrix work, and was assigned to an ion-pair to valence transition of $I_2 \cdot Ar_n$. This assignment was made because the feature does not correspond to any known system of free I_2 and it was only observed in expansions with argon.

In the present work, I_2 is expanded with a number of rare gases and excited to the lowest tier ion-pair states by a 193 nm excimer laser. This excitation promotes I_2 to the ion pair states and resolved emission reveals information about the spectroscopy and dynamics of I_2 clusters. The work presented here has been published as "Photophysics and photochemistry of I_2(D,D′) in rare gas clusters" in Chemical Physics **211**, p377-386 (1996).

5.2 Spectroscopy of I_2

The spectroscopy of I_2 has been studied for many years in the gas state and the potentials of many of its electronic states are well characterized[67][7], see Figure 5.1. The dissociation of the ground state iodine, I_2 X $0_g^+(^1\Sigma)$, leads to the formation of two ground state iodine atoms, I ($^2P_{3/2}$). There are a number of other states of the iodine

molecule which all correspond to the iodine atom ground state dissociation limit, such as the A $1_u(^3\Pi)$, A' $2_u(^3\Pi)$, and $^1\Pi$ (1_u) states. There is also a set of electronic states (including the B $0_u^+(^3\Pi)$ state) which on dissociation produce I $(^2P_{3/2})$ + I $(^2P_{1/2})$. The B state of I_2 has been studied in detail because it may be accessed directly from the ground state by absorption of light on the order of 500 nm.

The lowest tier ion-pair states of iodine are most important for the work presented in this thesis. All molecules possess ion-pair states in which bond breaking leads to the production of a pair of oppositely charged ions[75]. In iodine the lowest tier ion pair states correspond to $I^+(^3P_2)+ I^-(^1S_0)$ and consists of the D' $2_g(1)$, β $1_g(1)$, D $0_u^+(1)$, E $0_g^+(1)$, γ $1_u(1)$, and δ $2_u(1)$ states[75] in order of increasing minimum energy. Excitation of ground state iodine to high vibrational levels of the D state is accomplished by absorption of 175-210 nm[76] radiation. The F $0_u^+(2)$ state (which is not shown in Figure 5.1) belongs to the second tier of ion-pair state and on bond breaking forms $I^+(^3P_0) + I^-(^1S_0)$. Although this is far from a complete picture of I_2 spectroscopy the states which are of interest in this thesis have been presented.

In halogen spectra single photon excitations show an overriding preference for $\Delta\Omega = 0$ transitions[77], where Ω is the total angular momentum of the electrons about the internuclear axis. Single photon absorptions in iodine also follow the general selection rule $g \longleftrightarrow u$, where g refers to an even electronic state and u refers to an odd electronic state.

5.3 Results

Gas mixtures of I_2 ($\approx$ 0.3 Torr) with 0.2 - 2 atm of carrier gas were expanded into a vacuum chamber through a commercial solenoid pulsed nozzle having a 0.2 or 0.5 mm orifice. Unless otherwise stated all of the expansions used a 0.2 mm orifice nozzle. The gas mixtures were obtained by flowing helium (Matheson, 99.995% purity), neon (Spectra Gases 99.999% purity), argon (Matheson, 99.9995% purity), krypton (Spectra Gases, 99.997% purity), or xenon (Spectra Gases, 99.995% purity) over a

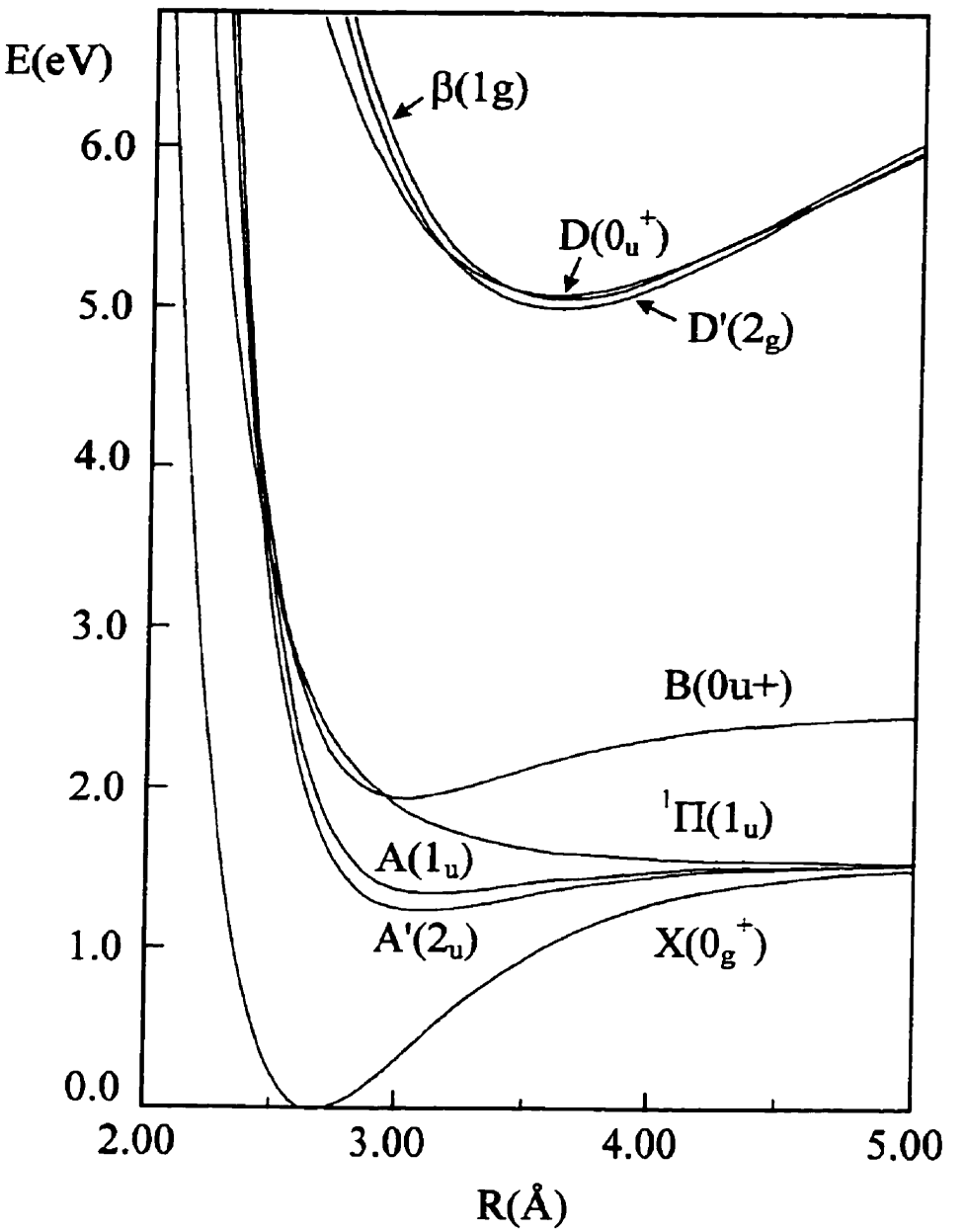

Figure 5.1: *Potential energy curves for I_2.*

room temperature solid sample of I_2 (BDH, ACS grade, unpurified), with a vapor pressure of 0.3 Torr. Under the expansion conditions used in these experiments, at most one I_2 molecule would be expected to be within a single cluster[28]. Some of the experiments involved using a gas mixing system Edwards Datametric Flow Controller 1605 to control the ratio of two carrier gases.

The free I_2 molecules in the jet had a rotational temperature of 10 to 15 K (see Appendix A). This temperature was determined by measuring an excitation spectrum of the free I_2 in the jet on the B←X transition and comparing the observed spectrum to simulated spectra as described in previous work from this laboratory[78]. Measuring the temperature of I_2 which was in clusters was not possible as a result of the efficient quenching of B state fluorescence by rare gas atoms[59].

Fluorescence from iodine molecules excited by the ArF excimer laser (193 nm) was transmitted *via* a fiber optic bundle to the entrance of the monochromator. Light transmitted through the monochromator passes through a cutoff filter to ensure that light at twice the laser wavelength is not being transmitted. All of the emission observed was prompt, beginning before the end of the laser pulse. The collisions between the species in the beam would be at a rate of 50μs based on calculations using the ideal thermodynamic analysis of the expansion as discussed in Chapter 4. The longest temporal profile measured in any of the experiments was 80 ns, therefore intercluster collisions had no impact on any of the observed spectra. The term temporal profile is used, since the signal measured is a convolution of the actual fluorescence decay lifetime with the laser profile. The laser pulse duration is approximately 10 ns (see Figure 4.5).

5.3.1 I_2 with helium and neon

Under the expansion conditions of these experiments I_2 is not expected to cluster with either helium or neon, as a result of their low polarizabilities. That there is no clustering is corroborated by the observation of emission from the initially excited D state alone (see Figure 5.2). (Helium is much less efficient than the heavier rare

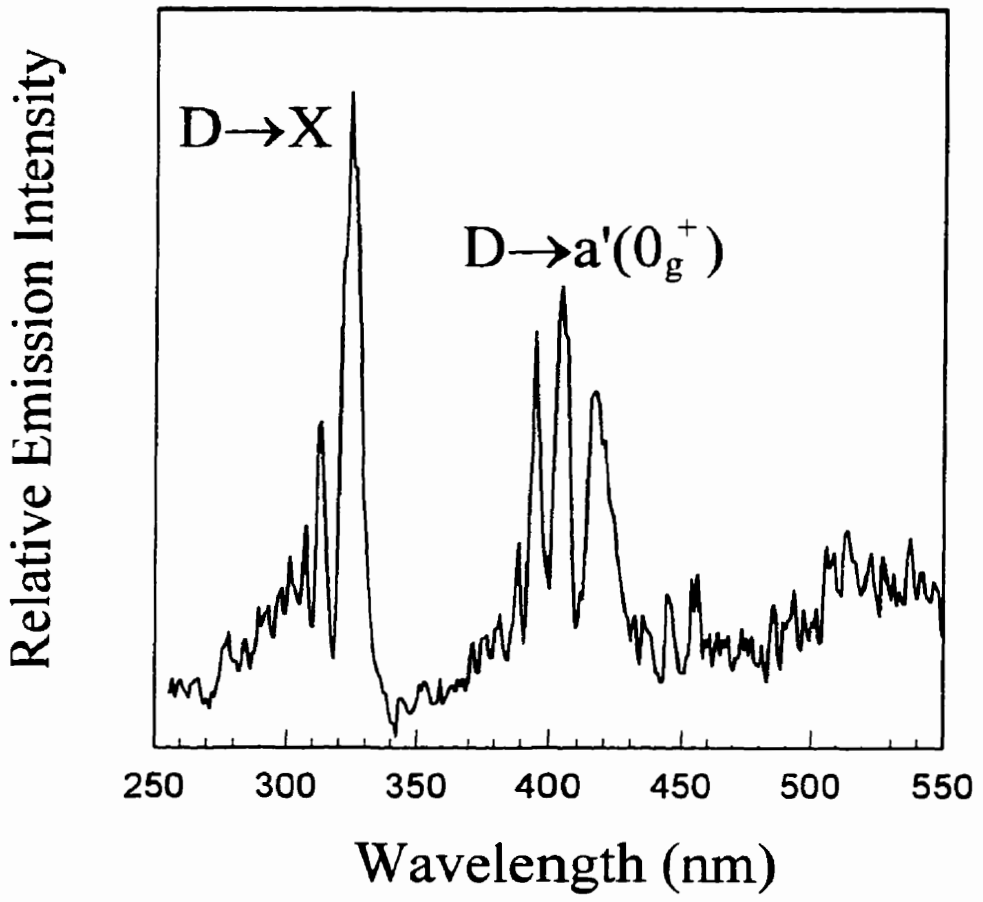

Figure 5.2: *Resolved fluorescence spectrum recorded following 193 nm excitation of expansions of 0.5 Torr I_2 in 1 atm He. The peaks are all due to emission from the initially excited D state of I_2.*

gases in inducing the D $\rightarrow$ D′ conversion and relaxation[72].) The emission observed is attributed[7][72] to the D $\rightarrow$ X (325 nm) and D $\rightarrow$ a′ 0_g^+ (410 nm) transitions in iodine. In addition, the spectrum displays no dependence on the stagnation pressure of the rare gas. Because the temporal profile of the emission tracks the laser profile closely, we can only measure an upper limit to the excited state lifetime of 17 $\pm$ 4 ns, see Figure 5.3. These experiments were also performed using nitrogen as the carrier gas (see Figure 5.4). For nitrogen stagnation pressures below 1 atm, the results were identical to those observed using either helium or neon. In expansions of I_2 with 2 atm of nitrogen emission is observed at 341 nm, which is attributed to the D′ $\rightarrow$A′ transition in iodine[70].

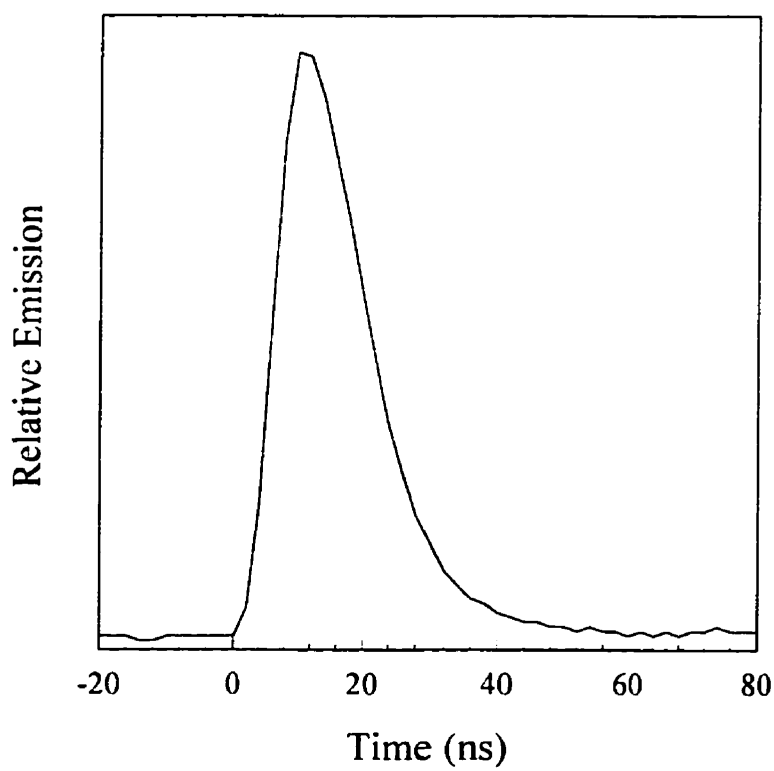

Figure 5.3: *Fluorescence decay trace for the D$\rightarrow$X transition in I_2.*

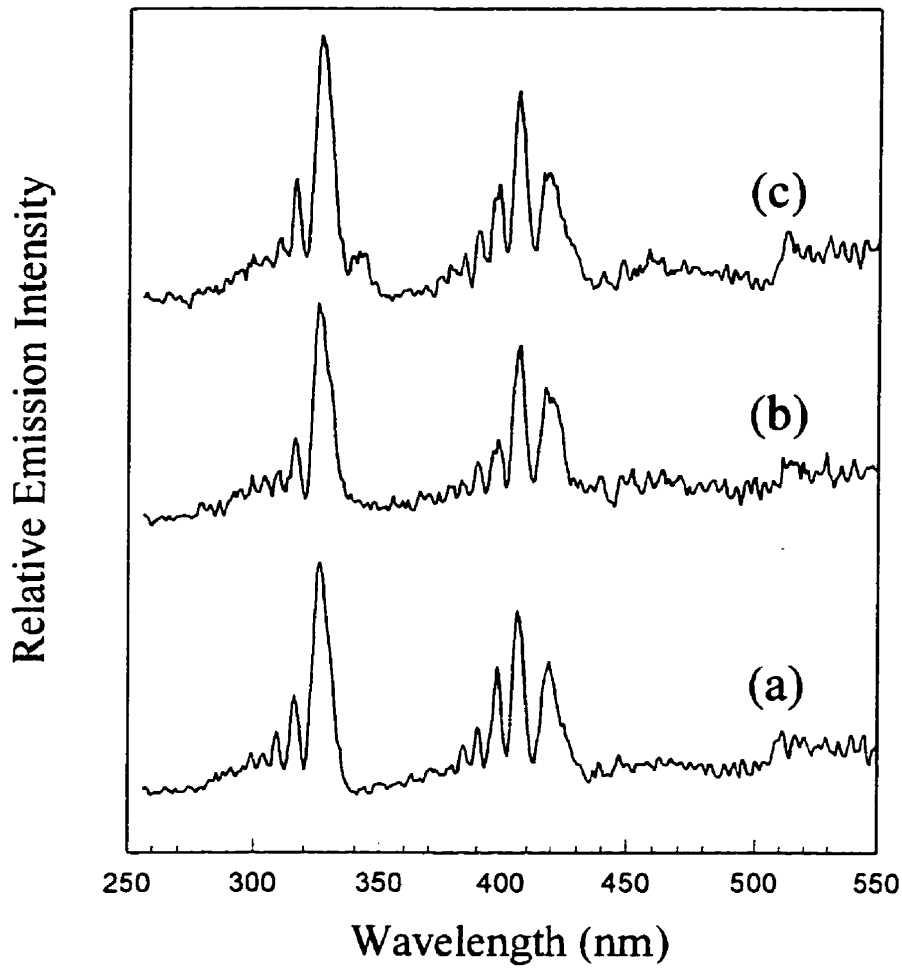

Figure 5.4: *Resolved fluorescence spectrum recorded following 193 nm excitation of expansions of I_2 in (a) 0.5 atm; (b) 1 atm; (c) 2 atm nitrogen.*

5.3.2 I_2 with argon

I_2 is expanded with an argon stagnation pressure of 0.5 - 2 atm. Figure 5.5a shows that at 0.5 atm stagnation pressure, the spectrum is like that measured using helium (see Figure 5.2) with the exception of a small peak at 341 nm. At 1 atm Ar stagnation pressure, the peak at 341 nm arising from D' $\rightarrow$A' emission in I_2[70] increases significantly in intensity (as displayed in Figure 5.5b). This feature is quite pronounced at 1 atm Ar stagnation pressure and accompanied by a decrease in emission intensity from the D state. The emission is a consequence of either D$\rightarrow$D' relaxation due to intracluster collisions[73] or to cluster perturbation breaking down the isolated I_2 selection rules. The D' emission is observed promptly, well within the intercluster collision time. The observed lifetime (see Figure 5.6) of less than 20 ns is the same as the time measured by Tellinghuisen and Phillips[72] for internal conversion D(v $\approx$150)$\rightarrow$ D'(2_g, v $\leq$ 5) caused by collisions with a buffer gas followed by spontaneous emission D' $\rightarrow$A'(v $\approx$12). The D' state itself has been determined to have a lifetime of 6.7 ns[79] Excitation of the ground state I_2 molecule directly to the D' state is in violation of the $g \Leftrightarrow u$ selection rule and is not possible in isolated I_2. Either of the above explanations indicate that clusters containing iodine are responsible for the observed emission.

For argon backing pressures greater than 1.5 atm, a new emission feature is observed, as displayed in Figure 5.5c. This band has previously been attributed to emission from $I_2 \cdot Ar_n$ clusters[73]. This band is quite broad in wavelength and demonstrates an increasing red shift with increasing argon pressure, up to the highest pressures used in this experiment (2 atm) and is accompanied by extinction of emission from the D electronic state. At 2 atm stagnation pressure the $I_2 \cdot Ar_n \rightarrow$ A'.A emission maximum is at 380 nm with a FWHM of 2600 cm^{-1}. This red shift corresponds to a red shift of 3000 cm^{-1} from the maximum of the D' $\rightarrow$A' emission in gas phase I_2. As shown in Figure 5.6, the temporal profile for this emission shows a decay time of 36 $\pm$ 4 nsec, in contrast to the report of Fei, et. al.[73], which gave an upper limit on the lifetime of 10 nsec. We observed this peak undergo a further red shifting to 400

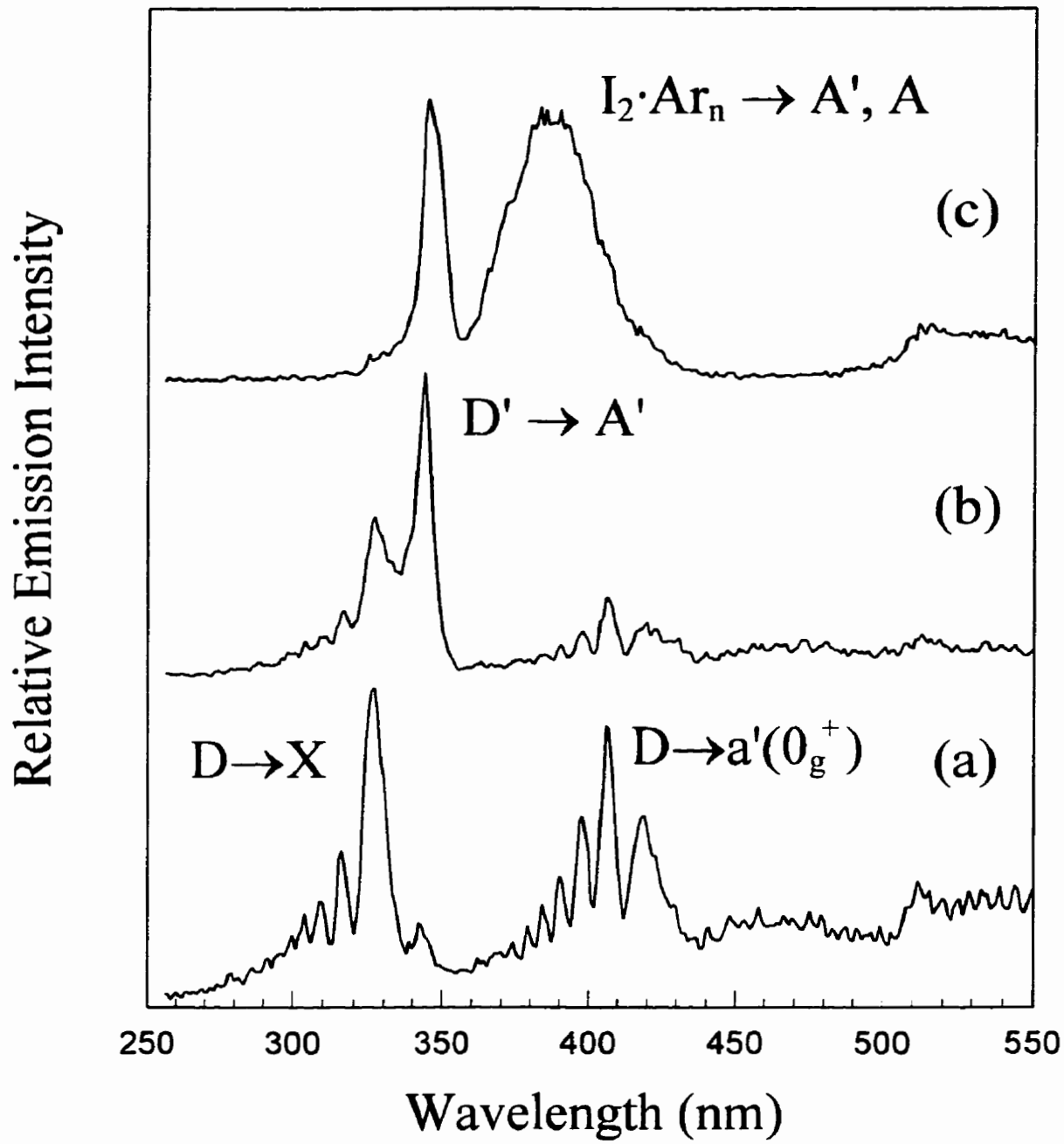

Figure 5.5: *Resolved fluorescence spectrum recorded following 193 nm excitation of expansions of 0.3 Torr I_2 in (a) 0.5 atm; (b) 1 atm; (c)2 atm of Ar. Note the quenching of the D state emission and the growth of the $D' \rightarrow A'$ band at 342 nm as the argon stagnation pressure is increased.*

nm with a FWHM of 1400 cm^{-1} when I_2 and 2 atm of argon were expanded through a 0.5 mm nozzle. (see Figure 5.7). Under these conditions the D and D′ emission was significantly diminished compared to the spectra recorded for 0.2 mm nozzle with all other conditions the same.

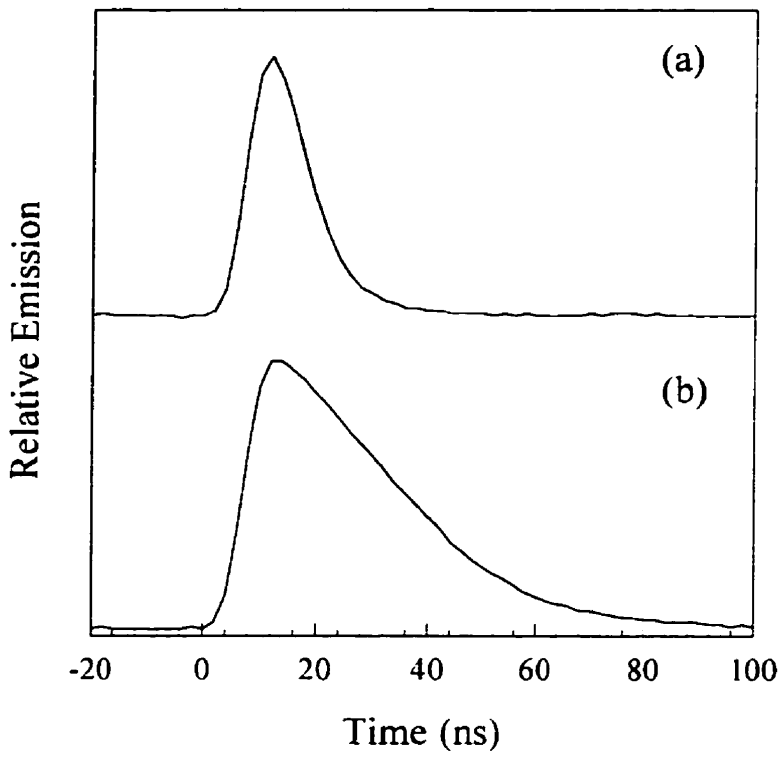

Figure 5.6: *Fluorescence decay traces of the emission features of I_2 expanded in argon. (a) The 341 nm emission in 1 atm Ar; and (b) the 380 nm emission in 2 atm Ar. The longer wavelength "cluster band" shows a decay time ~36 ns, compared to the D′ decay time of < 20 ns.*

5.3.3 I_2 with krypton

The spectra for I_2 expanded with krypton were measured with krypton stagnation pressures of 0.5 - 2 atm and are shown in Figure 5.8. Evidence of clustering is detected in the lowest pressure expansions used, where the D′ $\rightarrow$A′ emission is the dominant feature. This is consistent with work which shows that krypton expansions form

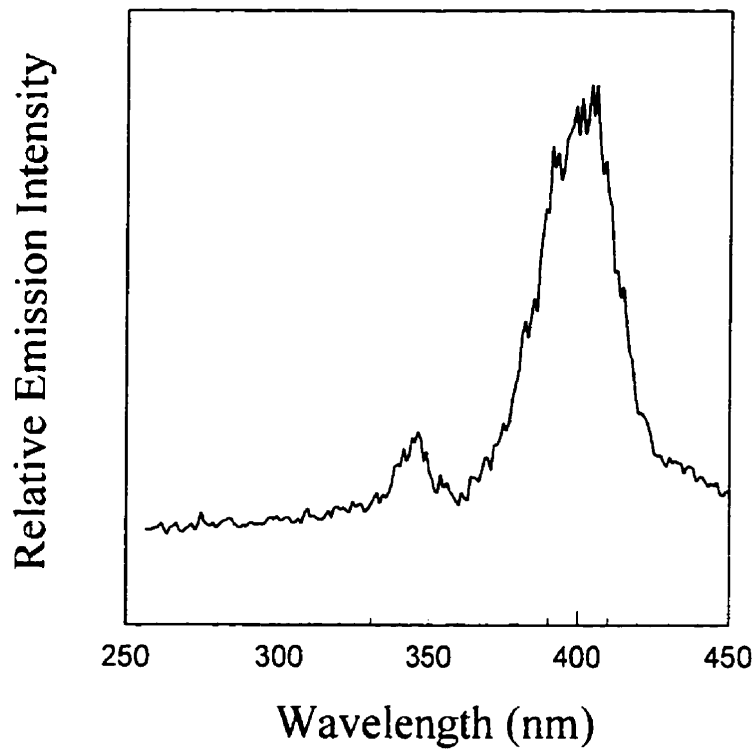

Figure 5.7: *Resolved fluorescence spectrum recorded following 193 nm excitation of 0.3 Torr I_2 expanded in 2 atm argon with a 0.5 mm orifice nozzle.*

larger clusters at lower pressures than argon expansions[60]. A broad-band emission similar to that observed in argon expansions is observed in all but the 0.5 atm kypton stagnation pressure expansions. The position of the intensity maximum of this peak shifts with increasing backing pressure from 341 nm to 437 nm at 1.7 atm krypton backing pressure. Increasing the krypton stagnation pressure further does not increase the red shift. The existence of a maximum red shift is consistent with the observations of Fei et. al.[73] where a maximum red-shifting of the $I_2 \cdot Ar_n \rightarrow A',A$ was observed at an argon source pressure of 2.5 atm. At 1 atm krypton stagnation pressure the decay time for this peak is approximately 50 nsec. the decay time increases to 80 ns for 2 atm krypton (see Figure 5.9). The growth of this emission feature is accompanied by the disappearance of emission from both the D and D' states. as was previously observed in argon expansions. An interesting feature of this emission band is that the width of the emission decreases from a FWHM of 2700 cm^{-1} at 1 atm Kr pressure to 1800 cm^{-1} at 2 atm Kr pressure (see Figure 5.8). The I_2 spectrum measured with the highest krypton expansion pressure is similar to that measured for I_2 frozen in a krypton matrix[9]. which consists exclusively of a broad emission feature at 423 nm.

5.3.4 I_2 with xenon

The emission spectra observed for iodine expanded with xenon are significantly different than those observed with other carrier gases. as is shown in Figure 5.10. Spectra were collected for I_2 expanded with 0.2 - 2 atm of xenon through a 0.2 mm nozzle. The spectra measured for I_2 expanded with 0.2 atm of xenon displays emission from both the D and D' states (see Figure 5.10a). An important difference between these spectra and those observed for the other rare gases is that the maximum fluorescence signal is observed for 0.3 atm xenon stagnation pressure (Figure 5.10b). At this pressure the emission is primarily from the D' state and the observed lifetime is identical to our measurements with other rare gases. In addition to a decrease in the D state emission. bands at 431 nm and 475 nm are observed[69][68]. The emission at 431 nm corresponds to E$\rightarrow$B emission in I_2[69]; its lifetime was measured as 24 ns within the

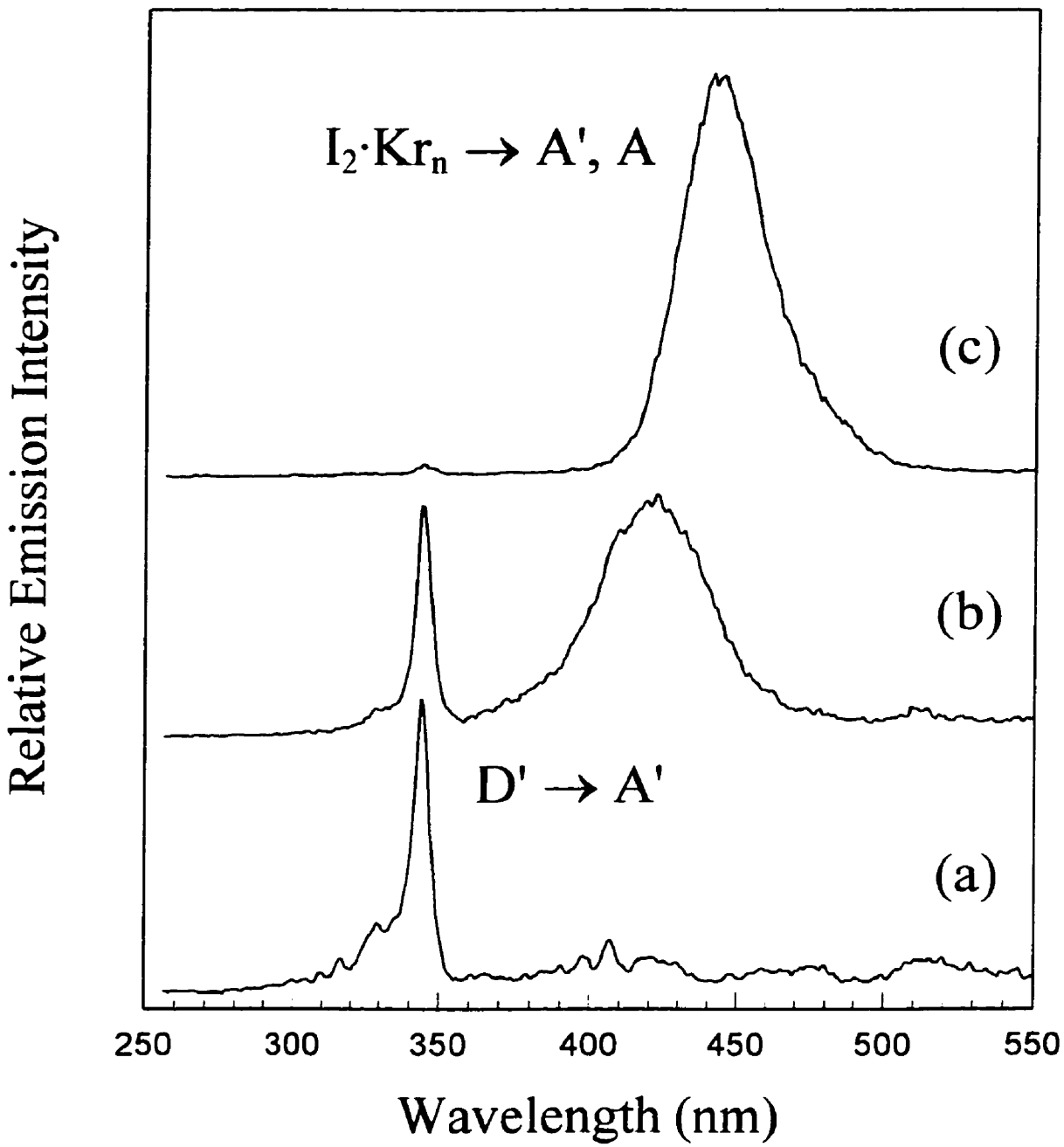

Figure 5.8: *Resolved fluorescencespectrum recorded following 193 nm excitation of expansions of 0.5 Torr I_2 in (a) 0.5 atm; (b) 1 atm; (c)2 atm of Kr. Note the quenching of the D state emission and the growth of the D' →A' band at 342 nm as the krypton stagnation pressure is increased.*

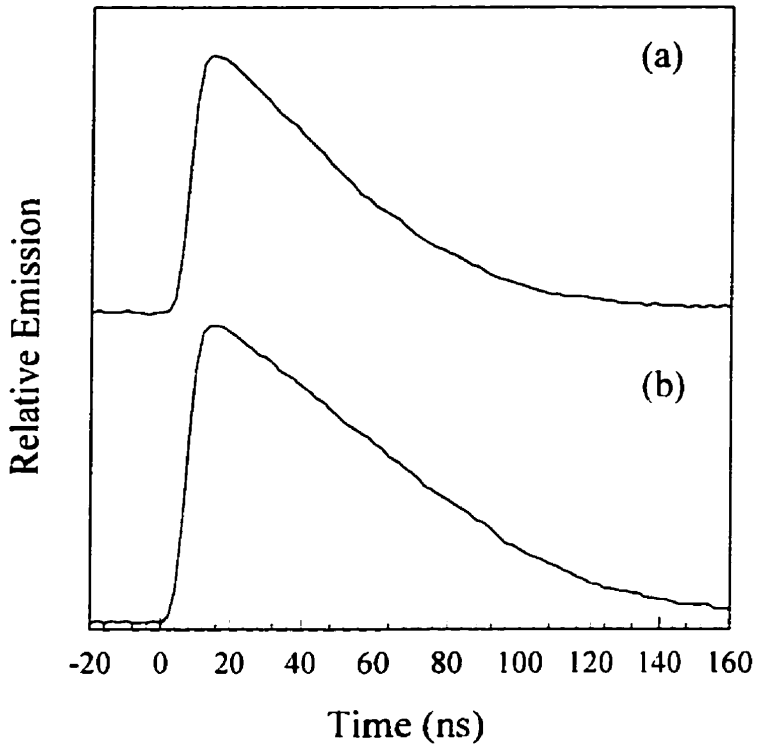

Figure 5.9: *Fluorescence decay traces of the (a) cluster emission from I_2 expanded in 1 atm Kr and (b) the cluster band at 2 atm stagnation pressure. Note the decay time increases from 50 to 80 ns with increasing the stagnation pressure from 1 to 2 atm.*

resolution of these experiments. Emission at 475 nm has been previously observed in I_2, but its origin has not been identified[68]. No emission from I_2 expanded in xenon pressure greater than 0.7 atm is observed. No emission is observed when xenon is expanded without I_2.

Another interesting feature of the emission from I_2 expanded with xenon is XeI (B→X) emission[42] (253 nm) with a decay time of $\leq$ 20 ns, as shown in Figure 5.11. This emission is very sensitive to the expansion conditions used. The conditions giving the largest signal intensity of XeI^* emission is expansions of I_2 with neat xenon is with a 0.5 mm orifice nozzle and a xenon stagnation pressure of 0.4 atm. This emission is not observed for lower pressures of xenon and it is quenched as the xenon pressure is increased (as is all of the other emission). I_2 expanded with a mixture of xenon and argon formed in a flow controller produced larger XeI^* signals than expansions with

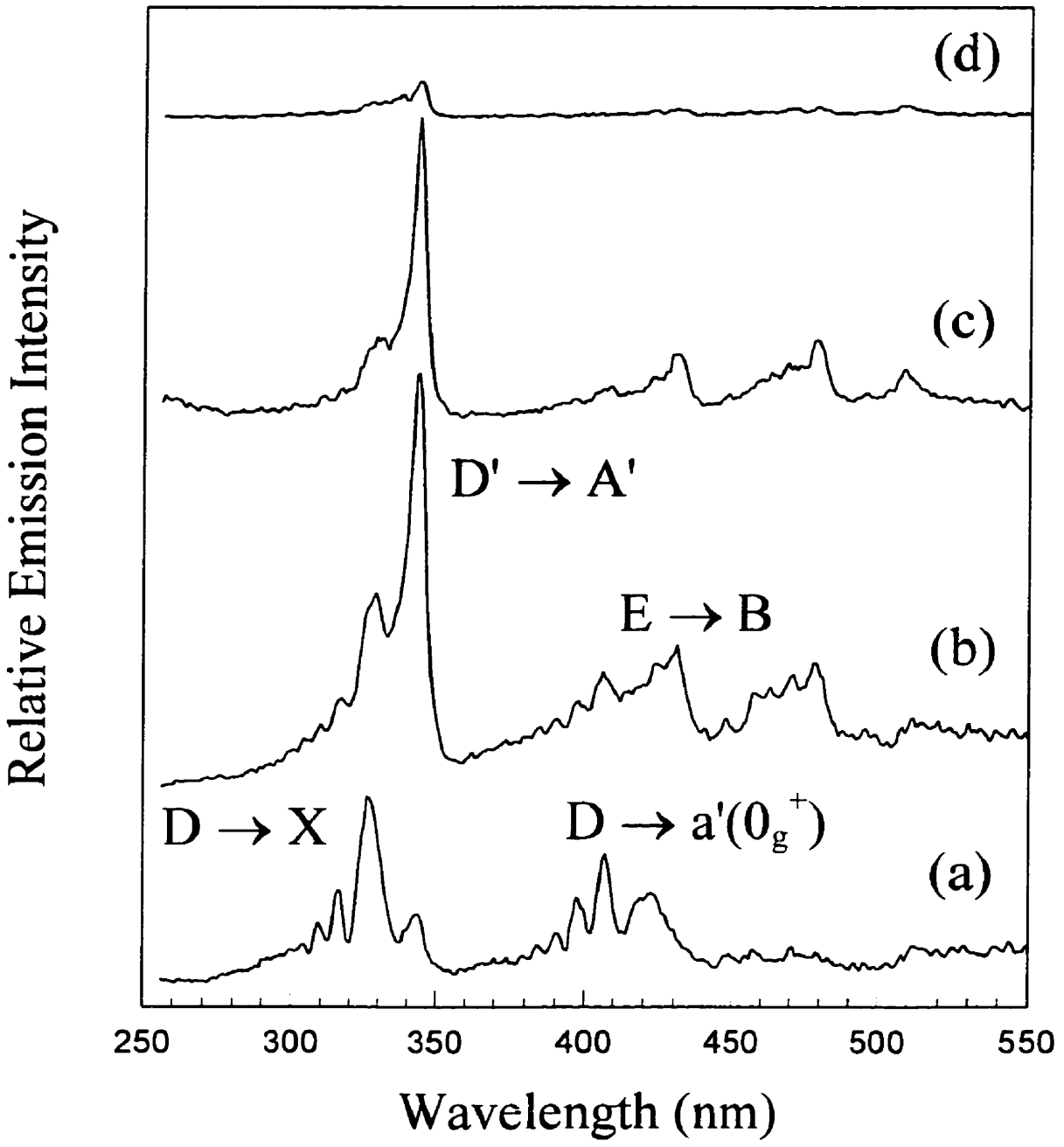

Figure 5.10: *Resolved fluorescencespectrum recorded following 193 nm excitation of expansions of 0.5 Torr I_2 in (a) 0.2 atm; (b) 0.3 atm; (c) 0.5 atm; (d) 0.7 atm of Xe.*

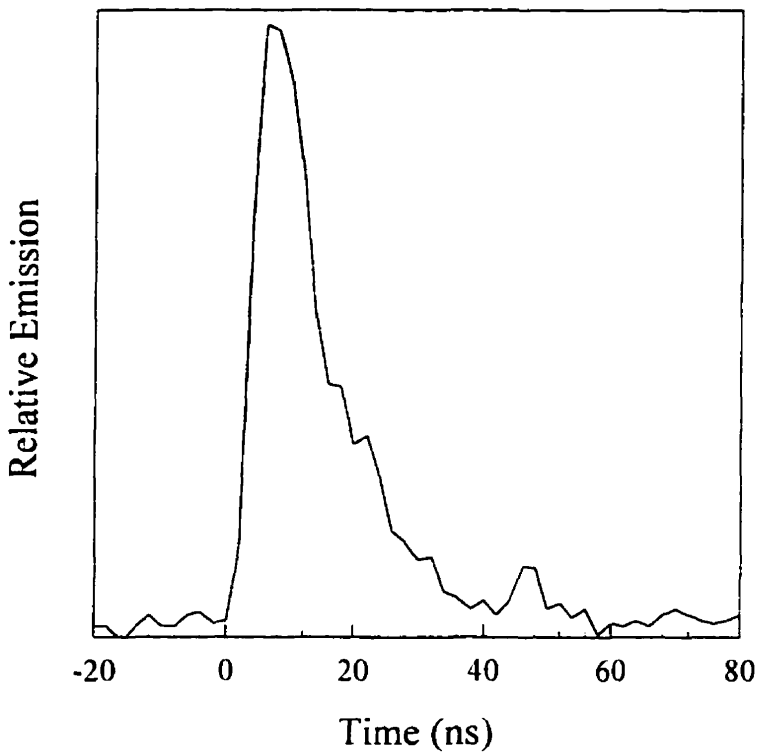

Figure 5.11: *The fluorescence decay time of the XeI emission from expansions of I_2 with 0.1 atm xenon and 1.3 atm argon.*

xenon alone. The largest signal for XeI* was observed for I_2 expanded with 0.1 atm xenon and 1.3 atm argon. The dependence of the signal intensity is a complicated function of both the total and partial pressures of the rare gases. A normalized table of the emission as a function of the total pressure and the fraction of Xe is compiled in Table 5.1

A surprising result is that the XeI* signal intensity is not linear with the excimer laser fluence. A log-log plot of the XeI (B→X) and the I_2 (D′ → A′) emission signal intensities as a function of excitation laser energy are shown in Figure 5.12. The XeI* has a slope of 1.8 which is indicates that the signal is resultant from a 2-photon process. In contrast, the I_2 (D′ → A′) signal intensity is linear with excitation laser energy as is expected for a one photon process. A comparison of the dependence of the XeI* emission intensity on 193 nm excitation in a room temperature gas cell (no clusters) and in a gas jet is shown in Figure 5.13. The slope of 0.7 for the log(energy)

	10 psi	20 psi	30 psi
1% Xe	—	0.42	1
5% Xe	—	1	0.16
10% Xe	0.03	0.40	0.06
20% Xe	0.45	0	—
30% Xe	1	—	—

Table 5.1: XeI signal as a function of partial pressures of expansion gases

vs log(XeI* emission) in the gas cell indicates a one-photon process as was previously assumed in the work of O'Grady and Donovan[42].

5.4 Discussion

Expansions of I_2 with helium and neon show only emission features attributable to fluorescence from the initially excited D state[8]. The fluorescence lifetime is within our experimentally resolvable limits ($\leq$ 20 ns), consistent with isolated I_2 being responsible[80]. No perturbations which could be attributed to clusters were observed for these expansion conditions.

Expansions of I_2 with 0.5 atm stagnation pressure of argon resulted in spectra which were identical to those measured with helium, except for a small peak at 341 nm. The peak is the result of either D$\rightarrow$D' relaxation followed by D' $\rightarrow$ A' emission[72] or due to mixing of the excited state as a result of cluster perturbation. Increasing the argon source pressure increases the intensity of this signal. The D' $\rightarrow$ A' emission occurs within a small fraction of the binary collision time, indicating that clusters are responsible. This peak is observed prominently for lowest pressures of krypton. Since kypton forms clusters more readily at low pressures[60] this is a further indication that clusters are responsible for this emission peak.

The "cluster band" observed in expansions of I_2 with 2 atm stagnation pressure of argon was first observed by Fei *et al.*[73]. In their experiments it was found to have an increasing red shift with increased cluster size to a maximum red shift to 400

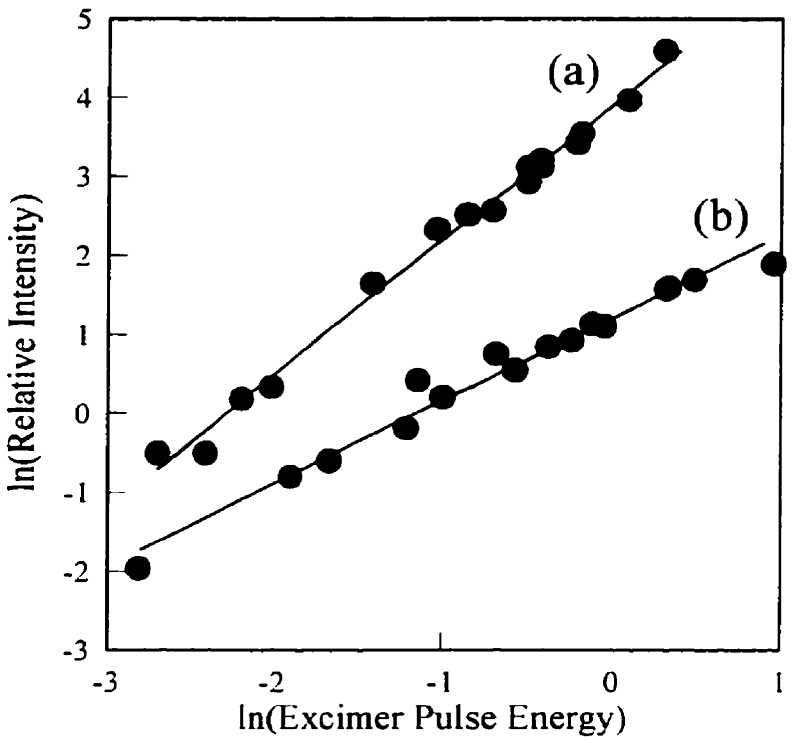

Figure 5.12: *Log-log plot of the laser pulse energy dependence of (a) the $D' \rightarrow A'$ emission intensity at 342 nm (slope = 1.0) and (b) the XeI^* emission intensity at 253 nm (slope = 1.8).*

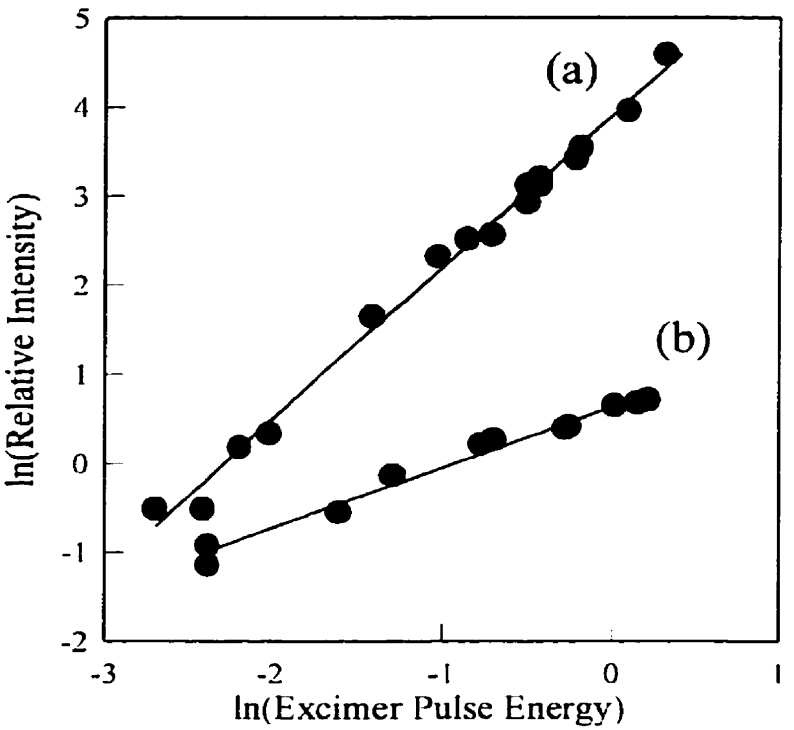

Figure 5.13: *Log-log plot of the laser pulse energy dependence of the XeI* emission in (a) a gas jet (slope = 1.8) and (b) a gas cell (slope = 0.7).*

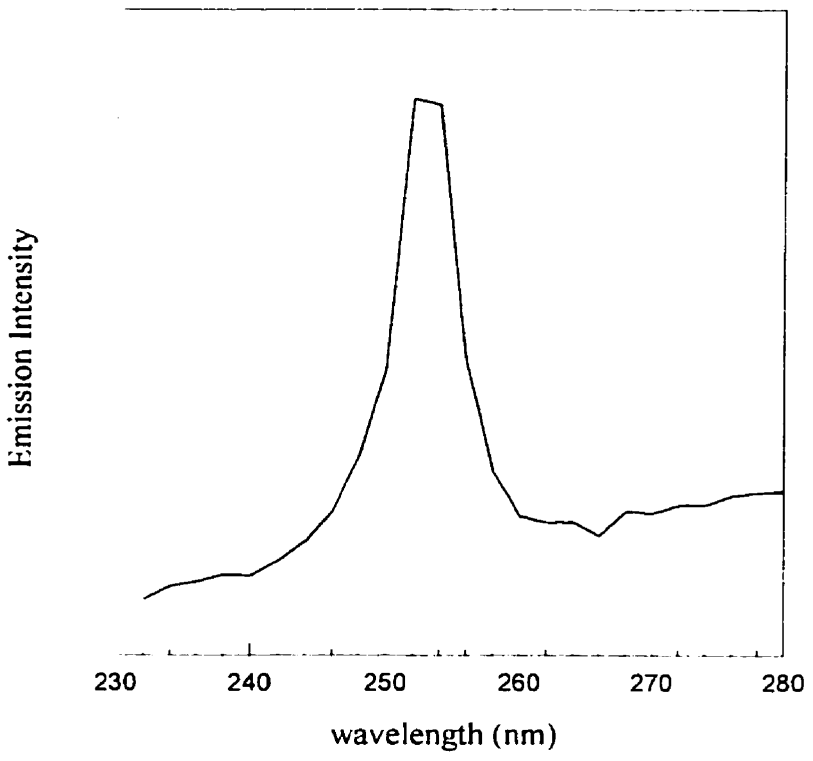

Figure 5.14: *Resolved fluorescence spectrum of XeI* $B \rightarrow X$ excimer emission, observed using an expansion mixture of $I_2 = 0.3$ Torr in 5% Xe in Ar with a total pressure of 1.3 atm. The intensity of this feature is stongly dependent upon the exact expansion conditions.*

nm. Macler and Heaven[9] used 193 nm radiation to excite I_2 embedded in Ar and Kr matrices, from this they observed a broad emission feature at 380 nm from the argon matrix and at 423 nm from the krypton matrix. We assign the "cluster band" emission to the same transitions as are observed in the matrix as do Fei *et al.*[73] The emitting state is best described as some admixture of the first tier ion-pair states.

Macler and Heaven attributed the unusually large red shift in the emission observed in the krypton matrices (5600 cm^{-1}) to the production of a charge transfer exciplex between excited I_2 and the Kr matrix. Based on the red-shift observed in the argon matrices and the relative polarizabilities of the two species, the expected red shift for krypton is 4400 cm^{-1}. The shift in the emission spectrum results from the interaction between the solvent atoms and the iodine atom. This interaction is primarily due to the dipole-induced dipole interaction term[1] and therefore the interaction will differ between argon and krypton by the ratio of their polarizabilities. Gürtler *et al.*[81] observed emission from $Cl_2(D' \rightarrow A')$ in Ar matrices which were shifted beyond that expected based on the spectra for Cl_2 in neon matrices. As well, the radiative lifetimes were noticeable longer than those observed for the gas phase species, that is longer than expected based on the Einstein A coefficient. The lifetime of the excited state is proportional to the inverse Einstein A coefficient; which is itself proportional to the third power of the emission frequency. Therefore decreasing the frequency of the emission increases the lifetime of the excited state. Gürtler et al.[81] assigned these transitions as to the $ArCl^{+} \cdot Cl^{-}$ charge transfer complex. Macler and Heaven[9] observed a large red shift which they attributed to an ion-pair to valence transition of I_2 in argon by analogy to Farado and Apkarian[40] who observed red shifts of up to 4700 cm^{-1} in XeCl ion-pair to valence transitions. Their results were reinterpreted[73] when results of expansions of I_2 in clusters of argon were made. Argon is known to readily admix the lowest tier ion pair states[72] of iodine. Both the A and A′ states were populated in the matrix experiments, but emission from the unperturbed D′ state would not be expected to terminate on the A state as a result of the $\Delta\Omega = 0$ propensity rule. Given this the emission was interpreted to be from an admixed ion-pair state to the A and A′ valence states.

Our results are consistent with the previous cluster and matrix experiments. For argon clusters we observe essentially the same emission bands with essentially the same pressure dependence as were observed by Fei *et al.* The only real deviation was in the measurement of the emission lifetime: our measurement was longer than that previously reported[73]. Our observation of a "cluster band" appearing in krypton with an increased red shift compared to that expected by the argon results is consistent with the matrix results of Macler and Heaven[9].

The lack of structure in the $I_2 \cdot Ar_n$ emission was attributed[73] to the interactions with the solvent molecules washing out the I_2 vibrational and rotational structure. In addition the range of sizes of clusters and rapid fragmentation of clusters by vibrational predissociation could cause homogeneous line broadenings. Excess internal energy in the I_2 molecule which is redistributed to vibrational modes of the solvent molecules can cause vibrational predissociation of the solvent molecules.

Our cluster experiments demonstrated an even larger red-shifting of the emission than what was observed in the matrix[73]. One possible explanation for this is that the cluster is more readily compared to a liquid species than to a matrix. Apkarian and co-workers[82][83][84] studied $Xe_2^+ I^-$ and $Xe_2^+ Cl^-$ in solid and liquid xenon. Due to solvation of the charge transfer complex, the transitions were appreciably redshifted from their gas phase positions. In addition, at temperatures close to melting point of xenon they found that redshifts in the liquid were approximately 5 nm greater than those of crystalline solid. They argue that the shift is greater in the liquid because of optimal solvation of the dipole could be achieved. In crystalline solid the degree of solvation was limited by competition with the host lattice forces. In other words, the optimum geometry for solvation of a specific molecule is not necessarily the same as that of the lattice. These arguments applicable to shifts in the I_2 seen in argon clusters and matrices provided we have observed "molten" clusters which are large enough to approximate a liquid state.

The clusters used in these experiments should be on the order of 60 atoms; this is large enough to approximate a solid or a liquid. The estimates of the cluster size are based on electron diffraction experiments of Fargas *et al.*[16][17] They expanded

pure argon through a 0.2 mm nozzle at 300 K and characterized the Ar_n clusters produced using electron diffraction techniques. Using an argon backing pressure of 2 atm. the average cluster size is about 60 atoms. with a distribution of sizes from 35 to 75 atoms. In addition, over 60% of the species in the expansion are clusters. These Figures would represent lower limits on the cluster sizes which would be found in our experiments. At the densities used in these experiments, the number of collisions, and hence the cluster size, is not dictated by kinetics[85]. Iodine will act as a more efficient site of nucleation. since its polarizability is much greater than that of either argon or krypton, and we are only studying the clusters which contain I_2. Also. since the van der Waals attractions are stronger for krypton than argon the clusters produced with krypton are expected to be even larger.

After the initial excitation of the I_2 molecule in the cluster. emission is observed from the lowest point on the D′ state which indicates that 11.500 cm^{-1} of energy has been dissipated. In argon clusters ion-pair states are stabilized by 2900 cm^{-1} with respect to valence states (assuming start with microcrystals)[9]. Therefore clusters dissipate more than 1.5 eV of energy before emission from $I_2(D'.v=0)Ar_m$. Based on this energy dissipation Fei et al[73] claimed it was likely that the emitting cluster were molten. One pathway through which energy may be dissipated in a cluster is by evaporation of atoms from the cluster. Simple thermodynamics calculations were made to determine the energy necessary to evaporate an Ar or Kr atom from a bulk solid at an initial temperature, T_0, of 20 K:

$$\Delta E = mC_v^s(T_m - T_0) + m\Delta H_{fus} + mC_v^l(T_v - T_m) + m\Delta H_{vap}$$

where m is the mass of the atom, C_v^s and C_v^l are the heat capacity of the atom in its solid and liquid phase respectively, ΔH_{fus} and ΔH_{vap} are the enthalpies of fusion and evaporation, and T_m and T_v are the melting and boiling temperatures for the atom. From these calculations, the energy necessary to evaporate a single argon atom is 600 cm^{-1} and a single krypton atom is 850 cm^{-1}. If this energy were exclusively dissipated by evaporation of rare gas atoms, it would take on the order of 20 atoms of Ar or 14 atoms of Kr to use up this excess energy. The "cluster"emission in Ar is

observed at 3000 cm^{-1} shift, compared to the D' $\rightarrow$A' emission, this would require the evaporation of 5 additional Ar atoms. The additional red shift of 6400 cm^{-1} for the Kr "cluster" peak would require the loss of an additional 7 atoms. These evaporation energies are an overestimate of the actual energy which would be lost from the cluster since they assume evaporation from bulk.

Although we observed the same cluster emission peak with jet expansion conditions similar to those used in the experiments of that Fei *et al.*[73], our measurements for the temporal profile of this emission were quite different. Fei *et al.*[73] determined an upper limit to the lifetime of this emission feature to be 10 ns. This is in contrast with the decay time of the convolution of the true emission decay signal and the laser profile measured for our experiments of 35 ns. since the laser has a fluence time of 10 ns the minimum lifetime of the emission would be 25 ns. Macler and Heaven[9] found the emission from I_2 in matrices has a lifetime of 5 ns. One difference between our experiments and those of Fei. et al. is that our interaction region is 18 nozzle diameters downstream from the nozzle, while their interaction region is 7 nozzle diameters. It is possible that the region in which Fei *et al.*'s[73] expansion is being studied is not a "collision free" regime. If that is the measured lifetimes of the emission are artificially reduced by collisional deactivation of the excited state species. Our measurements taking place in a truly collision free regime would not be affected by this deactivation process.

Previously, no emission from either I_2^{ip} nor chemiluminescence from XeI* from I_2-Xe_n has been reported from systems in condensed media or clusters[35]. We observe emission from I_2^{ip} as well as chemiluminescence from XeI (B$\rightarrow$X). The emission of XeI* at 253 nm[40] has been reported when gas phase I_2 was excited into its ion-pair manifold in the presence of xenon, while in the condensed phase, emission is observed at 390 nm and is assigned to Xe_2I^* exciplexes[82][83][84]. We do not observe any clear evidence for emission from Xe_2I^* exciplexes in our experiments. Our measurement of the emission decay of XeI(B), see Figure 5.11, is consistent with that of Hay et al[86] who measure the lifetime to be 12 ns.

5.5 Charge transfer model

Our results may be interpreted by proposing that a charge transfer exciplex is formed between the I_2^{ip} and the rare gas (RG) atoms. As discussed above, charge transfer complexes have been previously reported in X_2/RG matrices[81][82][83][84]. In our experiments, we attribute the fluorescence spectra from the rare gas clusters to a charge transfer species formed from an initial harpooning type electron transfer between a rare gas atom and the I_2^{ip}. The reaction between I_2^{ip} and Xe is generally attributed to this mechanism[42]. In this model, the "cluster band" represents emission from the $(RG^+ \cdot I_2^-)^*$ species, which may be solvated by the other rare gases in the cluster. Increasing the cluster size will increase the extent of solvation to the limit of fully solvated. This solvation will be in excess of that which would be experienced by the neutral species.

The "cluster band" represents fluorescence from the excited state $(RG^+ \cdot I_2^-)^*$ species, which may be solvated by other rare gas atoms in the cluster. The simulations of the potential energy surfaces for $I_2 \cdot (RG)_n$ based on the charge transfer model are displayed in Figures 5.17 to 5.19. The figures show calculated potential energy curves for I_2·RG in the X and D electronic states, as well as the $I_2^- \cdot RG^+$ charge transfer species with zero, one, and infinite solvating RG atoms. For a list of all of the constants used in these calculations see Tables 5.2 and 5.3. The Lennard-Jones potential terms used are actually the potentials calculated for the interaction between each of the rare gas atoms and a xenon atom. This approximation is made since the iodine atom has approximately the same van der Waals radius as xenon and each iodine atom within the I_2 molecule should behave approximately like a xenon atom. The geometry of the I_2·RG species is assumed to be T-shaped (see Figure 5.15) as that corresponds to the minimum potential energy[87][88].

The states corresponding to $I_2(X)$ + RG, $I_2(D)$ + RG, and $I_2(X)$ + RG+ $h\nu$ are modeled as the sum of two I-RG Lennard-Jones potentials corresponding to the

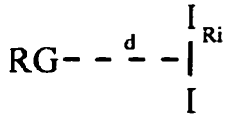

Figure 5.15: *Geometry of the I_2·RG species.*

interaction of each of the I atoms with the rare gas atom:

$$U(I_2(\mathrm{X}) + RG) = 8\epsilon\left[\left(\frac{\sigma}{\sqrt{d^2 + R_{i.X}^2}}\right)^{12} - \left(\frac{\sigma}{\sqrt{d^2 + R_{i.X}^2}}\right)^{6}\right]$$

$$U(I_2(\mathrm{D}) + RG) = 8\epsilon\left[\left(\frac{\sigma}{\sqrt{d^2 + R_{iD}^2}}\right)^{12} - \left(\frac{\sigma}{\sqrt{d^2 + R_{iD}^2}}\right)^{6}\right] + E_{\min}(\mathrm{D})$$

$$U(I_2(\mathrm{X}) + RG + h\nu) = 8\epsilon\left[\left(\frac{\sigma}{\sqrt{d^2 + R_{i.X}^2}}\right)^{12} - \left(\frac{\sigma}{\sqrt{d^2 + R_{i.X}^2}}\right)^{6}\right] + h\nu$$

where σ and ϵ are the Lennard-Jones constants. $R_{i.X}$ (R_{iD}) is $\frac{1}{2}$ the I_2 bond length in the X(D) state, and d is the distance between the I_2 species and the RG atom is varied. The value of $E_{\min}$(D) is 5.087 eV[89], it is the difference in energy between the ground state and the lowest ion-pair state. The value $h\nu$ is the energy available from the absorption of one photon of light at 193 nm. $h\nu$ = 6.42 eV. The potential term U(I_2(X) + RG + $h\nu$) is calculated to model the energy available to the dimer upon absorption of one photon of 193 nm radiation. The values for the Lennard-Jones potential terms (σ and ϵ) as well as the other constants are found in Tables 5.2 and 5.3.

The I_2^- + RG^+ charge transfer state, with no additional solvent atoms, is modeled by:

$$U(I_2^- \cdot RG^+) = IP(RG) - EA(I_2) - \frac{e^2}{4\pi\epsilon_0 d} + 8\epsilon\left(\frac{\sigma}{\sqrt{d^2 + R_i^2}}\right)^{12} - \frac{e^2\left[\alpha(RG) + \alpha(I_2)\right]}{2\left(4\pi\epsilon_0\right)^2 d^4}$$

where IP(RG) is the ionization potential of the rare gas atom and EA(I_2) is the electron affinity of I_2 and e is the charge on an electron. This potential combines the force of two ions interacting at larger distances and in the small distances limit it is the

interaction of two neutral species. The first three terms in this expression represent the ion-ion interaction terms. The fourth term is the Lennard-Jones repulsive potential acting between the individual I atoms and the rare gas atom. The last term is the ion-induced dipole energy for I_2^- acting on RG and RG^+ acting on I_2^-, using the assumption that the polarizabilities of the ions is the same as that of the neutral species. (Although this is not accurate, this term is a small compared to the ion-ion energies.)

When the charge transfer state is solvated by a rare gas atom, the minimum energy configuration for the species is a cross[88] as shown in Figure 5.16. The potential for

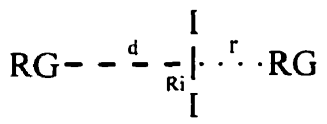

Figure 5.16: *Geometry of the $(I_2^- \cdot RG^+) \cdot RG$ species.*

the $(I_2^- \cdot RG^+) \cdot RG$ species, is given by

$$U((I_2^- \cdot RG^+) \cdot RG) = U(I_2^- \cdot RG^+) - \frac{e^2 \alpha(RG)}{2\,(4\pi\epsilon_0)\,r^4}$$

where r is the separation between the rare gas atom and the iodine molecule. The last term accounts for the solvation of the charge transfer state by the additional RG atom. In the fully solvated system the equation used is

$$U(I_2^- \cdot RG^+) = IP(RG) - EA(I_2) - \frac{e^2}{4\pi\epsilon_0 d} + 8\epsilon \left(\frac{\sigma}{\sqrt{d^2 + R_i^2}}\right)^{12} - \frac{e^2}{8\pi\epsilon_0}\left[\frac{1}{R_g} + \frac{1}{r_I}\right]\left(1 - \frac{1}{\epsilon_s}\right)$$

where r_I is the ionic radius of iodine. The sum of the solvation by the individual atoms is replaced by one which accounts for the shielding of the charges by the rare gas solvent[90]. The shielding term contains the value ϵ_S which is the dielectric constant of the rare gas solid[91]. The size of our clusters should be sufficient to fully solvate the I_2 molecule and this should be a reasonable value to use.

Even though these potential curves are model systems and many approximations are used in deriving these curves, there are still two important features which are

apparent in the potentials. The first feature is the increased stabilization of the charge transfer complex with increased solvation by the rare gas. The Figures are drawn to make this increased solvation readily apparent. The second feature relates to the position of the crossing point between the ion-pair levels and the charge transfer state. We believe these two features which account for the different spectra observed for the three species.

First we will look in detail at the potentials for the $I_2^- \cdot Kr^+$ charge transfer species (Figure 5.17). The minimum potential energy of the charge transfer complex decreases by 2 eV between that of the unsolvated species and the fully solvated species. The large change in potential is consistent with the large red-shift observed in the Kr cluster experiments. The other feature that we are interested in is the position of the crossing point between the ion-pair and charge transfer potentials. Knowing the crossing point is very important in determining transition probabilities. This crossing point shifts to longer I_2-Kr distances with increasing solvation.

Although the point of the crossing is dependent on the specific values used for the potentials, the trend is independent of the details. The implication is that the likelihood of charge transfer state formation is a function of the cluster size. The Franck-Condon principle requires that the curve crossing take place where the geometry of the initial species matches that of the final species. The dependence of the location of the crossing point on the solvation implies that the surface crossing can be "solvent tuned" into and out of the Franck Condon accessible region of the initially excited state[92].

In $I_2 \cdot Kr$ the calculated van der Waals bond length in the ground state is 4.2 Å. According to the Franck-Condon accessible model, the surface crossing with the charge transfer state is available when the number of Kr solvent atoms is between one (Figure 5.17b) and infinity (Figure 5.17c). In our experiments we observe the "cluster band" at almost every backing pressure used, which implies that the crossing point lies close to the Franck-Condon region even in unsolvated $I_2 \cdot Kr$.

In the argon cluster experiments, the cluster band initially appears at reasonably high argon stagnation pressure. This implies that either the charge transfer states are

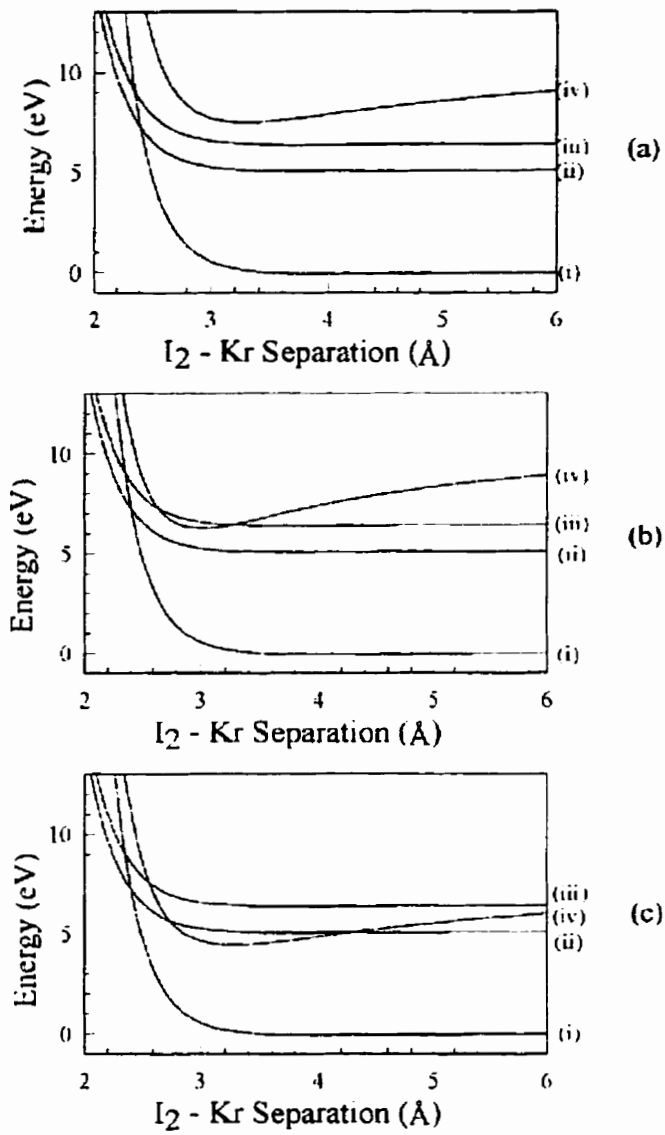

Figure 5.17: *Model potential curves for I_2·Kr "solvated" by Kr. In each of (a), (b), and (c), the curve labelled (i) represents $I_2(X)$·Kr; (ii) $I_2(D)$·Kr; (iii) $I_2(D)$·Kr shifted up in energy to 6.42 eV (ie 193 nm); (iv) I_2^-·Kr^+. (a) No additional Kr atoms resent; (b) one additional Kr present; (c) completely solvated by Kr.*

not energetically accessible or the charge transfer- ion-pair state surface crossing is not in the Franck Condon accessible region. The calculated potentials in Figure 5.18, indicate that the surface crossing does not take place, because this is less favorable for argon clusters compared to krypton clusters both in terms of energetics and in terms of the Franck Condon accessibility. In the "fully solvated" model, Figure 5.18c, there is only a small interaction region between the charge transfer states and the ion-pair states.

The formation of XeI* by one photon in the unclustered environment, but with two photons in the cluster may be explained by this model. The model potential curves for the I_2·Xe system are shown in Figure 5.19. The charge transfer state for this system lies lower in energy than the corresponding potentials for argon and krypton clusters. The crossing point between the initially excited level at 193 nm and the charge transfer curves lies at longer distances than the 4.4 Å equilibrium separation in the ground state of the complex, even in the unsolvated system. The crossing between the bottom of the state potential and the charge transfer state for the unsolvated species is well below the equilibrium separation and therefore not Franck Condon accessible. Increasing the solvation makes this crossing region even more inaccessible to the initially excited species. As a result formation of XeI* with a single photon is impossible.

One possible scenario is that the first 193 nm photon is absorbed in the complex and the initial excited state species is rapidly quenched by the surrounding xenon atoms. The energy deposited into the cluster modes could cause fragmentation of the solvent atoms. As the I_2 and Xe separate, a second photon may be absorbed while the separating partners cross through the internuclear distances over which the charge transfer ion-pair state surface crossing occurs. The XeI* product formed would then be a mirror image of that formed in the unclustered environment, since both approach the curve crossing while increasing the internuclear separation.

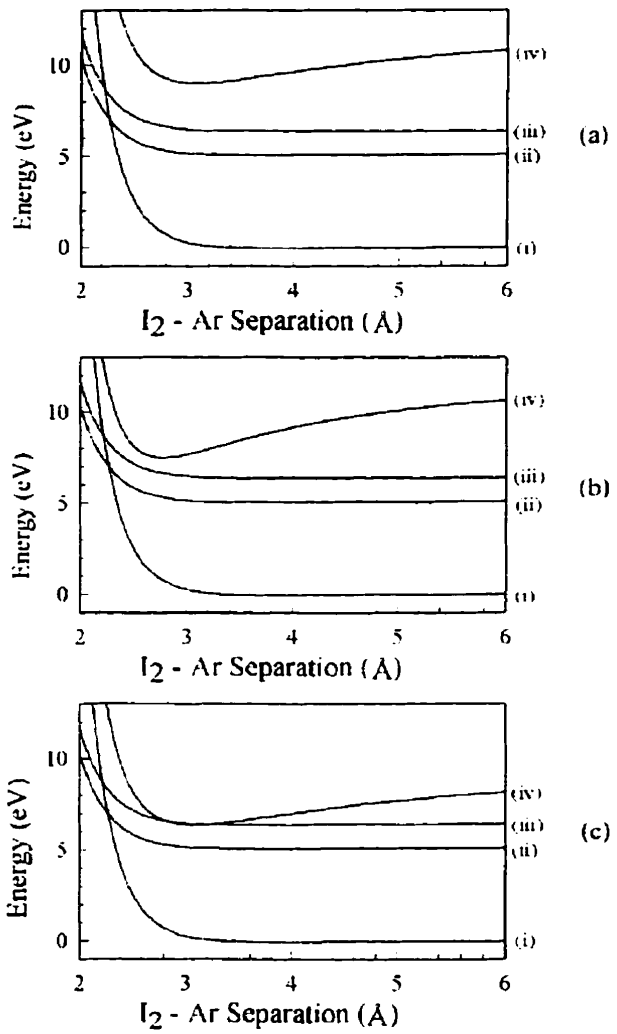

Figure 5.18: *Same as previous figure, but for the I_2·Ar system.*

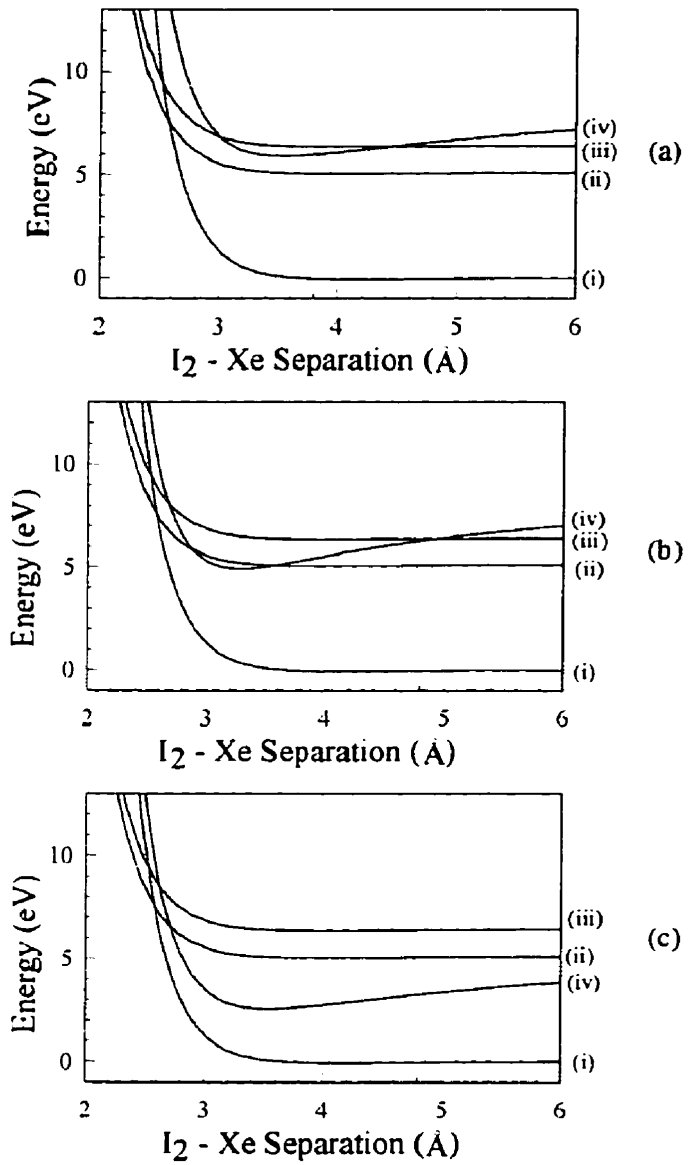

Figure 5.19: *Same as previous two figures, but for the $I_2 \cdot Xe$ system.*

	argon	krypton	xenon
Lennard Jones potential terms, ϵ[5]	187.4 cm^{-1}	231.1 cm^{-1}	282.3 cm^{-1}
σ[5]	3.62 Å	3.72 Å	3.88 Å
van der Waals radii, radius R_g[93]	1.90 Å	2.00 Å	2.20 Å
ionization potential, IE[94]	15.76 eV	14.00 eV	12.13 eV
polarizability, α[94]	1.641 Å	2.484 Å	4.044 Å
Rare Gas- I_2^- separation, r(Å)	3.0	3.2	3.5
dielectric constant in solid, ϵ_S[91]	1.58	1.78	2.01

Table 5.2: Rare gas parameters for model potentials

I_2 electron affinity, EA[94]	2.55 eV
ionic radius, radius I[94]	2.15 Å
I_2 bond length, X-state[94]	2.66 Å
D-state[89]	3.58 Å
I_2 polarizability[94]	12.86 $Å^3$

Table 5.3: I_2 parameters for model potentials

Chapter 6

HI cluster experiment

6.1 Introduction

Previous experiments which were performed by this group[78][62] have investigated a photochemical reaction which does not occur in an unclustered environment. Dimers of methyl iodide absorb one photon of 248 nm radiation and form ground electronic state I_2. It was determined that the dimer species was responsible for the observed I_2 signal. Neither ground state I nor spin-orbit excited I^* atoms may react with methyl iodide to form I_2 under the conditions investigated in the experiments. Thus, it was determined that a cluster induced cooperative effect is responsible for producing the I_2 product.

A variety of other alkyl halide systems were investigated[13]: methyl, ethyl and propyl iodide, hydrogen iodide, trifluoromethyl iodide, trifluoroethyl iodide, methyl and ethyl bromide, and a co-expansion of methyl iodide and methyl bromide. These clusters were excited at both 248 and 193 nm. All of the iodo containing compounds with the exception of CF_3I produced I_2 product. No Br_2 was observed from the excitation of the bromide species, nor was IBr observed from the excitation of the mixed clusters.

In these experiments ground state was formed as a product of HI cluster photolysis

at 193 and 248nm. The I_2 product was only observed with high pressures of HI (neat HI expanded at pressures greater than 1 atm). Since HI clusters readily due to the attractive nature of the intermolecular potential between HI molecules[95], large clusters would be formed at these pressures and would be responsible for the production of I_2. A linear dependence of the I_2 signal on the HI pressure is further evidence that large clusters are responsible. If dimers of HI were responsible for the production of the I_2 signal, the signal would depend quadratically on the gas pressure as was observed in the methyl iodide expansions. The scaling for larger clusters does not go as pressure to the n-th power. When the fraction of the species in the expansion which is clustered increases the kinetic equations from which the scaling laws are derived break down. The formation of a large clusters results from collisions of smaller clusters[32].

A cooperative effect, in which two reactions occur simultaneously, was observed in the photochemical reaction of surface aligned $(HX)_n$ complexes. Polanyi and co-workers[96] photolyzed HX (X = Cl and Br) absorbed on a LiF(001) surfaces and observed equal amounts of H_2 and X_2 desorbing from the surface. The bimolecular photoreaction $2HX + h\nu \rightarrow H_2 + X_2$ occurring between aligned adjacent HX molecules was proposed as the source of the H_2 and X_2 products. Although the ground state four-center reaction of hydrogen halide molecules is forbidden on orbital symmetry grounds[97] in the ground electronic state, the reaction of electronically excited state is allowed.

A similar mechanism is proposed by Buntine *et al*[10] to explain the appearance of translationally cold and ro-vibrationally excited H_2 product in their experiments. In their experiments a 218 nm photoexcitation of the species within a neat HI expansion produces H_2 which is ionized using resonance-enhanced multiphoton ionization and imaged onto a position sensitive detector. By this means the translational energy of the H_2 product may be measured. They observe two species of H_2. The fast species of H_2 is attributed to the reaction $H + HI \rightarrow H_2 + I$. The authors speculate that the slow H_2 species which they observe result from the four center reaction $(HI)_2 \rightarrow H_2 + I_2^*$ within a single cluster.

Young and co-workers[11][12] detected I_2^+ produced from laser excitation of HI clusters in a seeded expansion of HI followed by REMPI detection. The observed I_2^+ signal depended on the laser energy to the 3.6 power. Thus 3.6 photons are required to break the two HI bonds and to ionize the I_2 product. This signal was attributed to two photons breaking HI bonds producing ground state I_2 followed by a two photon ionization of the iodine molecule, in contrast to our previous conclusions[13]. The authors did not attribute the observed signal to a four center mechanism.

In this chapter evidence is presented for the formation of electronically excited molecular iodine, I_2^*, as a product of HI cluster photolysis. The evidence is the emission observed from the ion-pair states of I_2 when HI clusters are photolyzed at 248 nm. The emission depends quadratically on the laser intensity and quartically on the stagnation pressure of neat HI. These results along with the work of Polanyi[96] and Buntine *et al.*[10] provide strong evidence that the four center photoreaction takes place in HI clusters. The joint formation of I_2 and I_2^* might bring the results of Young[11][12] and our early results into agreement. The work presented here was published as "Evidence for a four-center mechanism in the photoreaction of HI clusters" in The Journal of Physical Chemistry, **99**:6763-6766, 1995.

6.2 Results

Neutral clusters of HI were prepared in a supersonic jet expansion of neat HI with a 0.5 mm orifice. The clusters were photolyzed 10 nozzle diameters downstream with a KrF laser (248 nm), the output of which had pulse energies of 0.15 to 5 mJ per 10 ns pulse. The resolved emission produced from the photolysis reaction was measured.

Upon excitation of HI clusters with 248 nm radiation, emission originating from the iodine ion pair states, I_2^{ip} is observed, see Figure 6.1. This emission is attributed to the I_2 : F, D and D′ states[68] and appears promptly within the 5 ns rise time of the detection electronics. Except for the total fluorescence intensity, the emission spectrum is constant with changing the HI stagnation pressure. No emission features

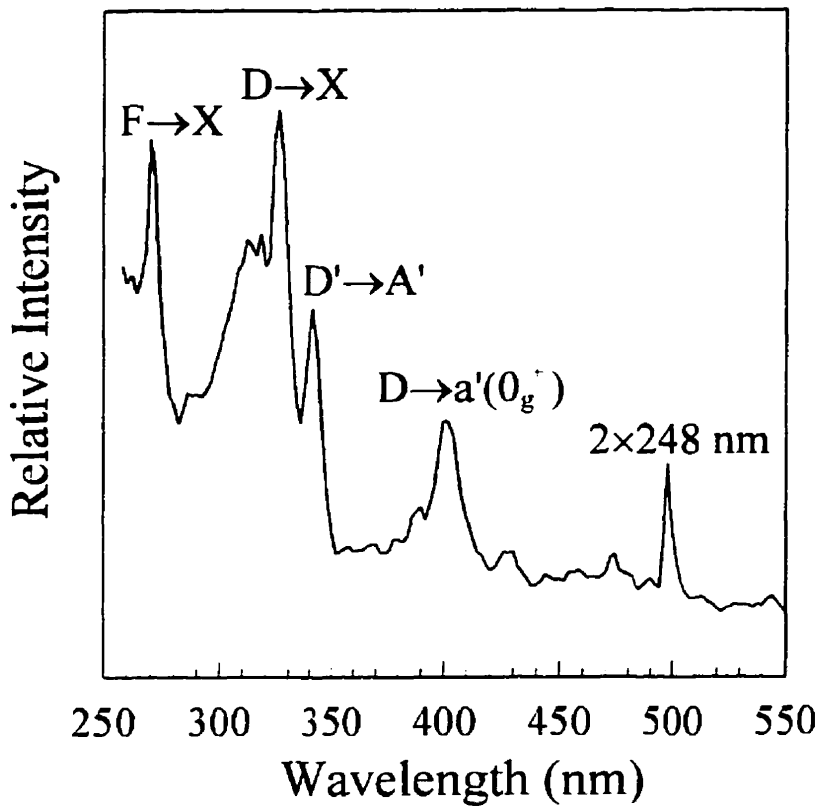

Figure 6.1: *Emission spectrum from I_2 ion pair states observed folowing 248 nm excitation of HI clusters. The spectrum was obtained at an HI stagnation pressure of 1300 Torr.*

due to the A, A', or B states of I_2 was observed within the signal to noise ratio of these experiments. Little emission was observed from irradiating I_2 expanded with 1 atm He at 248 nm (see Figure 6.2).

The temporal profiles of the D and D' states of I_2 (see Figure 6.3) show that the lifetimes are 20 and 22 nsec respectively with an uncertainty of $\pm$ 4 nsec. These agree within the uncertainty in the lifetimes measured when I_2 was excited directly to the ion-pair states with 193 nm radiation.

The dependence of the I_2 D state emission intensity on the laser pulse energy was measured for energies between 0.15 and 3.8 mJ/pulse (see Figure 6.4) incident on the chamber. Below 1.5 mJ/pulse this emission has a two-photon dependence. The

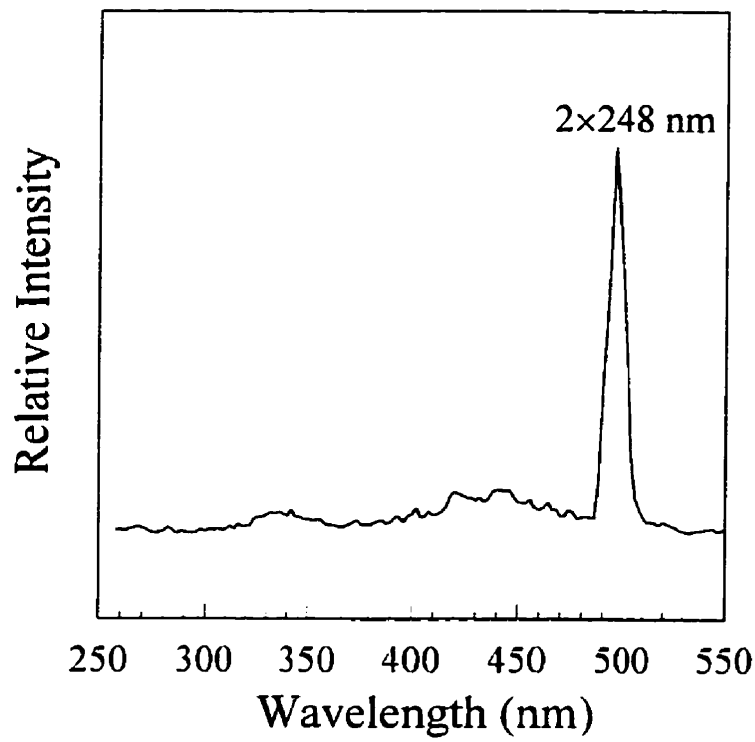

Figure 6.2: *Emission spectrum observed following 248 nm excitation of I_2 expanded with 760 Torr of helium. The peak at 496 nm results from the second order diffraction of the scattered laser light.*

log-log plot shown in the insert to Figure 6.4 has a slope of 2.3 ± 0.3 in the lower energy regime; this implies that a two photon process is responsible for populating the ion-pair states. The emission intensity of the I_2 D′ emission[72] (see Figure 6.5) also demonstrates a two photon dependence. The log-log plot shown in the insert of Figure 6.5 has a slope of 2.4 ± 0.3, thus we conclude that two photons are required to produce I_2^{ip} whose emission we observe.

The dependence of the I_2 D state emission on the stagnation pressure of HI was also measured, see Figure 6.6. From the log-log plot shown in Figure 6.6 the intensity of the emission signal has a dependence on the 4.1 ± 0.2 power of the HI stagnation pressure for pressures up to 700 Torr. This implies that HI dimers and trimers are involved in the production of I_2^{ip}. For low pressure expansions, the dependence of dimers on the pressure is third power or greater, since at least one "third body" is

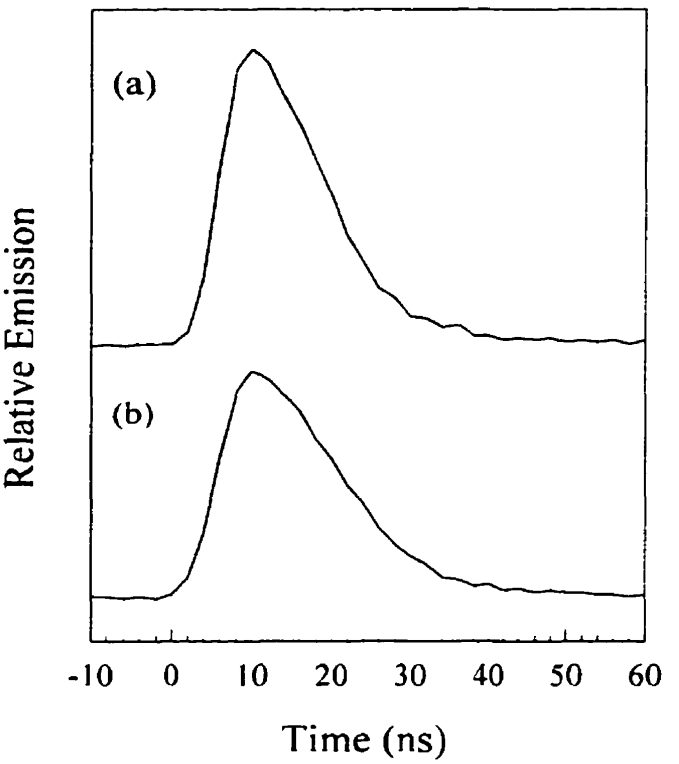

Figure 6.3: *Time resolved fluorescence observed for the I_2 ion pair states following 248 nm excitation of HI clusters: (a) D state (325 nm) and (b) D' state (341 nm).*

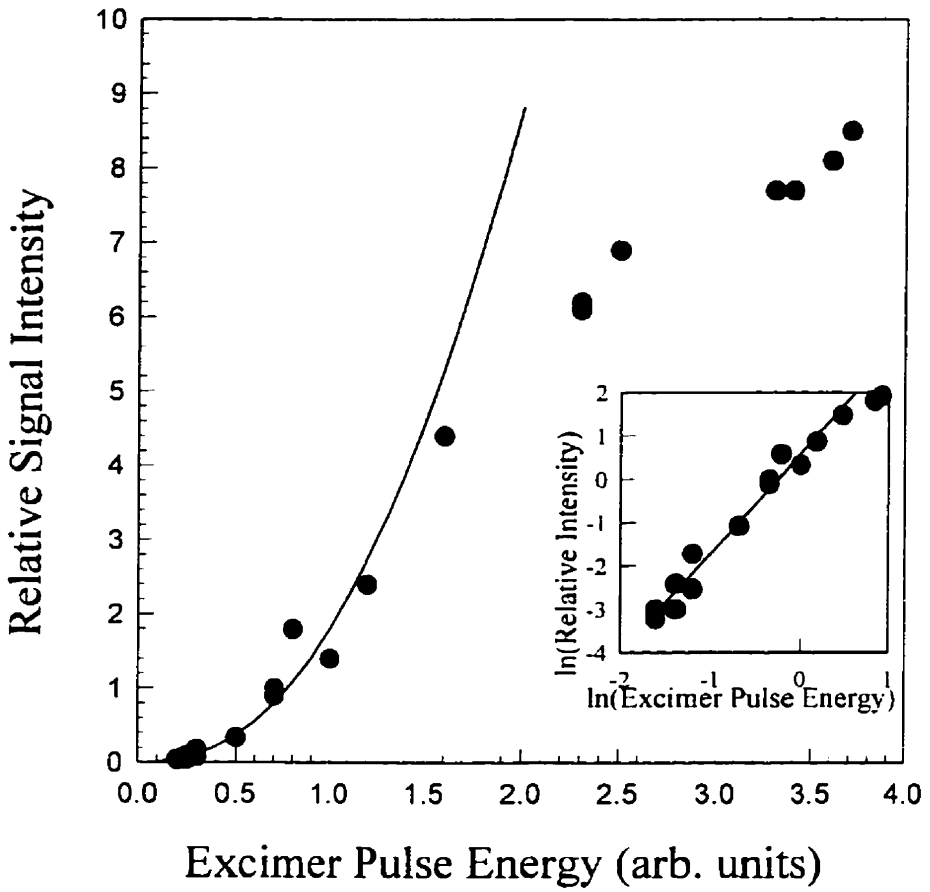

Figure 6.4: *Laser power dependnce of the D⟶X emission feature at 325 nm. The laser pulse energies range from 0.15 to 3.2 mJ/pulse. The solid line shows a quadratic fit to the low intensity data. The inset shows a ln-ln plot of the data. The solid line is a fit to the data and has a slope of 2.3 ± 0.3.*

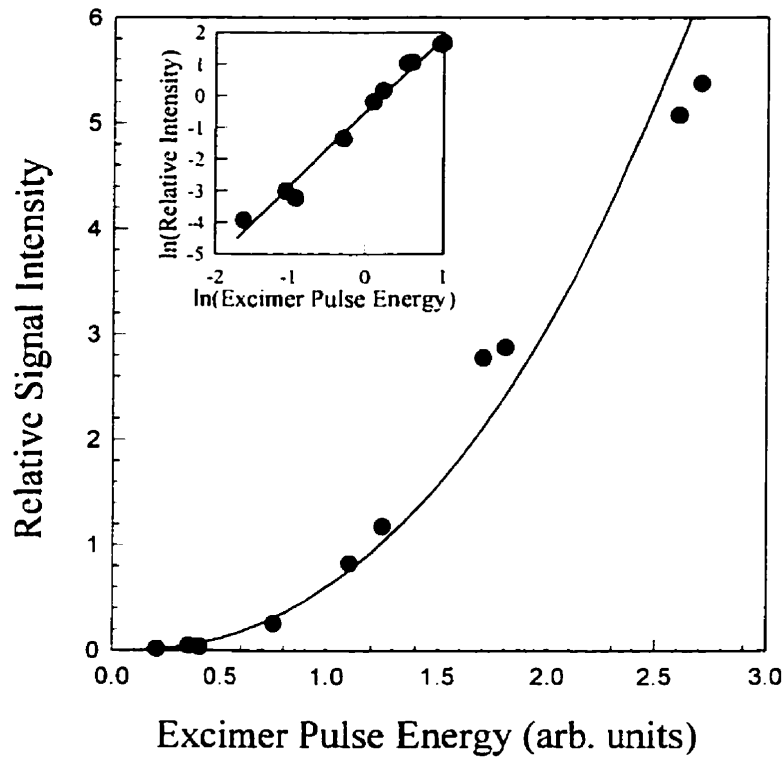

Figure 6.5: *The laser power dependence of the $D' \rightarrow X$ emission at 341 nm also has a slope of 2.4 ± 0.3. This is shown in the ln-ln plot in the insert, where the solid line has a slope of 2.3.*

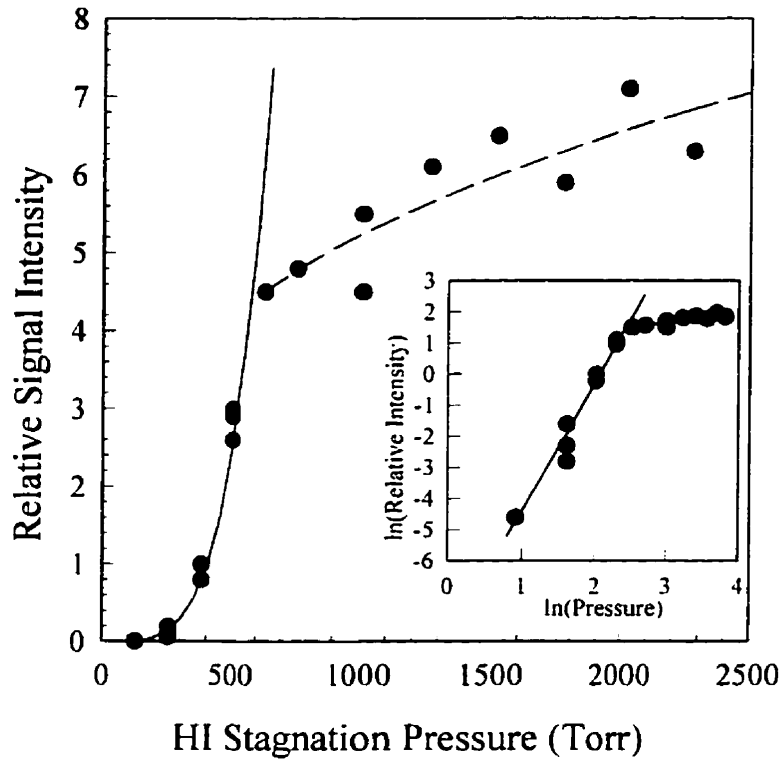

Figure 6.6: *Stagnation pressure dependence of the intensity of the I_2:D⟶X ion pair state emission. The solid line at pressures below 700 Torr shows at quartic fit to the data. For pressures above 700 Torr the signal is obseved to depend on the cube root of the pressure, as shown by the dashed line. The inset figure is the ln-ln plot of the same data, with the pressure dependences indicated.*

required to carry away excess energy. Trimers are formed with a pressure dependence of four from collisions between dimers which create a trimer and a monomer. The monomer removes excess energy from the complex. For pressures greater than 1 atm the signal varies by the cube root of the pressure, which indicates the onset of another mechanism to I_2 formation from HI cluster photolysis.

6.3 Discussion

In work done previously in this group[13] cold ground state I_2 product was detected from single photon excitation of HI clusters. In those experiments ion-pair state

emission could not have been detected, since the optical filters used for I_2 B $\leftarrow$ X laser induced fluorescence, LIF, would not pass light for $\lambda < 590$ nm. A significant difference between the current results and those reported previously by this group[13] is that the I_2 ground state product had an appearance threshold of approximately 1 atm and above that pressure the LIF signal is linear with HI backing pressure (slope of ln(intensity) vs. ln(pressure) = 1.12 ± 0.05). These results in conjunction with the current results strongly indicates that the ground state I_2 and the I_2^{ip} products are formed by different mechanisms.

There are many two photon mechanisms which could result in the formation of I_2^{ip} from HI clusters. The time scale for the observed emission rules out all but same cluster reaction mechanisms, since intercluster reactions occur on a time scale of tens of microseconds (see Section 4.2.1). The emission intensity from each of the ion-pair states maintain a constant ratio of spectral line intensity as the stagnation pressure of the HI gas changes by more than a factor of two from 1.7 atm to 3.7 atm; this indicates that all of the ion pair emission has a common origin. The enthalpies of formation for each of the relevant species are shown in Table 6.1 and the enthalpy of formation of species within the cluster is assumed to be the same as the enthalpy of formation of the species in the gas state. The energy of a 248 nm photon in the appropriate units for these calculations is 482.37 kJ/mol. The enthalpy of formation of ro-vibrationally excited ground state I_2 is given as #, because the only constraint on it is that it be less than 213.68 kJ/mol, which is the dissociation energy for ground state I_2[98]. The enthalpy of formation of I_2^{ip} is taken to be the enthalpy of formation of I_2(D) which is one of the states of the lowest tier of ion pair states.

		$\Delta H_f(25°C)$
A.	$(HI)_n + h\nu \longrightarrow H + I + (HI)_{n-1}$	-184.1 kJ/mol
	$I + (HI)_{n-1} \longrightarrow I_2 + H + (HI)_{n-2}$	147.1 kJ/mol
	$I_2 + h\nu \longrightarrow I_2^{ip}$	-78.7 kJ/mol

		$\Delta H_f(25°C)$
B.	$(HI)_n + h\nu \longrightarrow H + I^* + (HI)_{n-1}$	-93.0 kJ/mol
	$I^* + (HI)_{n-1} \longrightarrow I_2 + H + (HI)_{n-2}$	56.1 kJ/mol
	$I_2 + h\nu \longrightarrow I_2^{ip}$	-78.7 kJ/mol

In both mechanisms A and B the first photon dissociates an HI molecule. The iodine atom produced subsequently reacts with another HI molecule and produces an iodine molecule. Neither mechanism is likely to occur based on the highly endoergic second step in the mechanism. As well, the I atom will not have sufficient kinetic energy to overcome any barrier, since the photodissociation of HI places most of the excess energy into the H atom translation[11]. Correlation diagrams for I^*+ HI → I_2+ H [78], show that the spin-orbit excited state of I correlates with electronically excited I_2. Ground state I_2 could only be formed in the cluster, as would be required for the second step of B, if the cluster induces a nonadiabatic transition to a single reactive potential energy surface.

		$\Delta H_f(25°C)$
C.	$(HI)_n + 2h\nu \longrightarrow 2H + 2I + (HI)_{n-2}$	-368.2 kJ/mol
	$2I \longrightarrow I_2^{ip}$	252.4 kJ/mol
		$\Delta H_f(25°C)$
D.	$(HI)_n + 2h\nu \longrightarrow 2H + 2I^* + (HI)_{n-2}$	-186.2 kJ/mol
	$2I^* \longrightarrow I_2^{ip}$	70.5 kJ/mol

Mechanisms C and D require two photons to dissociate two HI molecules. The iodine atoms produced recombine to form molecular iodine in its ion-pair state. Neither mechanism C nor D is likely to produce the observed signal, since I_2^{ip} does not correspond to two iodine atoms or to spin orbit excited iodine atoms. (There is no appropriate curve crossing)

		$\Delta H_f(25°C)$
E.	$(HI)_n + h\nu \longrightarrow 2H + I_2^{\#} + (HI)_{n-2}$	#-99.5 kJ/mol
	$I_2^{\#} + h\nu \longrightarrow I_2^{ip}$	-# -78.7 kJ/mol

The first photon is used to produce ro-vibrationally excited ground state iodine, $I_2^{\#}$ and the second photon excites this species to the ion pair states. This mechanism is unlikely, 248 nm light does not excite low-lying v levels (those populated at room temperature and below) of I_2 to the ion-pair states. The large difference in the bond length of the ion-pair states compared to that of the ground state leads to small Franck-Condon factors for such transitions. This mechanism could be possible it the $I_2^{\#}$ formed in the first step had sufficient vibrational excitation to allow favorable Franck-Condon factors. However, previous experiments by this group[13] showed that only vibrationally and rotationally cold ground electronic state I_2 is produced by 248 nm photolysis of $(HI)_n$. Also, I_2 which is formed in the ground state, is formed with a very different stagnation pressure dependence than that which is observed for the ion-pair state iodine product.

The following mechanisms which differ only in which excited state the I_2 is initially produced, were suggested in the work of Buntine *et al*[10] In their experiments, neat expansions of HI were photolyzed at 218 nm and they observed H_2(v=1) with very little translational energy

		ΔH_f(25°C)
F.	$(HI)_n + h\nu \longrightarrow H_2 + I_2(A) + (HI)_{n-2}$	-330.69 kJ/mol
	$I_2(A) + h\nu \longrightarrow I_2^{ip}$	-220.91 kJ/mol
		ΔH_f(25°C)
G.	$(HI)_n + h\nu \longrightarrow H_2 + I_2(B) + (HI)_{n-2}$	-285.78 kJ/mol
	$I_2(B) + h\nu \longrightarrow I_2^{ip}$	-265.79 kJ/mol

The reactions described in mechanisms F and G require that the reaction take place *via* a four-center reaction. That one of the products is born in an electronically excited state from the four center reaction is required by the Woodward-Hoffman rules[97]. If this four center mechanism was responsible for the signal observed by Buntine *et al.* then the I_2 must be born in an electronically excited state. This process is energetically favorable. There is in fact enough energy to populate the I_2 ion-pair states directly. We consider this unlikely based on our measurement that the power dependence of the I_2^{ip} emission intensity is two-photon. Although laser power

species	$\Delta H_f(25°C)$
H	217.97 kJ/mol[94]
H_2	0.00 kJ/mol[94]
HI	26.49 kJ/mol[94]
I	106.84 kJ/mol[94]
I^*	197.80 kJ/mol[99]
I_2	62.44 kJ/mol[94]
$I_2^{\#}$	62.44 + # kJ/mol[94]
$I_2(A)$	204.66 kJ/mol[94][98]
$I_2(B)$	249.56 kJ/mol[94][98]
$I_2(D)$	466.12 kJ/mol[94][98]

Table 6.1: Thermodynamic constants used in calculations of the energetics of possible reactions occuring in HI clusters.

studies are not a conclusive measurement, the results rarely overestimate the number of photons involved in a multiphoton process. In addition, symmetry requirements favor a two step population of the ion-pair states. The initial excitation of $(HI)_n$ with the first photon corresponds to exciting a Π state in the HI monomer. Both the ground state of H_2 and the I_2 ion-pair states have Σ symmetry[98], that is the coordinate of the angular momentum along the internuclear axis is zero. The A, A', and B states of I_2 have Π symmetry[98]. The (Λ, S) coupling scheme labels are not strictly true for HI and I_2 in which the coupling of the angular momentum to the spin is important. The (Ω, ω) coupling scheme is the most appropriate for HI and I_2, in which the angular momentum and spin for each electron are coupled to one another and then all but the outermost ω are added together and then subsequently ω for the outermost electron is included. Although the (Λ, S) coupling scheme is not strictly followed this suggests a greater propensity to populate the A, A', and B states of I_2.

In proposing this mechanism as the one responsible for the ion-pair emission which we observe, it would be desirable to observe emission from the initially excited states. Our apparatus is capable of observing emission at the appropriate wavelengths for

these states. However, the A and A′ states have lifetimes of hundreds to thousands of microseconds[100] and with our present apparatus we would not see such weak emission. One limitation to our measurements is that the gas beam is only within the acceptance cone of the fiber optic for less than 5 μs based on the initial velocity of the beam. There should be little energy disposed to translation, since the iodine atoms compose the majority of the weight of the system it is expected that the nascent iodine molecule will travel with approximately the initial beam velocity, thus only a small fraction (< 2.5 %) of the actual emission would be observed with our apparatus. In the work of Buntine *et al.*[10] the H_2 signal which they attributed to molecular clusters was observed to have low translational energy. Since H_2 is significantly lighter than molecular iodine, it is not likely that the I_2 product would be born with more translational energy than the H_2 product. Given that neither product will have significant translational energy the I_2^* will likely have considerable vibrational and rotational energy and would be born in a large range of (v,J) levels. The combination of a broad emission in both energy and time would make this signal difficult to observe. The broad internal population distribution would also make observation of emission from the brighter B state difficult.

The quartic dependence of the I_2^{ip} emission implies that dimers and trimers are the precursors of this reaction. The geometry of the HI dimer has been calculated[95] (see figure 6.7); the angles shown are $\theta_1 = 3.3^\circ$ and $\theta_2 = 91.7^\circ$ and the bond length. R_e, is 5.14 Å.. The geometry of the trimer has not been calculated nor have either been

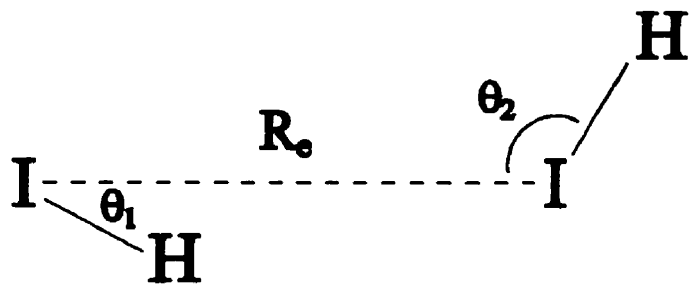

Figure 6.7: *The geometry of the HI dimer.*

determined experimentally. If it is the trimers which are primarily responsible for our observed emission, it might be that the geometry of the trimer is more favorable for allowing this four-center reaction. In this case, the third molecule might act like a solid surface to align the reacting pair[96]

In our experiments it was found that production of I_2^{ip} is favored at lower stagnation pressures and at higher pressures a mechanism is opened up for the production of ground electronic state I_2. The ion-pair emission might be attenuated because the I_2^* intermediate state is efficiently quenched by HI. The efficient quenching of I_2(B) by Ar, Kr, and Xe is discussed in Appendix A of this thesis with regard to measuring I_2 LIF signals. Also, the mechanism for the single photon production of ground state I_2 which only becomes available in larger clusters might be more favorable. In Figure 6.8, the pressure dependence of the two signals, separately normalized are displayed. From this it is clear that over a certain range both product channels are available. If this is true then it would bring our previous results[13] and those of Young and co-workers[11] into agreement. It might be that Young and co-workers[11] measured both species. The ground state I_2 produced with single photon excitation would require a 3 photon ionization for their detection. The ion-pair state I_2 product is formed with 2 photons and its ionization would require a third. This combination of processes could result in the 3.6 photon dependence observed by Young and co-workers.[11]

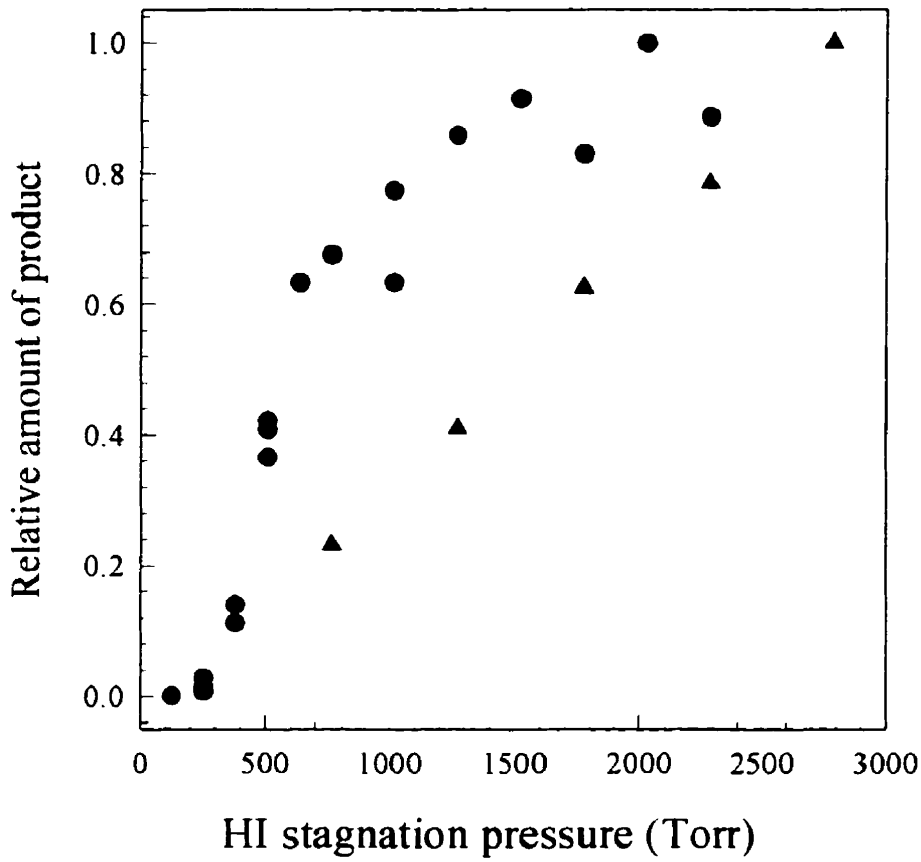

Figure 6.8: *Comparison of the pressure dependence of the excited state (•) and ground state (▲) I_2 signal seen in HI cluster photolysis. An absolute intensity comparison is not possible with our present techniques; therefore each dependence is normalized to its own maximum.*

Chapter 7

Collision-induced disorder in liquid crystal films

7.1 Introduction

Understanding the processes involved in the collision of gas phase molecules with a liquid surface is important to many processes such as the uptake of pollutants by water droplets in clouds, gas phase chromatography and heterogeneous catalysis[14]. Gas liquid scattering can yield information on surface structure and rigidity, energy transfer, the attractive forces between gas and liquid molecules, and the dynamics of gas-liquid collisions[101][43][44][102][45][46][103][104][14][47][105]. However, few studies of gas liquid interactions have been performed.

Molecular beam techniques were first applied to study gas-liquid collisions in 1959 by Hurlbut and Beck[106]. Sinha and Fenn[107] measured the scattering of argon atoms off a fresh continuously renewed surface of liquid glycerol. Their results showed that argon atoms recoil in a lobular pattern which indicates that direct collisions and thermal desorption from the liquid can be distinguished. Olander *et al*[101] studied the effect of the solid-liquid phase transition on the reactive scattering of Cl_2 with

indium, lead, bismuth, and tin. Only with bismuth is there a difference in the reaction kinetics of Cl_2 with the metal surface between the solid and liquid state.

Experiments performed by Naaman and co-workers[43][44][102] explored the scattering of monatomic and diatomic gases from organized organic monolayers. Their results showed that the "stiffness" (degree to which the molecular motion is restricted) of the surface determines whether the "direct" (impulsive) scattering or "trapping-desorption" (atom has multiple collisions with the surface before scattering) occurs. Nathanson and co-workers[45][46][103][104][14] have explored inelastic scattering of various gases (primarily rare gases) from liquid surfaces. They also studied the relative importance of the "direct" scatter and "trapping-desorption" channels and found the trapping probability is determined by the enthalpies of solvation[46].

McCaffery and co-workers[47][105] measured the internal state distribution of a gas scattered off a series of liquid interfaces. In their experiments I_2 was scattered off methyl-substituted polysiloxane, perfluorinated polyethers, and Ga (solid and liquid). The internal energy distribution of I_2 directly scattered and trapped-desorbed were measured. It was found that the degree of rotational excitation depended on the scattering substrate. Their results were qualitatively consistent with those inferred from the kinetic energy distributions of Nathanson and co-workers[45][46][103][104][14] and the observations of Olander *et al*[101]. Hardly any difference was observed between the scattering off solid or liquid phase Ga, as Olander *et al* observed for three different metals.

All of the work to date in this field has focused on measuring properties of the scattered species after collision(s) with the liquid surface. In these experiments we examine the effect of the scattering on the liquid substrate. Liquid crystals are chosen since the alignment in the nematic phase may be interrogated as a result of the birefringence. The advantage to using 4′-pentyl-4-biphenylcarbonitrile (5CB) is that it has only one liquid crystal mesophase and the nematic phase in the range 22.5°C and 35.2°C[108] The loss of order of an aligned nematic phase liquid crystal 5CB caused by collisions of a gas beam is measured. The loss of order is dependent on the orientation of the liquid crystal director to the beam direction. It was found that collisions

occurring "broadside" to the alignment director are more effective in disrupting the alignment than those which occur "lengthwise". The work described here has been published as "Surface-mediated disorder in aligned liquid crystal films caused by collisions with He" in Physical Review Letters, **77**:310-313. 1996 and "Scattering of gases from aligned liquid crystals: collision-induced loss of order at the gas-liquid interface" to be published in The Journal of Chemical Physics Dec 1. 1996.

7.2 Results

In these experiments a liquid crystal sample in its nematic state is placed between two polarizers, which are mounted perpendicular to one another. Light is transmitted through the combination crossed polarizers/liquid crystal and the effect of a gas beam on the sample is measured. The liquid crystal sample is aligned with its director either perpendicular or parallel to the projection of the atomic beam axis onto the sample plane. A pulsed beam of helium is allowed to impinge on the sample for several minutes and is then shut off for several minutes. This sequence is repeated two or three times. The sample is then rotated by 90^c so its orientation is switched from perpendicular to parallel or the reverse and the sequence is repeated two or three more times. The gas pulse is typically 5 ms duration, triggered at a repetition rate of 10 Hz. The pressure in the scattering chamber rises to 2 - 3 $\times 10^{-5}$ Torr with the pulsed nozzle running and a He stagnation pressure of 1 atm.

The intensity of the light transmitted through the crossed polarizers/liquid crystal combination is not constant from day to day. The change in light transmission caused by the atomic beam also varies significantly from day to day. This makes quantitative reproducibility of the experiments nearly impossible. Over the course of several hours the amount of light transmitted through the crossed polarizer set-up often changes by 10 - 20%. This may be due to evaporative losses from the sample, buildup of impurities, or both. Even though the sample is not at equilibrium as a result of the continuous pumping, the amount of sample lost to evaporation over the course of a 3

to 4 hour experiment is less than 3% (as measured by Michel Olivier[109]). Surface contaminants are not expected to be a problem since the Nathanson[45][46][14] and McCaffery[47][105] groups found little accumulation of contaminants at the interface of other low surface energy organic liquids.

7.2.1 Sample alignment

A polarizing light microscope is used to observe the time dependence of the alignment of the liquid crystal sample. The microscope consists of two crossed polarizers between which the sample is mounted and visible light is transmitted though the combination. A sample plate with an aligned PVA coating was placed in the microscope. The nematic phase liquid crystal was added to the sample plate and the first picture, Figure 7.1a, was taken immediately. The pattern observed in this picture is that of a nematic liquid crystal which has not been aligned[49]. A nematic liquid crystal in its unperturbed state has a local alignment, but there are many small domains[49]. Over time the molecules in the individual domains begin to align with the PVA. In turn the domains coalesce as they each align with the same director, in Figure 7.1b fewer larger domains are visible. After 20-30 minutes time the different domains join into a single uniform alignment along the direction of the director, as shown in Figure 7.1c. To ensure that the sample is single domained, the sample was allowed to settle for 20-30 minutes before the experiments were begun.

Further proof of the alignment instilled by the rubbed PVA coating is the dependence of the optical signal on the temperature as shown in Figure 7.2. The temperature is varied between the crystalline-nematic transition temperature, 22.5°C, to past the nematic-isotropic transition, 35.2°C. Over this range the signal shows only a small decrease with increasing temperature up to the nematic-isotropic phase transition. Above the phase transition temperature the signal vanishes. Since the sample must be aligned in order to observe a signal in our experiments, the signal vanishes when the liquid crystal becomes isotropic.

Figure 7.1: *Photographs of the nematic-phase 5-CB sample taken through a polarizing microscope: (a) immediately after the sample is added to the sample plate containing the rubbed-PVA substrate; (b) 3 min after sample added; (c) 30 min after sample added.*

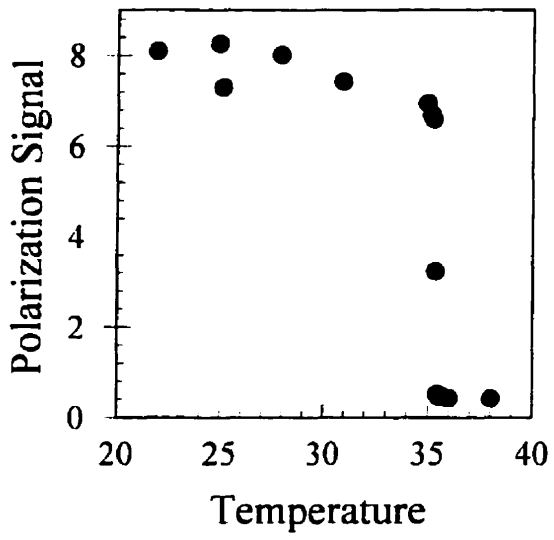

Figure 7.2: *Dependence of the liquid crystal signal on the temperature of the sample. The temperature of the sample is varied from below the crystalline-nematic transition to above the nematic-isotropic transition. Note that the signal drops sharply at the nematic-isotopic transition temperature.*

7.2.2 The effect of atomic beam on the transmission signal

Figures 7.3 and 7.4 shows representative data of the optical transmission signal as a function of time for several experiments with a gas beam of helium. The time at which the beam is turned on is indicated with an arrow, ↓, and the time at which the beam is turned off is indicated with an arrow as well as an asterisk, ↓•. The left traces show the results when the alignment is perpendicular; the right traces show the results for the parallel alignment.

The liquid crystal director was either aligned parallel or perpendicular to the component of the atom beam on the plane of the liquid crystal. In the perpendicular geometry, the transmission is always affected by the gas beam. In the parallel geometry the gas beam may or may not affect the transmission. The magnitude of the change in signal with the gas beam on is always larger for the perpendicular geometry than the parallel geometry, by a factor of 2 or more. The optical transmission either increases or decreases as a result of the gas beam turned on. No change is observed in the optical transmission for a single gas pulse. Only after several pulses is any

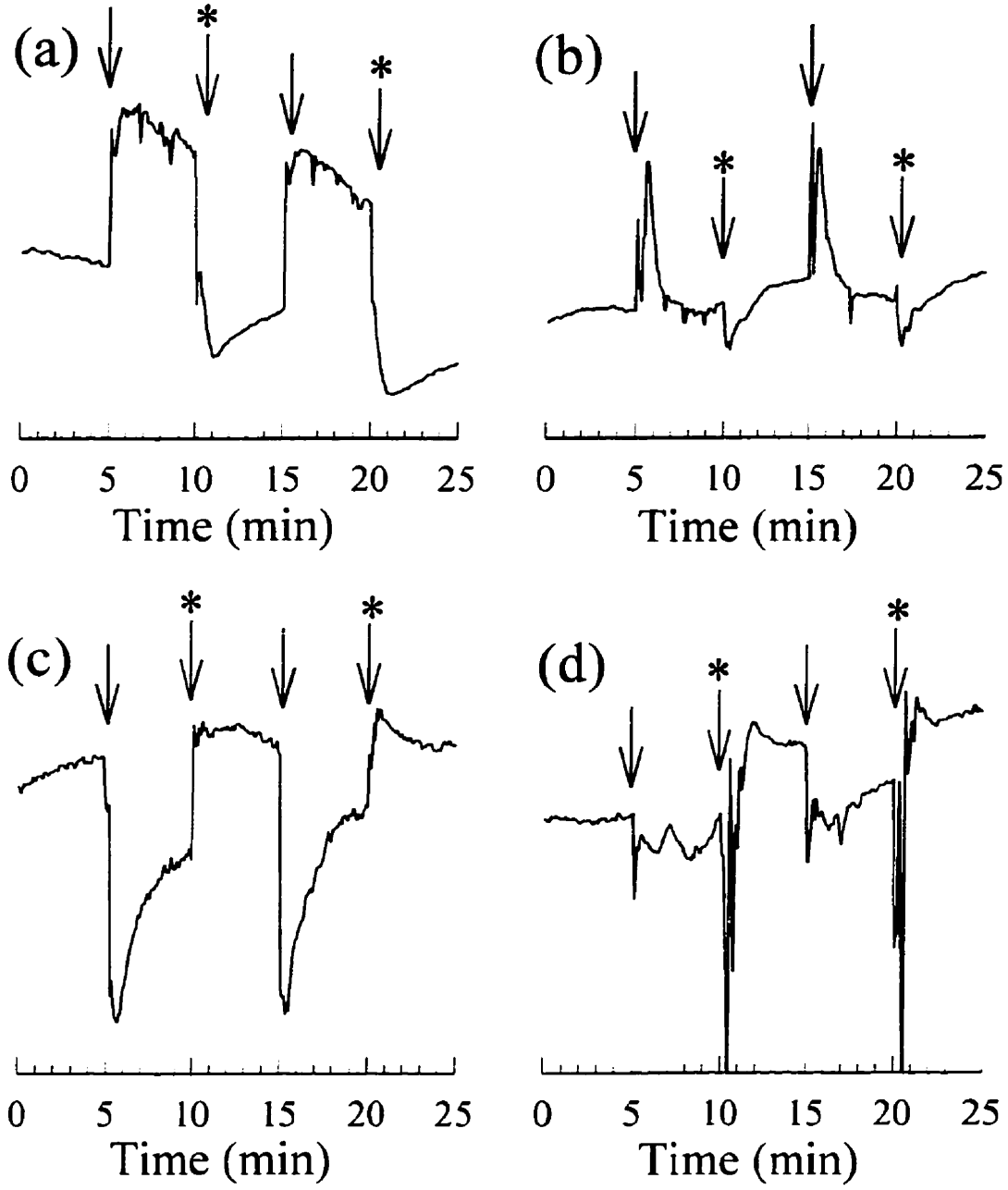

Figure 7.3: *Representative plots of the optical transmission vs. time for sample aligned perpendicular, (a) and (c), and parallel, (b) and (d), to the horizontal component of the gas beam direction. Arrows mark the times at which the gas beam is turned on and arrows with asterixes mark the time at which the gas beam is turned off. The magnitude of the change in transmission signal is ~ (10-25)%.*

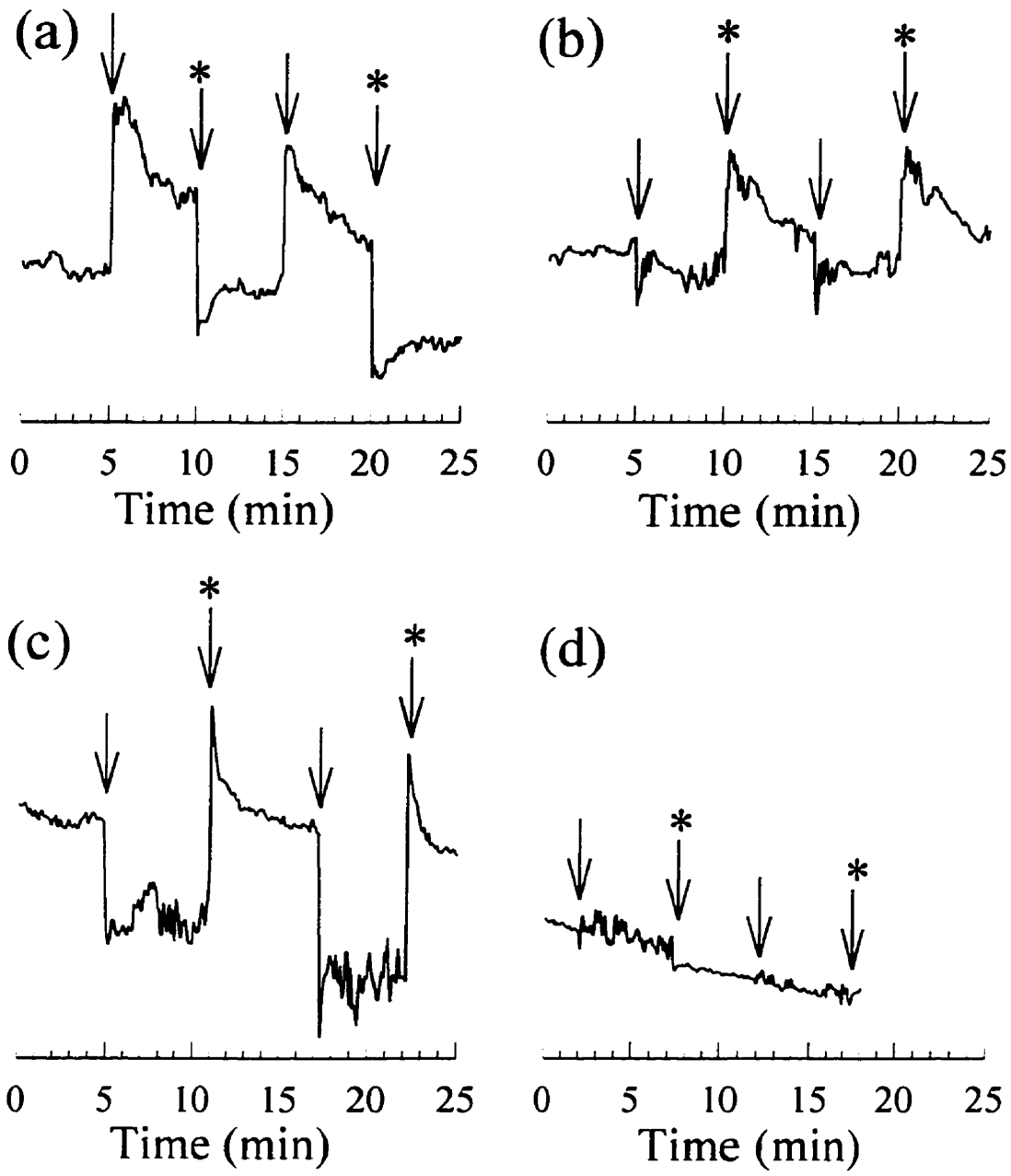

Figure 7.4: *Representative plots of the optical transmission vs. time for sample aligned perpendicular, (a) and (c), and parallel, (b) and (d), to the horizontal component of the gas beam direction. Arrows mark the times at which the gas beam is turned on and arrows with asterixes mark the time at which the gas beam is turned off.*

change in the signal observed, as well the relaxation of the signal occurs on a similar time scale.

An intense, short transient "spike" is sometimes observed in the parallel configuration signals after the beam is turned on or off, see for example Figure 7.3d. Even when an intense spike is not observed, the signals often rise (or fall) to a peak and then decay to some steady state value.

The signal increases monotonically as the pulsed beam repetition rate is varied between 1 and 25 Hz with constant pulse width (5 ms), as shown in Figure 7.5. The signal remains constant when the pulse width and repetition rate are varied as long as the duty cycle of the pulsed nozzle (pulse width × repetition rate) remains constant (see Figure 7.6). The observed signal shows no dependence on the constituent of the gas beam for the gases used here: He, Ar, N_2, and a 10% mixture of C_2H_6 in He. Figure 7.7 shows little to no difference in the effect of helium or a 10% mixture of C_2H_6 in He impinging on the surface.

The initial temperature of the liquid crystal was varied over the nematic temperature range, the resultant signal did not vary beyond the uncertainty in the measurements, as shown in Figure 7.8. When the temperature of the sample is heated above the nematic-isotropic transition, the optical transmission drops to zero. The results, displayed in Figure 7.9, showed no dependence of the wavelength of the transmitted Ar^+ light (λ = 514 or 477 nm). Early experiments with a HeNe probe laser also showed a change in the optical transmission with the gas beam on.

7.3 Discussion

This experiment exploits the birefringent property of an aligned nematic liquid crystal. The net transmission through the polarization measurement apparatus is given by (see Appendix B)

$$I = \frac{1}{4}E_0^2\left\{\cos\left(\frac{2\pi n_e d}{\lambda}\right) - \cos\left(\frac{2\pi n_o d}{\lambda}\right)\right\}^2 \tag{7.1}$$

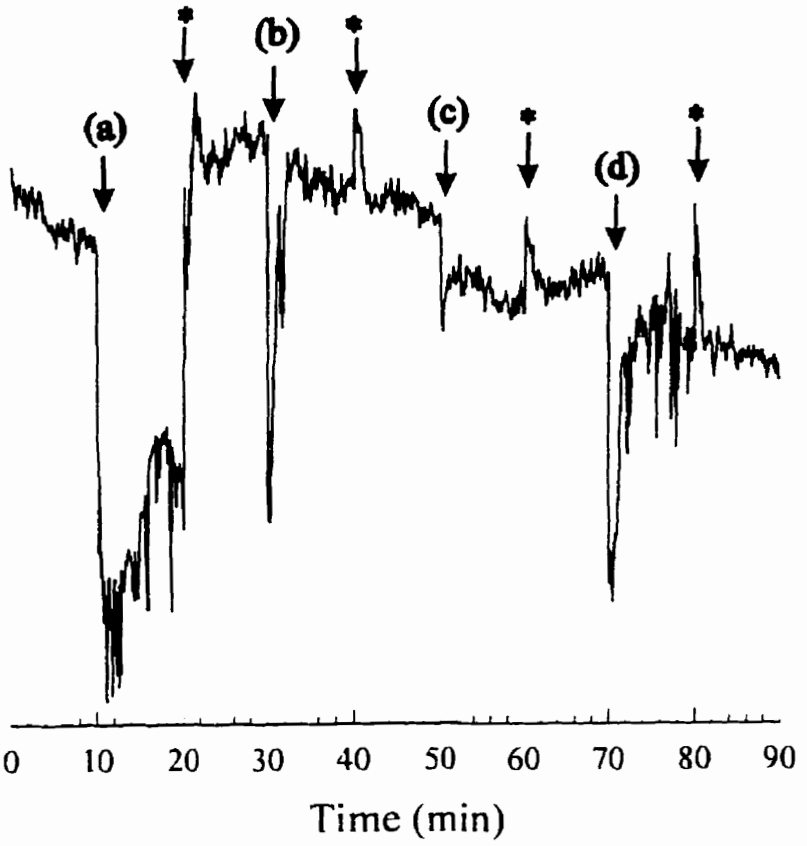

Figure 7.5: *Plot of the optical transmission vs time for the sample in the perpendicular alignment with a pulse width of 5 ms and a repetition rate of (a) 20 Hz; (b) 5 Hz; (c) 1 Hz; (d) 10 Hz.*

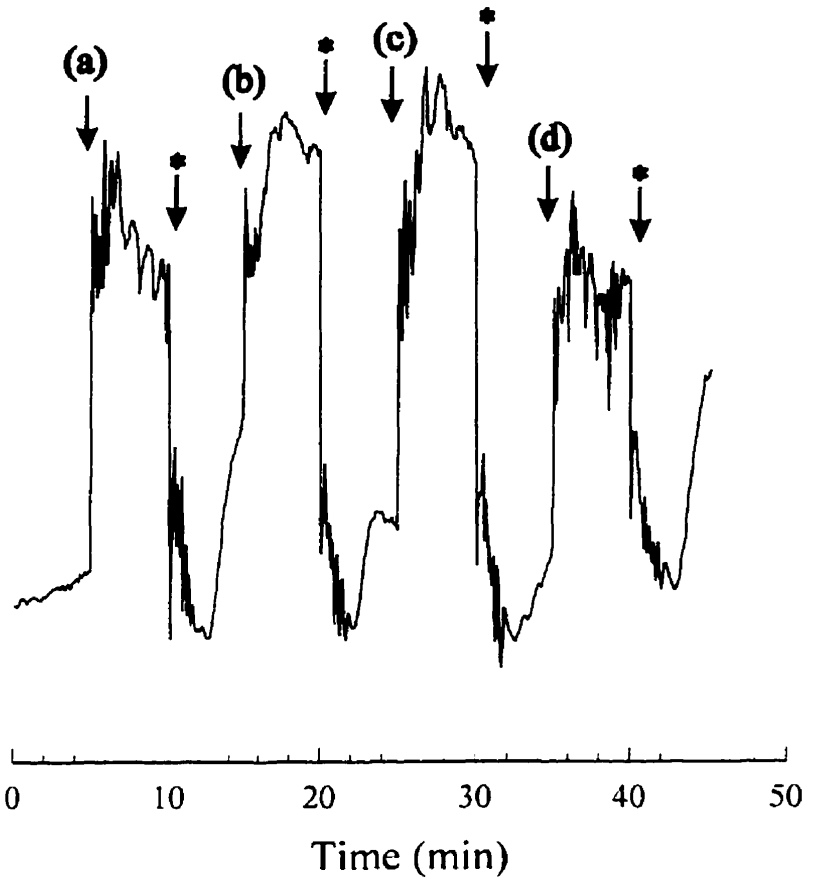

Figure 7.6: *Representative results showing the optical transmission through the sample-crossed polarizer setup as a function of time. The duty cycle remains constant, but the pulse width and repetition rate are varied: (a) 5 ms at 10 Hz, (b) 25 ms at 2 Hz, (c) 10 ms at 5 Hz, and (d) 2 ms at 25 Hz. The arrows with asterix mark times where the atomic beam is switched off.*

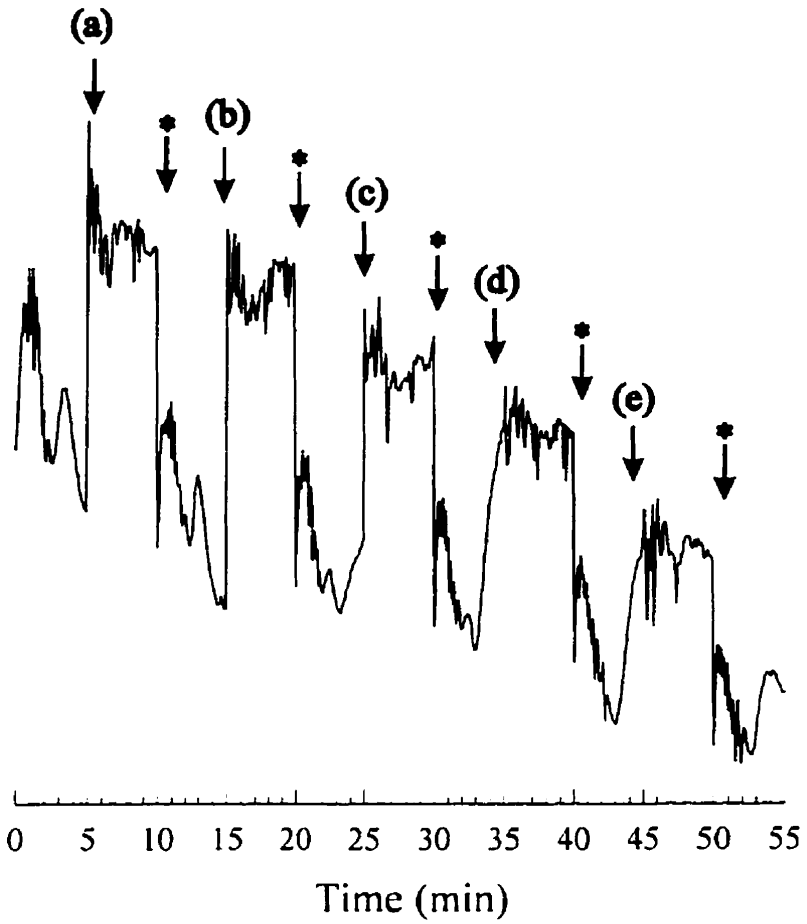

Figure 7.7: *Plot of the optical transmission vs time for samples which are impacted by He (a), (b), and (e); by 10% C_2H_6 in He (c) and (d).*

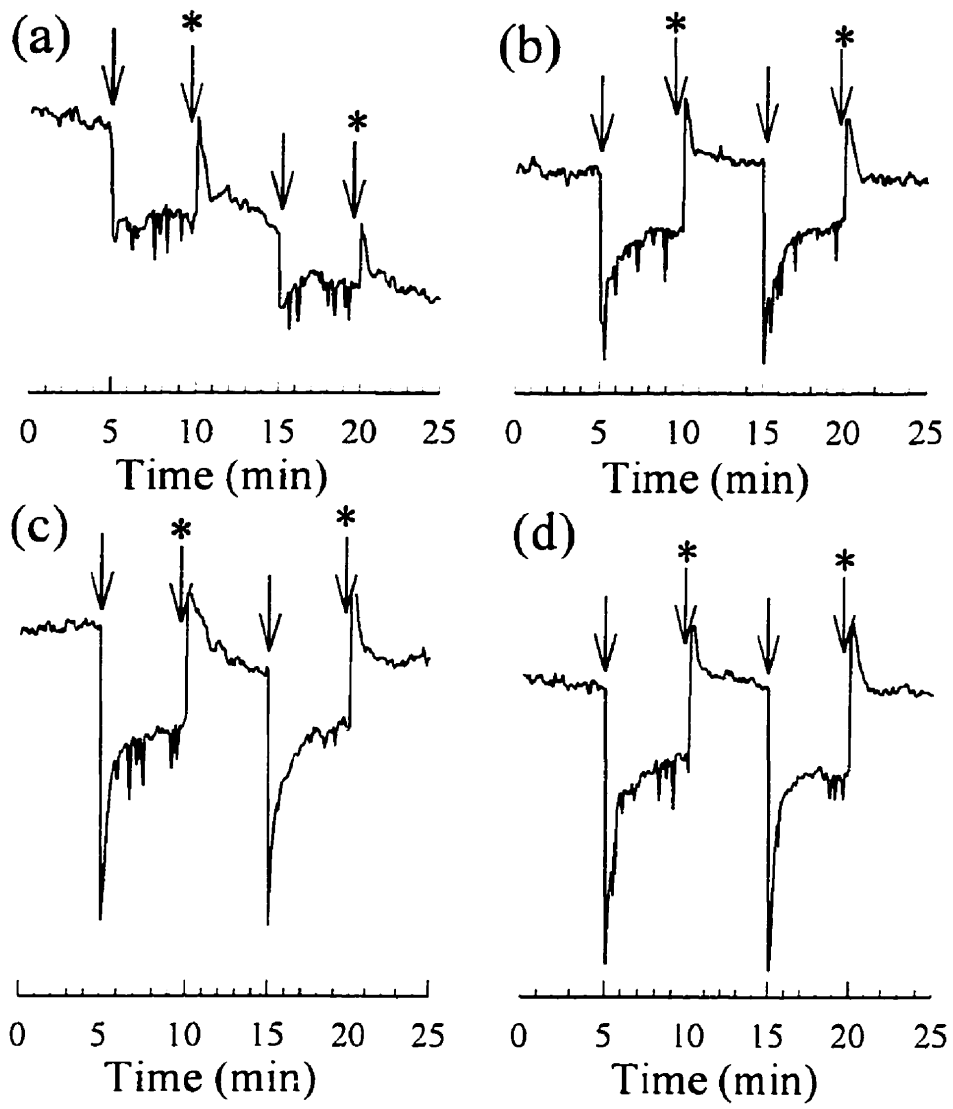

Figure 7.8: *Plots of optical transmission vs time for different temperatures (a) 26° C, (b) 28° C, (c) 30° C, and (d) 32° C,*

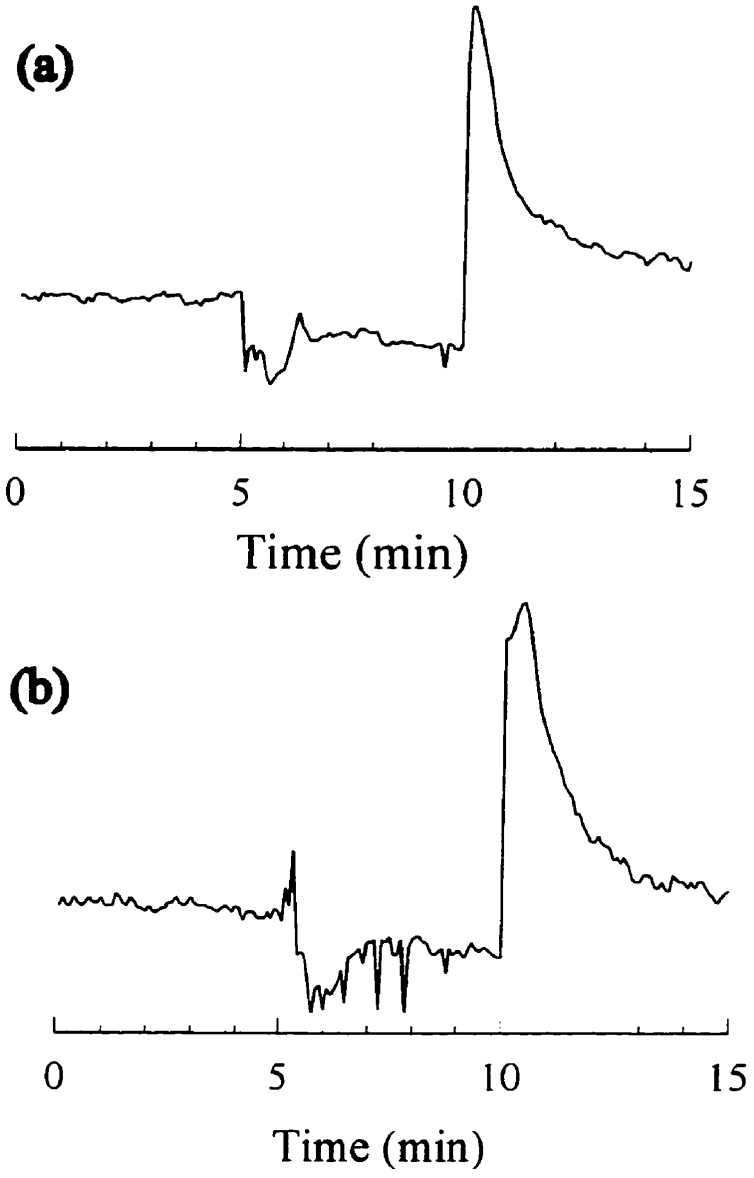

Figure 7.9: *Plots of the optical transmission signal vs time with (a) 514 nm light, and (b) 477 nm light.*

where E_0 is the electric field vector of the incident light beam, n_o and n_e are the ordinary and extraordinary indices of refraction respectively, d is the thickness of the liquid crystal film, and λ is the wavelength of the incident light. The expression for the transmission is very sensitively dependent on the thickness of the sample (see Figure B.1). The signal is the product of two oscillating functions, one with a period of 319 nm the other with a period of 6385 nm. Since no change is made to the incident light, λ and E_0 are constant and the and the only variables which affect the transmitted signal are the indices of refraction and the thickness of the sample. The indices of refraction are functions of the order parameter, the density, and the temperature.

The variation in the signal level observed with different samples depends on the exact thickness of the sample. The initial thickness of the sample makes a substantial difference in determining how large the change in signal will be when the gas beam is turned on. In these experiments it is the relative signal rather than the absolute signal which was measured. The change is signal is therefore is more appropriately expressed as a percentage change in the signal value. A change in signal of 10% is used to determine the required thickness change, since that large a change should be visible over the noise of the signal. The change in thickness of the sample required to reduce the signal by 10% has been calculated over the range 0 to 1596 nm, since the signal repeats itself after this range. In Figure 7.10 the signal and the thickness change required for a 10% signal change are compared for the range 1439 to 1516 nm, which is representative signal range. From the calculations, the average thickness change necessary to change the signal by 10% is 1.9 nm or approximately 4 layers. However, this is likely to underestimate the actual thickness change necessary to observe a signal in these experiments. From Figure 7.10, it is obvious that the larger signal levels correspond to larger sample changes to produce a 10% signal change. For example at 1440 nm thickness the signal is 0.54% of the maximum signal and the required thickness change is 0.1nm, while at 1516 nm the signal is nearly 200 times larger and a thickness change of 10.7 nm is required to observe a signal change. Since the signal for 1440 nm thickness is small, it is unlikely that any signal would be observed over the noise and hence thicknesses corresponding to small signal with

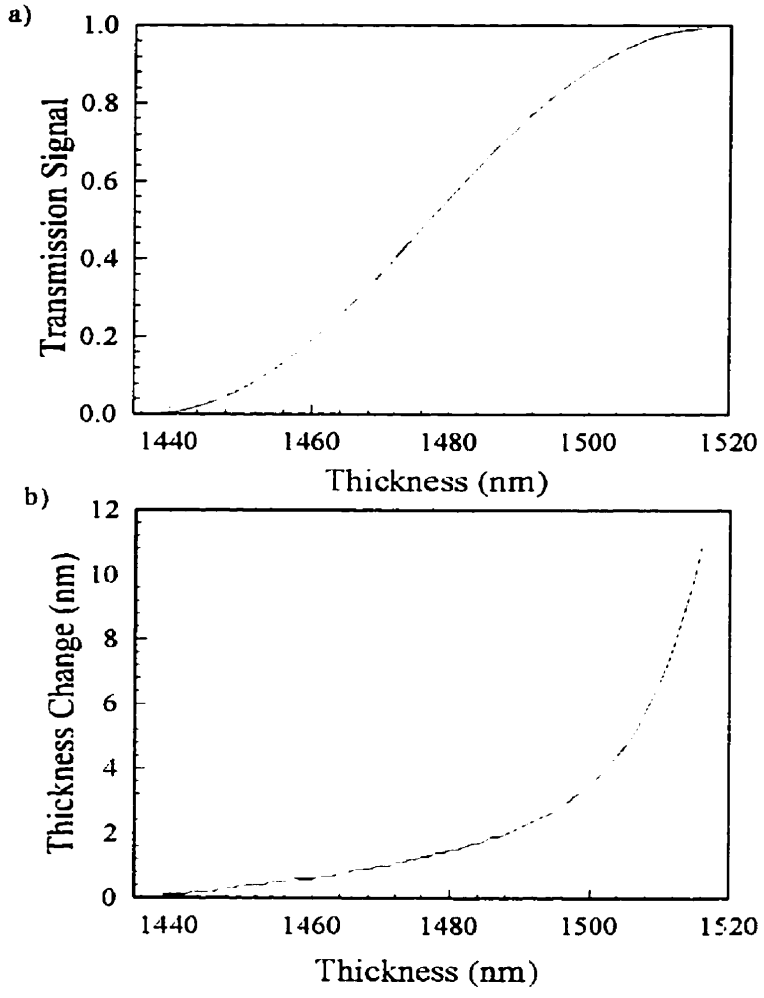

Figure 7.10: *(a) The transission of light through the polarization detection apparatus as a function of the thickness of the liquid crystal sample for the range of thicknesses 1439-1516 nm. (b) The thickness change in the sample required to change the transmission signal by 10% as a function of the thickness of the liquid crystal.*

no gas jet are unlikely to be measured. Therefore, in terms of the actual experiment the observed changes will be weighted toward larger initial signal and consequently large changes in the sample thickness. A weighted average based on the initial signal intesity for the thickness change for an observed signal is perhaps 4 nm.

A complication in analyzing the observed signal with these calculations is that both n_e and n_o are functions of the temperature. For 5CB, n_e varies from 1.72 to 1.65 and n_o varies from 1.52 to 1.54 over the nematic temperature range (see Figure 3.4). The index of refraction changes with temperature since the temperature affects the order parameter and the sample density.

The time scale in which the signal is observed is on the order of 0.1 - 1 sec. The time scale for reorientation of the nematic phase liquid crystals is on the order of 0.01 to 0.1s[110]. If the observed change in signal is the result of either changing the sample thickness or the order parameter, then the solution to Equation 7.1 will change. If the order parameter changes, this results in changing the indices of refraction. .

In order to help understand the mechanisms which could be responsible for the observed signal, we make some calculations of the energy and momentum transferred from the gas beam to the sample. The energy of the molecules in the gas beam comes from the initial thermal energy of the beam which is 6.2×10^{-21}J/molecule. The nozzle flow rate is given by

$$\dot{N} = F(\gamma)\, n_0 \sqrt{\frac{2kT_0}{m}} \left(\frac{\pi d^2}{4}\right)$$

$$F(\gamma) = \left(\frac{\gamma}{\gamma+1}\right)^{\frac{1}{2}} \left(\frac{2}{\gamma+1}\right)^{\frac{1}{\gamma-1}}$$

where the initial temperature, $T_0 = 300K$, the molecular weight, $W = 4\times10^{-3}$kg / mol, $\gamma = \frac{5}{3}$, n_0 is the number density for the gas ($= \rho_0 / m$) which for helium is $2.68 \times 10^{25}/\mathrm{m}^3$, and d is the diameter of the orifice of the gas nozzle (for the experiments described here $d = 2 \times 10^{-4}$m). From this we find the nozzle flow rate, $\dot{N}$, is equal to 4.81×10^{20}/s. In 5 ms, which is the time for a single gas pulse, the number of molecules through the nozzle is $N = \dot{N}t = 2.4 \times 10^{18}$ atoms. Therefore, the total energy per pulse is 15 mJ. The work of Nathanson and co-workers[45][46][103][104][14] suggests

that half of the kinetic energy of the beam could go into the sample. Thus, at most 7.5 mJ of energy per pulse could be transferred to the sample. If this energy exclusively goes into heating the sample then the temperature change can be determined using $\Delta H = n_{LQ} C_p \Delta T$ where ΔH is the enthalpy for constant pressure systems, n_{LQ} is the number of moles of liquid crystal, and C_p is the heat capacity. An estimate of the heat capacity of the liquid crystal to be 300 J/K-mol is made based on heat capacities for other similar molecular weight organic molecules[94]. The number of moles of liquid crystal is given by $n = \rho V/M$ where ρ is the density, $1.008 \times 10^3 \text{kg/m}^3$, the volume of the sample is 20μL, and the molecular weight is 249.36 g/mol. Then

$$\Delta T = \frac{\Delta H}{n_{LQ}\, C_p} = 0.3 \text{ K}.$$

The observed signal is not likely the result of a bulk heating of the sample. The usual temperature of the liquid crystal is 25°C, thus a temperature change of 11°C would be required to heat the sample to the nematic isotropic transition temperature. The change in the signal is observed in less than 1 sec, which corresponds to 10 gas pulses. Ten gas pulses would only be sufficient to raise the sample temperature by $\leq$ 3°C according to the above calculation. In addition, when the initial temperature of the liquid crystal was varied no change was observed in the rise time for the signal. Finally, from the temperature profile, see Figure 7.2, raising the temperature would only result in decreasing the signal which is not consistent with our results.

Although this is not enough energy to cause a bulk heating of the sample, there is certainly enough energy to locally heat the surface layers over the isotropic transition temperature. A phase change of the top layers of the sample would change the thickness of liquid crystal which is participating in the polarization retardation. An energy of 0.03 mJ would be sufficient to raise the temperature of a 10 nm layer from 22 to 36°C. This much energy is available within a single gas pulse, but despite repeated efforts no signal change was observed from a single gas pulse. In addition this method of energy deposition does not explain the observed anisotropy between the parallel and perpendicular geometry, since a local heating of the top few layers of the sample should not depend on the orientation of the molecules.

A mechanism which explains the change in the signal as well as the signal anisotropy is a purely mechanical model. The helium molecules in the gas beam may impart an alignment-breaking torque on the liquid crystal molecules at the surface. The effect of this torque would depend on whether the helium collides with the rod-like molecules "lengthwise" (parallel geometry) or "broadside" (perpendicular geometry). In the parallel geometry, the projection of the beam momentum at the surface is along the long axis of the liquid crystal. The result of this collision is expected to be an out-of-plane buckling motion of the rod like molecules. This out-of-plane buckling would produce a waving motion at the surface, but little net effect on the overall alignment. In the "broadside" collision, the projection of the beam momentum at the surface is perpendicular to the long axis of the liquid crystal. This could rotate the molecules in the plane of the surface, which would disrupt the net alignment of the sample.

Upon application of an external force, a liquid crystal will undergo a deformation[52] as will a solid. The energy to deform a liquid crystal is much lower than is needed for a solid. In Chapter 4, it was shown that the maximum for the velocity of the beam is determined by

$$V_{\max} = \sqrt{2\frac{\gamma}{\gamma - 1}\frac{R}{W}T_0}$$

For the expansions in this experiment, the gas used was helium, the initial temperature was 25°C. For these initial conditions, $V_{\max} = 1766\, m/s$. To calculate the force that a single helium atom imparts on the surface, assume that the helium impinging on the surface leaves with $V_{exit} = -V_i$, where V_i is the velocity with which it hits the surface. The force with which the gas impacts the surface is given by $|F| = m|a|$, where

$$|a| = \left|\frac{V_{exit} - V_i}{t}\right| = \left|\frac{-2V_i}{t}\right|.$$

The time for the collision is approximated to be 10 ps, which is reasonable interaction time for a binary collision. From this the force on the surface resulting from a single collision is determined to be $|F| = 2.34 \times 10^{-12}$N $= 2.34 \times 10^{-7}$dyne. This force is close the measured bulk elastic constants measured for similar liquid crystals ($\sim 10^{-6}$ dyne)[52]. Thus the impact of the gas beam could push the molecules out of alignment and a collisions induced nematic to isotropic transition would result. If several

collisions are involved the probability of this mechanism would be even more likely.

Once the molecules at the surface begin to rotate, the tendency of liquid crystal molecules to align with one another could cause other molecules to follow suit and a disruption of several layers of the liquid crystal would result after several pulses of the atomic beam. This would decrease the number of layers of the liquid crystal participating in the polarization retardation. The bulk alignment of the sample will oppose this surface initiated rotation. This would explain why no signal change is observed with a single pulse and that the signal remains relatively constant after some period of time. In order to produce an observable signal the "effective thickness" of the sample must change by on the order of 5 nm or 10 layers. Since the alignment of the liquid crystal comes about by the first layer aligning with the PVA surface grooves and subsequent layers align with lower layers, it is reasonable to assume that the rotation of the surface layer will induce rotation through a number of layers of the sample. As is shown in Figure 7.10 on average a rotation of 4 layers of sample will produce an observable signal. The recovery time scale with the beam turned off is consistent with the reorientational relaxation times of 10's to 100's of milliseconds.

An alternative explanation is that the collisions with the surface induce a flow in the upper layers. Translational motion is coupled to the inner orientational motions in liquid crystals, therefore the flow disturbs the alignment[49][111]. In isotropic phase liquid crystal this coupling has been shown to produce birefringence[66]. It is possible that "broadside" collisions are more capable than "lengthwise" collisions in transferring energy and momentum to the liquid crystal, which induces flow in the surface layers of the liquid crystal. Since this mechanism would produce signal changes by changing the "effective thickness" of the sample, it will also be highly sensitive to the exact thickness of the liquid crystal. Measurements of the energy disposal of the scattered products could increase our understanding of the mechanisms responsible for our observed signal.

Chapter 8

Conclusions

The focus of this thesis is to better understand the dynamics involved in chemical reactions occurring at a liquid surface. To this end three experiments were performed.

Firstly, the effect of solvation on the energetics of a probe species was measured. The change in the energetics of the I_2 probe molecule was observed as a function of the size of the cluster, and hence the degree of solvation. It was found that the emission observed from I_2· RG clusters upon excitation of the iodine to its ion-pair levels may be due to a charge transfer exciplex formation.

Further experiments investigated reactions following HI cluster photolysis. Our results taken together with earlier experiments performed in this group indicate that different photo-chemical processes occur in HI clusters depending on the cluster size. Our results suggest that the size of the cluster plays a role in determining the products.

Finally, the dynamics of gas molecules colliding with a liquid crystal surface were studied. Measurements of the change in the polarization retardation of a liquid crystal due to incident gas jet were made. The orientation of the liquid crystal molecules with respect to the incident beam effects the transient loss of order in the liquid crystal sample. The anisotropy may be attributed to the more efficient alignment-changing torque exerted by perpendicular collisions with the gas beam.

There are many possible extensions to this research. One interesting continuation

of this work would be studying collisions of NO molecules with liquid crystal surface. This would be particularly interesting since NO molecules scattered from the surface could be measured via REMPI spectroscopy while simultaneously measuring the change in the polarization retardation of the liquid crystal surface. Simultaneous measurements of the effect of the collision on both the impinging gas molecule and the liquid crystal surface would be very informative about the energy transfer processes occurring in this system.

Appendix A

Temperature of I_2 in clusters

A laser induced fluorescence experiment was performed to determine tThe temperature of the incident I_2 molecules in the gas beam. The experimental set-up is much like that used for the fluorescence excitation experiments. An exception was the excitation source was in this case a Nd:Yag pumped dye laser operating on Rhodamine 6G operating in the region of 591 - 596 nm with a bandwidth of 0.1 cm^{-1}. The output of the laser was directed though an aperature which reduced the beam spot size to 1mm. The beam was not otherwise focused. The total emission was measured directly with a photomultiplier tube.

Upon excitation of the iodine molecules, the total emission from I_2 for wavelengths greater than the excitation wavelength was measured as the excitation wavelength was scanned between 591 and 596 nm. The (10.0), (12.1), (14.2), (16.3), and (18.4) vibronic bands of the $B\,(^3\Pi_{0u^+}) \leftarrow X\,(^1\Sigma_g^+)$ transition in I_2 are present at 591.5 nm. The spectra collected are then replicated[78] as nearly as possible by by simulated spectra using the I_2 molecular constants from Huber and Hertzberg[112] and the J-dependent Franck-Condon factors from Tellinghuisen[113](see Figure A.1). For I_2 in helium, argon, or xenon the rotational temperature is on the order of 10 K. The vibrational temperature was dependent on the gas. For helium at 1 atm the vibrational temperature is 50 K, for argon at 1 atm: 175 K, and in xenon at 0.2 atm :200 K.

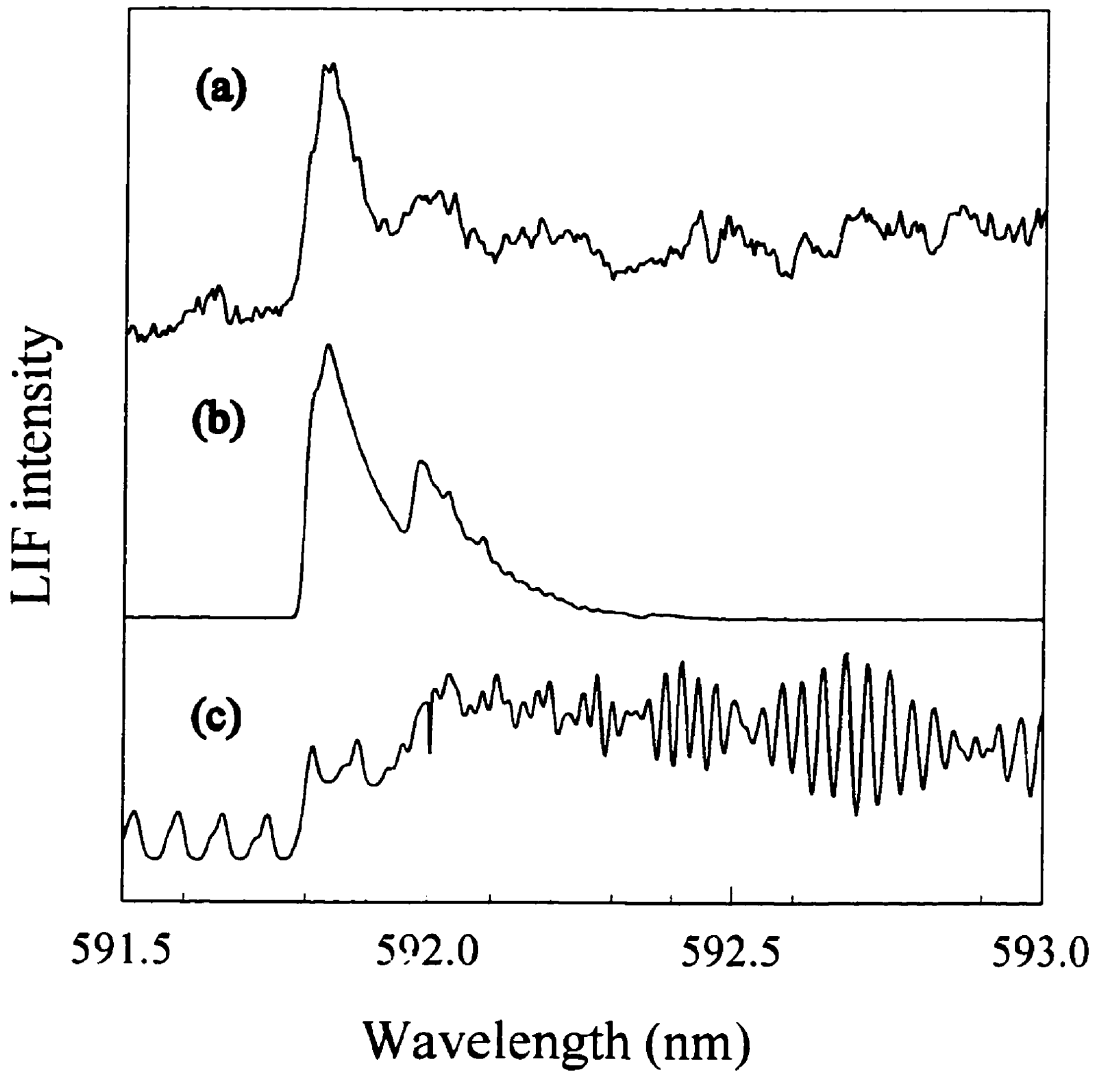

Figure A.1: *(a) LIF spectrum of I_2 in an expansion with 0.5 atm argon. (b) Simulated LIF spectrum of I_2 with T_{rot} = 15 K and T_{vib} = 150 K. (c) Simulated LIF spectrum of I_2 with T_{rot} = 300 K and T_{vib} = 300 K.*

Appendix B

Polarization measurements

The polarization measurement apparatus consists of two linear polarizers between which the liquid crystal sample is mounted. The sample is mounted so that the liquid crystal molecules are aligned either parallel or perpendicular to the incident gas beam. The polarizers are aligned orthogonal to one another and at 45° angles to the alignment direction of the liquid crystal. The x-axis is defined as the ordinary axis of the liquid crystal and the y-axis is defined by the extraordinary axis of the liquid crystals.

If the two polarizers are used without the liquid crystal, no light is transmitted if the polarizers are perfectly aligned. The liquid crystal acts as a polarization retarder, and as a result some light is transmitted through the apparatus.

The amount of light transmitted through the polarization measurement apparatus can be calculated. The intensity of light is a function of the magnitude of the electric field of the light:

$$I = \left|\vec{E}\right|^2$$

The resultant electric field of the light transmitted through the liquid crystal experiment is governed by the product of the Jones matrices for each of the individual optical elements.[48]

The transmitted light has an electric field vector $\vec{E} = Re\{E_x + E_y\}$. In matrix notation the two components of the incident electric field are given as

$$\begin{bmatrix} E_x \\ E_y \end{bmatrix} = \begin{bmatrix} E_{0x} \\ E_{0y}e^{i\varphi_y} \end{bmatrix}$$

where E_{0x} and E_{0y} are the initial x and y amplitudes of the electric field vector, and φ_y is the phase difference between these two components.

The light initial impinges on the first polarizer which is at an angle of 45° to the y-axis in the x-y plane. The transmission through this polarizer is given by the Jones matrix[48][114]:

$$\vec{T}_1 = \frac{1}{2}\begin{bmatrix} 1 & 1 \\ 1 & 1 \end{bmatrix}$$

The light transmitted through the first polarizer has an electric field of

$$\begin{bmatrix} E_x \\ E_y \end{bmatrix} = \frac{1}{2}\begin{bmatrix} E_{0x} + E_{0y}e^{i\varphi_y} \\ E_{0x} + E_{0y}e^{i\varphi_y} \end{bmatrix}.$$

The liquid crystal acts as a polarization retarder.[48] The Jones matrix for a retarder without attenuation which is aligned with the extraordinary axis on the x-axis and the ordinary axis as the y-axis is given by[48][114]

$$\vec{T}_{\text{LC.}} = \begin{bmatrix} \exp(-2\pi i n_o d/\lambda) & 0 \\ 0 & \exp(-2\pi i n_e d/\lambda) \end{bmatrix} \tag{B.1}$$

where n_o and n_e are the ordinary and extraordinary refractive indices respectively, λ is the wavelength of the incident light, and d is the thickness of the liquid crystal film. Following this element, the electric field of the light is :

$$\begin{bmatrix} E_x \\ E_y \end{bmatrix} = \frac{1}{2}\begin{bmatrix} (E_{0x} + E_{0y}e^{i\varphi_y})\exp(-2\pi i n_o d/\lambda) \\ (E_{0x} + E_{0y}e^{i\varphi_y})\exp(-2\pi i n_e d/\lambda) \end{bmatrix}$$

The final element of this apparatus is the second polarizer which is located at an angle of -45° to the y-axis in the x-y plane and has a Jones matrix given by[48][114]

$$\vec{T}_2 = \frac{1}{2}\begin{bmatrix} 1 & -1 \\ -1 & 1 \end{bmatrix}.$$

The electric field vector for the light transmitted through the polarization measurement apparatus is given by:

$$\begin{bmatrix} E_x \\ E_y \end{bmatrix} = \frac{1}{4}\begin{bmatrix} (E_{0x} + E_{0y}e^{i\varphi_y})\{\exp(-2\pi i n_o d/\lambda) - \exp(-2\pi i n_e d/\lambda)\} \\ (E_{0x} + E_{0y}e^{i\varphi_y})\{\exp(-2\pi i n_e d/\lambda) - \exp(-2\pi i n_o d/\lambda)\} \end{bmatrix}.$$

The intensity of the transmitted light is given by:

$$I = \left|\vec{E}\right|^2 = Re\left\{|E_x|^2 + |E_y|^2\right\}. \tag{B.2}$$

$$\begin{aligned} I &= Re\left\{\frac{1}{4}(E_{0x} + E_{0y}e^{i\varphi_y})^2\left[\exp\left(-\frac{i2\pi n_e d}{\lambda}\right) - \exp\left(-\frac{i2\pi n_o d}{\lambda}\right)\right]^2\left[(-1)^2 + (1)^2\right]\right\} \\ &= \frac{1}{4}E_0^2\left\{\cos\left(\frac{2\pi n_e d}{\lambda}\right) - \cos\left(\frac{2\pi n_o d}{\lambda}\right)\right\}^2. \end{aligned} \tag{B.3}$$

Using $n_e = 1.69$, $n_o = 1.53$, $E_0 = 1$, and $\lambda = 514$ nm, the light transmitted through the optical system is shows a dependence on the thickness of the liquid crystal sample given by figure B.1.

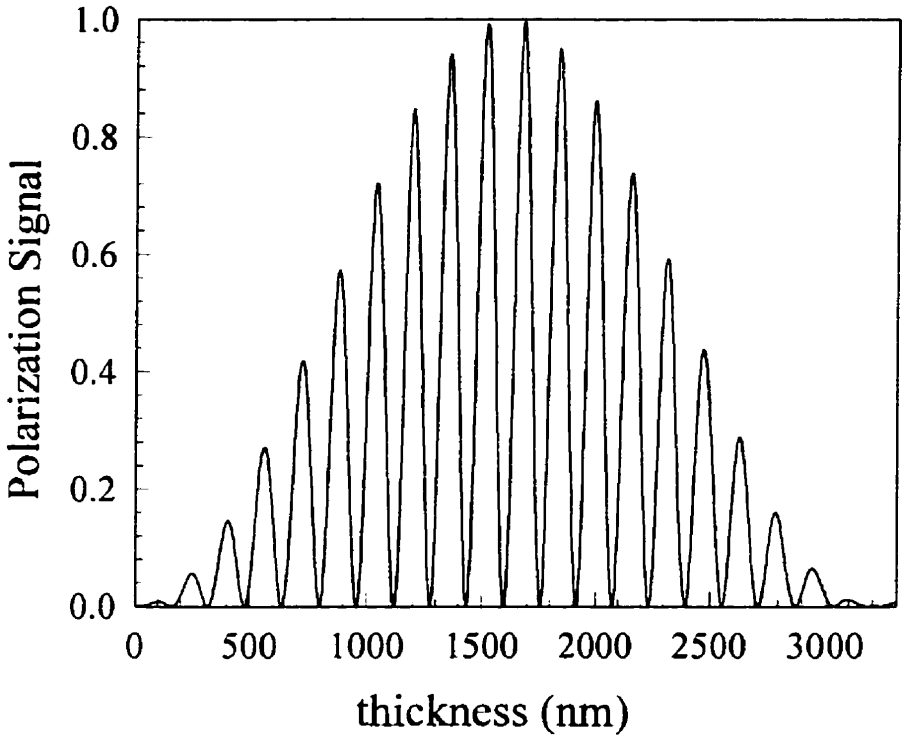

Figure B.1: *Intensity of light transmitted through the polarization measurement apparatus as a function of thickness of the liquid crystal film*

Appendix C

DKRUN

```
DECLARE SUB begin (position!, unit$, size!, grating!)
    DECLARE SUB changeGrating (grating!)
    DECLARE SUB changeSize (size)
    DECLARE SUB changeUnit (unit$)
    DECLARE SUB go (position!)
    DECLARE SUB scan (position, size)
    DECLARE SUB query (num, responce)
    DECLARE SUB unitConvert (units!, unit$)
    DECLARE SUB echo ()
    DECLARE SUB inducrap ()
    'This program is used to control the DK120 Monochromator.
    OPEN "com1:9600,n,8,1,cs1000,ds0" FOR RANDOM AS #1
    CALL begin(position, unit$, size, grating)
    choice = 0
    DO WHILE choice <> 7
    CLS
    LOCATE 3, 1, 1
    PRINT "The current position of the monochromator is "; position;
```

```
PRINT " "; unit$; "."
PRINT "The current step size is "; size; " "; unit$; "."
PRINT "The monochromator is using grating # "; grating; "."
FOR i = 1 TO 3
PRINT
NEXT i
PRINT "There are a number of operations available: "
PRINT " (1) move the monochromator"
PRINT " (2) scan the monochromator (.25 sec/step)"
PRINT " (3) change the step size"
PRINT " (4) change the units"
PRINT " (5) change the grating"
PRINT " (6) query all"
PRINT " (7) exit"
PRINT
INPUT "Which is your choice "; choice
PRINT
IF choice = 1 THEN CALL go(position)
IF choice = 2 THEN CALL scan(position, size)
IF choice = 3 THEN CALL changeSize(size)
IF choice = 4 THEN
CALL changeUnit(unit$)
CALL go(position)
CALL changeSize(size)
END IF
IF choice = 5 THEN
CALL changeGrating(grating)
CALL go(position)
CALL changeSize(size)
END IF
```

```
IF choice = 6 THEN CALL begin(position, unit$, size, grating)
LOOP
CLOSE #1
SUB begin (position, unit$, size, grating)
CALL query(0, position)
CALL query(14, units)
CALL unitConvert(units, unit$)
CALL query(6, size)
CALL query(4, grating)
END SUB
SUB changeGrating (grating)
INPUT "Which grating do you want to use"; grating
WAIT &H3FE, 16, 0
PRINT #1, CHR$(26);
WAIT &H3FE, 16, 0
PRINT #1, CHR$(grating);
message$ = INPUT$(1, #1)
END SUB
SUB changeSize (size)
INPUT "What step size do you want"; size
WAIT &H3FE, 16, 0
PRINT #1, CHR$(55);
WAIT &H3FE, 16, 0
PRINT #1, CHR$(size);
CALL inducrap
END SUB
SUB changeUnit (unit$)
PRINT "What units do you want to use¿"
PRINT " (1) nanometers"
PRINT " (2) Angstroms"
```

```
PRINT " (3) Wavenumbers"
INPUT "Which unit do you wish to use "; units
WAIT &H3FE, 16, 0
PRINT #1, CHR$(50);
WAIT &H3FE, 16, 0
PRINT #1, CHR$(units);
CALL inducrap
CALL unitConvert(units, unit$)
END SUB
SUB echo
z$ = INPUT$(LOC(1), #1)
WAIT &H3FE, 16, 0
PRINT #1, CHR$(27);
message$ = INPUT$(1, #1)
PRINT STR$(ASC(message$))
END SUB
SUB go (position)
INPUT "What position do you want to go to "; position
WAIT &H3FE, 16, 0
PRINT #1, CHR$(16);
WAIT &H3FE, 16, 0
first = INT(position / 256)
second = INT(position - 256 * first)
PRINT #1, CHR$(first); CHR$(second);
CALL inducrap
END SUB
SUB inducrap
FOR m = 1 TO 2
FOR n = 1 TO 801
crap = (1001 - n) ^ (1.23 - n * 21.2323) / m
```

```
morecrap = (42.3 ^ (3.21 - (n / 1001))) * 29.7 / (n + 21.5)
NEXT n
NEXT m
END SUB
SUB query (num, responce)
'
z$ = INPUT$(LOC(1), #1)
WAIT &H3FE, 16, 0
PRINT #1, CHR$(56);
WAIT &H3FE, 16, 0
PRINT #1, CHR$(num);
'
message$ = INPUT$(2, #1)
high = ASC(MID$(message$, 1, 1))
low = ASC(MID$(message$, 2, 1))
responce = low + 256 * high
'
CALL inducrap
'
END SUB
SUB scan (position, size)
INPUT "What do you want your starting position to be"; first
INPUT "What do you want your ending position to be"; last
PRINT "Do you want to scan from "; first; " to "; last; "(y)";
INPUT ok$
IF ok$ = "y" THEN
numStep = CINT((last - first) / size)
WAIT &H3FE, 16, 0
PRINT #1, CHR$(16);
WAIT &H3FE, 16, 0
```

```
one = INT(first / 256)
two = INT(first - 256 * one)
PRINT #1, CHR$(one); CHR$(two);
INPUT "When you want to start press return"; dummy
FOR i = 1 TO numStep
PRINT #1, CHR$(54);
CALL inducrap
NEXT i
CALL query(0, position)
END IF
END SUB
SUB unitConvert (units, unit$)
'
IF units = 1 THEN unit$ = "nm"
IF units = 2 THEN unit$ = "Angstroms"
IF units = 3 THEN unit$ = "wavenumbers"
'
END SUB
```

Appendix D

LOCKIN

```
' Simulates Chart Recorder for SR510 Lockin Amplifier.
  ' This program uses the RS232 port on the Lockin Amplifier.
  '

  'Dimension some variables and open up the com port.
  DIM CurrentDataPt, CurrentErasePt, CurrentTime, waitTime AS INTEGER
  DIM Signl(-10 TO 5000)
  OPEN "com1:9600,N,8,2,CS,DS,CD" FOR RANDOM AS #1
  PRINT #1, " "
  'This activates the F1 key so that it may be used as a trap to begin or
  ' end the program.
  KEY(1) ON
  ON KEY(1) GOSUB KeyStroke
  CLS 'clear screen
  LOCATE 5, 1
  PRINT "This program emulates a chart recorder."
  LOCATE 10, 1
  INPUT "What is the minimum signal"; yMin
  INPUT "What is the maximum signal"; yMax
```

```
INPUT "How many minutes should appear on the screen"; minuteMax
INPUT "How many seconds between data points"; waitTime
INPUT "What is the data filename"; filename$
xMax = INT(minuteMax * 60 / waitTime)
OPEN filename$ FOR OUTPUT AS #5
format$ = "#####.### #####.####"
'These values are used to allow room for a header and a footer on the screen.
ayMin = yMin - (yMax - yMin) / 10
' Make the actual yMin value (yMin - one tenth of delta y)
ayMax = yMax + (yMax - yMin) / 10
' Make the actual yMax value (yMax + one tenth of delta y)
'Open up the graphics screen.
SCREEN 12
'Define the coordinate addresses for the screen.
WINDOW (-xMax / 10, ayMin)-(xMax, ayMax)
'Draw a box on the screen.
LINE (0, yMin)-(xMax, yMax), 4, B
LINE (0, 0)-(xMax, 0), 4, , 1111
VIEW PRINT 3 TO 3
PRINT yMax;
VIEW PRINT 28 TO 28
PRINT yMin;
IF (yMax > 0) AND (yMin < 0) THEN
position = (yMax / (yMax - yMin)) * 25
' There are 25 text lines within the signal box.
zero% = INT(position + 3)
VIEW PRINT zero% TO zero%
PRINT 0;
END IF
VIEW PRINT 1 TO 2
```

```
PRINT TAB(25); "Hit the 'F1' Key to begin the program."
WHILE Ikey <> 1
WEND
CurrentDataPt = 0
StartTime = TIMER
PRINT #1, "Q"
INPUT #1, InSignal
Signl(CurrentDataPt) = InSignal * 1000
' This converts signal in volts to signal in milivolts.
Ikey = 0
VIEW PRINT 1 TO 2
PRINT TAB(25); "Hit the 'F1' Key to end the program. "
WHILE (Ikey <> 1) AND (CurrentDataPt < 5000)
' This controls the time between collecting data points.
WHILE TIMER - StartTime < waitTime
WEND
StartTime = StartTime + waitTime
' Set up some constants that will be used within this loop.
CurrentDataPt = CurrentDataPt + 1
CurrentLoop = INT((CurrentDataPt - 1) / xMax)
CurrentErasePt = CurrentDataPt + 5 - xMax
CurrentEraseLoop = INT((CurrentErasePt - 1) / xMax)
' Determine the current time.
CurrentTime = CurrentDataPt * waitTime
NumMinutes = INT(CurrentTime / 60)
NumSeconds = CurrentTime - NumMinutes * 60
' This part reads in signal from the lockin amp.
PRINT #1, "Q"
INPUT #1, InSignal
Signl(CurrentDataPt) = InSignal * 1000
```

```
' This converts signal in volts to signal in milivolts.
' Open up the file for output.
PRINT #5, USING format$; CurrentTime / 60; Signl(CurrentDataPt)
' Writes current values on the screen.
VIEW PRINT 29 TO 30
PRINT TAB(7); CurrentLoop * minuteMax; "min";
PRINT TAB(72); (CurrentLoop + 1) * minuteMax; "min"
PRINT TAB(23); "time = "; NumMinutes; "min "; NumSeconds;
"sec Signal =";
Signl(CurrentDataPt); " ";
' Draws data on the screen.
IF CurrentDataPt + 4 < xMax THEN
LINE (CurrentDataPt - 1, Signl(CurrentDataPt - 1))-(CurrentDataPt,
Signl(CurrentDataPt))
ELSE
ErasePt = CurrentErasePt - CurrentEraseLoop * xMax
CurrentDrawPt = CurrentDataPt - CurrentLoop * xMax
LINE (ErasePt - 1, Signl(CurrentErasePt - 1))-(ErasePt, Signl(CurrentErasePt)),
0
LINE (CurrentDrawPt - 1, Signl(CurrentDataPt - 1)) - (CurrentDrawPt,
Signl(CurrentDataPt))
END IF
WEND
SCREEN 0
CLOSE #1, #5
END
KeyStroke:
Ikey = 1
RETURN
```

Bibliography

[1] Geoffrey C. Maitland, Maurice Rigby, E. Brian Smith, and William A. Wakeham. *Intermolecular Forces: Their Origin and Determination.* Clarendon Press, Oxford, 1981.

[2] John Lewis Heilbron. *A History of the problems of Atomic Structure from the discovery of the electron to the beginning of Quantum Mechanics.* PhD thesis, University of California, Berkeley, Berkeley, California, 1965.

[3] Peter W. Atkins. *Physical Chemistry.* W. H. Freeman and Co., New York, fifth edition, 1994.

[4] Maurice Rigby, E. Brian Smith, William A. Wakeham, and Geoffrey C. Maitland. *The forces between molecules.* Clarendon Press, Oxford, 1986.

[5] G. Scoles. Two-body, spherical, atom-atom, and atom-molecule interaction energies. *Annual Reviews of Physical Chemistry*, 31:81–96, 1980.

[6] Ilan Benjamin, Michael A. Wilson, and Andrew Pohorille. Scattering of Ne from the liquid-vapor interface of glycerol: A molecular dynamics study. *Journal of Chemical Physics*, 100:6500–6507, 1994.

[7] Joel Tellinghuisen. The McLennan bands of I_2: A highly structured continuum. *Chemical Physics Letters*, 29:359, 1974.

[8] Joel Tellinghuisen. Resolution of an ancient spectroscopy puzzle: the D $\rightarrow$ X spectrum of I_2. *Chemical Physics Letters*, 99:373–376, 1983.

[9] M. Macler and M. C. Heaven. Spectroscopy and relaxation dynamics of metastable electronically excited states of iodine in rare gas matrices. *Chemical Physics*, 151:219–232, 1991.

[10] Mark A. Buntine, David P. Baldwin, Richard N. Zare, and David W. Chandler. Application of ion imaging to the atom-molecule exchange reaction: H + HI → H_2 + I. *Journal of Chemical Physics*, 94:4672–4675, 1991.

[11] Mark A. Young. Photochemistry of HI clusters via excitation of the first UV continuum. *Journal of Physical Chemistry*, 98:7790–7797, 199.

[12] Joseph W. Burnett and Mark A. Young. Rotational excitation as a probe of photohemistry in $(HI)_n$ clusters. *Chemical Physics Letters*, 228:403–409, 1994.

[13] Y. B. Fan, K. L. Randall, and D. J. Donaldson. Photochemistry of alkyl halide dimers. *Journal of Chemical Physics*, 98:4700–4706, 1993.

[14] Ilan Banjamin, Michael A. Wilson, Andrew Pohorille, and Gilbert M. Nathanson. Scattering of water from the glycerol liquid-vacuum interface. *Chemical Physics Letters*, 243:222–228, 1995.

[15] Sandeep Goyal, Dacid L. Schutt, and Giacinto Scoles. Molecular solvation in atomic clusters studied by means of molecular beam infrared spectroscopy. *Accounts of Chemical Research*, 26, 1993.

[16] J. Fargas, M. F. deFeraudy, B. Raoult, and G. Torchet. Noncrystalline structure of argon clusters. I. Polyicosahedral structure of Ar_N clusters, $20<N<50$. *Journal of Chemical Physics*, 78:5067–5080, 1983.

[17] J. Fargas, M. F. deFeraudy, B. Raoult, and G. Torchet. Noncrystalline structure of argon clusters. II. Multilayer icosahedral structure of Ar_N clusters, $50<N<750$. *Journal of Chemical Physics*, page 3491, 1986.

[18] O. F. Hagena and W. Obert. Cluster formation in expanding supersonic jets: effect of pressure, temperature, nozzle size, and test gas. *Journal of Chemical Physics*, 56:1793–1802, 1972.

[19] Jörg Schroeder and Jürgen Troe. Elementary reactions in the gas-liquid transition range. *Annual Reviews of Physical Chemistry*, 38:163–90, 1987.

[20] Paul B. Beeken, Eric A. Hanson, and George W. Flynn. Photochemical and photophysical dynamics of I_2 isolated in a rare gas cage. *Journal of Chemical Physics*, 78:5892–5899, 1983.

[21] Mario E. Fajardo, R. Withnall, J. Feld, F. Okada, W. Lawrence, L. Wiedeman, and V. A. Apkarian. Condensed phase laser induced harpoon reactions. *Laser Chemistry*, 9:1–26, 1988.

[22] J. Frank and E. Rabinovitch. Some remarks about free radicals and the photochemistry of solutions. *Transactions of the Faraday Society*, 30:120–131, 1934.

[23] K. Luther, J. Schroeder, J. Troe, and U. Unterberg. Pressure dependence of atom recombination and photolytic cage effect of iodine in solution. *Journal of Physical Chemistry*, 84:3072–3075, 1980.

[24] T. J. Chuang, G. W. Hoffman, and K. B. Eisenthal. Picosecond studies of the cage effect and collision induced predissociation of iodine in liquids. *Chemical Physics Letters*, 25:201, 1974.

[25] K. Luther and J. Troe. Photolytic cage effect of iodine in gases at high pressure. *Chemical Physics Letters*, 24:85, 1974.

[26] K. L. Saenger, G. M. McClelland, and D. R. Herschbach. Blue shift of iodine in solvent complexes formed in supersonic molecular beams. *Journal of Physical Chemistry*, 85:3333, 1981.

[27] James J. Valentini and Jon B. Cross. The photodissociation cage effect in van der Waals complexes: Fluorescence spectra of I_2 $B(^3\Pi_{0+u})$ from the hindered photodissociation of I_2Ar at 488 nm. *Journal of Chemical Physics*, 77:572–573, 1982.

[28] J. M. Phillippo, P. Melinon, R. Monot, and H. van der Bergh. Solvent caging by diatomic moleculesin the photodissociation of I_2M clusters. *Chemical Physics Letters*, 138:579–583, 1987.

[29] Michael L. Alexander, Nancy E. Levinger, M. A. Johnson, Douglas Ray, and W. C. Lineberger. Recombination of Br_2^- photodissociation within mass selected ionic clusters. *Journal of Chemical Physics*, 86:6200–6210, 1988.

[30] R. Naaman. Small clusters: Reactions of van der waals molecules. In *Advances in Chemical Physics*, volume 70. John Wiley and Sons, Toronto, 1988.

[31] Elliot R. Bernstein. Chemical reactions in clusters. *Journal of Physical Chemistry*, 96:10105–10115, 1992.

[32] Donald H. Levy. Supersonic molecular beams and van der Waals molecules. In R. G. Wooley, editor, *Quantum Dynamics of Molecules*. Plenum Press, New York, 1980.

[33] Phillip R. Brooks. Reactions of oriented molecules. *Science*, 193:11, 1976.

[34] C. T. Rettner and R. N. Zare. Effect of atomic reagent approach geometry on reactivity: reactions of aligned $Ca(^1P_1)$ with HCl, Cl_2, and CCl_4. *Journal of Chemical Physics*, 77:2416–2429, 1982.

[35] C. Jouvet, M. Boivineau, M. C. Duval, and B. Soep. Photochemistry in excited states of van der waals complexes. *Journal of Physical Chemistry*, 91:5416–5422, 1987.

[36] Christophe Jouvet and Benoit Soep. Photochemistry in van der waals complexes: $(Hg\text{-}H_2)^* \rightarrow HgH + H$. *Laser Chemistry*, 5:157–165, 1985.

[37] G. Radhakrishnan, S. Buelow, and C. Wittig. Orienting reactants using van der Waals precursors: $OCO{\cdot}HBr + h\nu \rightarrow (OCO \leftarrow H) + Br \rightarrow CO + OH + Br$. *Journal of Chemical Physics*, 84:727–738, 1986.

[38] S. Buelow, G. Radhakrishnan, J. Catanzarite, and C. Wittig. The use of van der Waals forces to orient chemical reactants: The H + CO_2 reaction. *Journal of Chemical Physics*, 83:444–445, 1985.

[39] R. D. Levine and R. B. Bernstein. *Molecular Reaction Dynamics*. Oxford University Press, New York, 1974.

[40] M. E. Fajardo and V. A. Apkarian. Cooperative photoabsorption induced chanrge transfer reaction dynamics in rare gas solids. i. photodynamics of localized xenon chloride exciplexes. *Journal of Chemical Physics*, 85:5660, 1986.

[41] R. Cooper, F. Grieser, and M. C. Sauer, Jr. A kinetic study of the formation of excited states in the pulse radiolysis of gaseous xenon-iodine systems. *Journal of Physical Chemistry*, 81:1889–1894, 1977.

[42] B. V. O'Grady and R. J. Donovan. Chemiluminescent reaction between I_2(D 0_u^+) and Xe to yield XeI($B^2\sigma_1/2$). *Chemical Physics Letters*, 122:503, 1985.

[43] Sidney R. Cohen, Ron Naaman, and Jacob Sagiv. Thermally induced disorder in organized organic monolayers on solid substrates. *Journal of Physical Chemistry*, 90:3054–3056, 1986.

[44] Sidney R. Cohen, Ron Naaman, and Jacob Sagiv. Translational energy transfer from molecules and atoms to adsorbed organic monolayers of long chain amphiphiles. *Physical Review Letters*, 58:1208–1211, 1987.

[45] Mackenzie E. King, Gilbert M. Nathanson, Mark A. Hanning-Lee, and Timothy K. Minton. Probing the microscopic corrugation of liquid surfaces with gas-liquid collisions. *Physical Review Letters*, 70:1026–1029, 1993.

[46] Mary E. Saecker and Gilbert M. Nathanson. Collisions of protic and aprotic gases with hydrogen bonding and hydrocarbon liquids. *Journal of Chemical Physics*, 99:7056–7075, 1993.

[47] A. J. Kenyon, A. J. McCaffery, C. M. Quintella, and M. D. Zidan. Liquid surface dynamics: a quantum resolved scattering study. *Chemical Physics Letters*, 190:55–58, 1992.

[48] B.E.A. Saleh and M.C. Teich. *Fundamentals of Photonics*. John Wiley and Sons, Inc., New York, 1991.

[49] Peter J. Collings. *Liquid Crystals: Nature's Delicate Phase of Matter*. Princeton University Press, Princeton, New Jersey, 1990.

[50] E. B. Priestley. Liquid cystal mesophases. In E. B. Priestley, Peter J. Wojtowicz, and Ping Sheng, editors. *Introduction to Liquid Crystals*, chapter 1. Plenum Press, New York, 1975.

[51] P. G. deGennes. *The Physics of Liquid Cystals*. Clarendon Press, Oxford, second edition, 1974.

[52] G. Vertogen and W. H. de Jeu. *Thermotropic Liquid Crystals, Fundamentals*. Springer-Verlag, Berlin, 1988.

[53] Peter J. Wojtowicz. Lyotropic liquid crystals and biological membranes: the crucial role of water. In E. B. Priestley, Peter J. Wojtowicz, and Ping Sheng, editors. *Introduction to Liquid Crystals*, chapter 18. Plenum Press, New York, 1975.

[54] Peter J. Wojtowicz. Introduction to the molecular theory of nematic liquid crystals. In E. B. Priestley, Peter J. Wojtowicz, and Ping Sheng, editors. *Introduction to Liquid Crystals*, chapter 3. Plenum Press, New York, 1975.

[55] Iam-Choon Khoo and Shin-Tson Wu. *Optics and Nonlinear Optics of Liquid Crystals*. World Scientific Publishing co., Singapore, 1993.

[56] R. G. Horn. Refractive indices and order parameters of two liquid crystals. *Le Journal de Physique*, 39:105–109, 1978.

[57] M. F. Vuks. Determination of the optical anisotropy of aromatic molecules from the double refraction of crystals. *Optics and Spectroscopy*, 20:361, 1966.

[58] I. Haller. Thermodynamic and static properties of liquid crystals. *Progress in Solid State Chemistry*, 10:103, 1975.

[59] Donald H. Levy. Van der Waals molecules. In *Advances in Chemical Physics*, volume 47. John Wiley and Sons, Toronto, 1982. part 1.

[60] David R. Miller. Free jet sources. In Giacinto Scoles, editor, *Atomic and Molecular Beam Methods*, volume 1. Oxford University Press, New York, 1988.

[61] H. Ashkenhas and F. S. Sherman. *The structure and utilisation of supersonic free jets in low density wind tunnels*, volume II. Academic Press, New York, fourth symposium edition, 1966.

[62] Y. B. Fan and D. J. Donaldson. Laser-induced fluorescence study of I_2 from $(CH_3I)_n$ photodissociation. *Journal of Physical Chemistry*, 96:19–21, 1992.

[63] Elizabeth Bishenden, Y. B. Fan, Nancy Andraos, Jennifer Haddock, Stephen P. Sapers, and D.J. Donaldson. Fluorescence spectroscopy of CS_2 excited near 308 nm. *Canadian Journal of Applied Spectroscopy*, 37:89, 1992.

[64] David P. Shoemaker, Carl W. Garland, and Joselph W. Nibler. *Experiments in Physical Chemistry*. McGraw Hill Publishing Co., New York, 5th edition, 1989.

[65] CVI Laser Corporation. *DIGIKROM 120 Monochromator Manual*.

[66] W. H. de Jeu. *Physical Properties of Liquid Crystalline Materials*. Gordon and Breach, New York, 1980.

[67] R. S. Mulliken. Iodine revisited. *Journal of Chemical Physics*, 55:288–309, 1971.

[68] H. Hemmati and G. J. Collins. Laser excited fluorescence of I_2. *Chemical Physics Letters*, 75:488, 1980.

[69] A. L. Guy, K. S. Viswanathan, A. Sur, and Joel Tellinghuisen. Reinterpretation of the emission spectrum of I_2 in argon. *Chemical Physics Letters*, 73:582–588, 1980.

[70] Joel Tellinghuisen. The ultraviolet laser transitions in I_2 and Br_2. *Chemical Physics Letters*, 49:485, 1977.

[71] Joel Tellinghuisen. The $D' \rightarrow A'$ transition in I_2. *Journal of Molecular Spectroscopy*, 94:231, 1982.

[72] Joel Tellinghuisen and L. F. Phillips. Kinetics of I_2 following photolysis at 1930 Å: Temperature dependence of A′-state quenching. *Journal of Physical Chemistry*, 90:5108–5120, 1986.

[73] S. Fei, X. Zheng, M. C. Heaven, and Joel Tellinghuisen. Spectroscopy and relaxation dynamics of I_2Ar_n clusters. geminate recombination and cluster fragmantation. *Journal of Chemical Physics*, 97:6057–63, 1992.

[74] Xiaonan Zheng, Suli Fei, Michael Heaven, and Joel Tellinghuisen. Spectroscopy of metastable species in a free-jet expansion: The $D' \leftarrow A'$ transition of I_2. *Journal of Chemical Physics*, 96:4877–83, 1992.

[75] Kenneth P. Lawley and Robert J. Donovan. Spectroscopy and electronic structure of ion-pair states. *Journal of the chemical Society Faraday transactions*, 89:1885–1898, 1993.

[76] A. R. Hoy and R. H. Lipson. Reinvestigation of the Cordes band system of I_2 using a vacuum ultraviolet laser. *Chemical Physics*, 140:187–193, 1990.

[77] J. C. D. Brand and A. R. Hoy. Multiphoton spectra and states of halogens. *Applied Spectroscopy Reviews*, 23:285–328, 1987.

[78] Y. B. Fan and D. J. Donaldson. Cluster-induced photochemistry of CH_3I at 248 nm. *Journal of Chemical Physics*, 97:189, 1992.

[79] Myran C. Saueer, Jr., William A. Mulac, Ronald Cooper, and Franz Grieser. Fast excited state formation and decay in the pulse radiolysis of gaseous argon-iodine systems. *Journal of Chemical Physics*, 64:4587–91, 1976.

[80] A. B. Callear, P. Erman, and J. Kurepa. The D state lifetime and the UV laser action of molecular iodine. *Chemical Physics Letters*, 44:599, 1976.

[81] P. Gurtler, H. Kunz, and J. LeCalve. Vacuum ultraviolet spectroscopy of the Cl_2 molecule trapped in pure neon, pure argon, or mixed neon-argon matrices. *Journal of Chemical Physics*, 91:6020, 1989.

[82] W. Lawrence, F. Okada, and V. A. Apkarian. Experimental studies on photodissociation of HI in crystalline xenon. *Chemical Physics Letters*, 150:339, 1988.

[83] F. Okada, L. Wiedeman, and V. A. Apkarian. Photoinduced harpoon reactions as a probe of condensed-phase dynamics: ICl in liquid and solid xenon. *Journal of Physical Chemistry*, 93:1267, 1989.

[84] F. Okada and V. A. Apkarian. Electronic relaxation of Xe_2Cl in gaseous and supercritical fluid xenon. *Journal of Chemical Physics*, 94:133, 1991.

[85] D. Golomb, R. E. Good, and R. F. Brown. Dimers and clusters in free jets of argon and nitric oxide. 52:1545–1551, 1970.

[86] P. Jeffrey Hay and Thom. H. Dunning, Jr. The covalent and ionic states of the xenon halides. *Journal of Chemical Physics*, 69:2209, 1978.

[87] M. L. Burke and W. Klemperer. The one-atom cage effect: continuum processes in I_2-Ar below the B state dissociation limit. *Journal of Chemical Physics*, 98:1797–1809, 1993.

[88] A. Garcia-Vela, P. Villarreal, and G. Delgado-Barrio. Structure and dynamics of small $I_2...He_2$ van der waals clusters (n=1-9). *Journal of Chemical Physics*, 92:6504–6513, 1990.

[89] Joel Tellinghuisen. The D state of I_2: Analysis by quantum simulations of bound-free D $\rightarrow$ X fluorescence. *Canadian Journal of Physics*, 62:1933–40, 1984.

[90] Peteer Kruus. *Liquids and Solutions*. Marcel Dekker, New York, 1977.

[91] M. L. Klein and J. A. Venables. *Rare Gas Solids*. Academic Press, London, 1977.

[92] V. Vaida, D. J. Donaldson, S. P. Sapers, R. Naaman, and M. S. Child. Spectroscopic probe of intramolecular predissociation dynamics in clusters. *Journal of Physical Chemistry*, 93:513–520, 1989.

[93] G. A. Cook. *Argon, Helium, and the Rare Gases*. volume 1. Wiley (Interscience), New York, 1961.

[94] R. C. Weast, editor. *CRC Handbook of Chemistry and Physics*. C. R. C. Press, Boca Raton, 67th edition, 1986.

[95] Y. Hannachi and B. Silvi. Structure and bonding of hydrogen halide complexe: an ab initio calculation of the 1:1 species. *Journal of Molecular Structure*, 200:483–496, 1989.

[96] C. C. Cho, J. C. Polanyi, and C. D. Stanners. Bimolecular photoreaction of adsorbates: $2HX \rightarrow H_2 + X_2$ (X = Cl, Br). *Journal of Chemical Physics*, 90:598–600, 1989.

[97] Roald Hoffman. Transition state for the hydrogen-iodine and hydrogen exchange reactions. *Journal of Chemical Physics*, 49:3739–40, 1968.

[98] Gerhard Hertzberg. *Molecular Spectra and Molecular Structure*, volume 1. Krieger Publishing Co., Malabar, Florida, 1950.

[99] Charlotte E. Moore. Atomic energy levels. circular 467, National Bureau of Standards, Washington, DC, May 1958.

[100] Rainer Bohling, Jürgen Langen, and Ulrick Schurath. A $\rightarrow$ X and a' $\rightarrow$ x' progressions in dissociative excitation of matrix-isolated I_2: rare gas effects on lifetimes and intensities. *Chemical Physics*, 130:419, 1989.

[101] D. R. Olander, M. Balooch, and W. J. Siekhus. Reactions of chlorine with liquid metals. 4. tin. *Journal of Physical Chemistry*, 90:4397–4402, 1986.

[102] Sidney R. Cohen, Ron Naaman, and Jacob Sagiv. Rotational and state-resolved translational distributions of NO scattered from organized amphiphilic monolayers. *Journal of Chemical Physics*, 88:2757–2763, 1988.

[103] N. Lipkin, R. B. Gerber, N. Moiseyev, and G. M. Nathanson. Atom scattering studies of liquid structure and dynamics: collisions of xe with a model of squalane. *Journal of Chemical Physics*, 100:8408–8417, 1994.

[104] Steven T. Govoni and Gilbert M. Nathanson. Exploring the fate of water molecules striking concentrated sulfuric acid: scattering versus solvation. *Journal of the American Chemical Society*, 116:779–780, 1994.

[105] A. J. Kenyon, A. J. McCaffery, C. M. Quintella, and M. D. Zidan. Dynamics of the gas/liquid interface from laser molecular beam scattering. *Faraday Discussions*, 96:245–254, 1993.

[106] F. C. Hurlbut and D. E. Beck. U. C. Engineering project report. Technical Report HE-150-166, University of California, 1959.

[107] M. Sinha and J. B. Fenn. *Symposium International on Molecular Jets*, 5, 1975.

[108] D. A. Dunmur and A. E. Tomes. Molecular properties of pentyl-cyano mesogens having different core structures. *Molecular Crystals and Liquid Crystals*, 97:241–253, 1983.

[109] Olivier Michel, private communication.

[110] I. C. Khoo. *Liquid Crystals*. John Wiley and Sons, Inc., New York, 1995.

[111] Brian C. Benicewicz, Julian F. Johnson, and Montgomery T. Shaw. Viscosity behavior of liquid crystals. *Molecular Crystals and Liquid Crystals*, 65:111–132, 1981.

[112] K. P. Huber and G. Hertzberg. *Molecular Spectra and Molecular Structure*, volume 4. Van Nostrand Reinhold, New York, 1979.

[113] Joel Tellinghuisen. Intensity factors for the I_2 B $\leftrightarrow$ X band system. *Journal of Quantitative Spectroscopy and Radiative Transfer*, 19:149, 1978.

[114] David S. Kliger, James W. Lewis, and Cora E. Randall. *Polarized Light in Optics and Spectroscopy*. Axademic Press, Inc., Toronto, 1990.

IMAGE EVALUATION
TEST TARGET (QA-3)

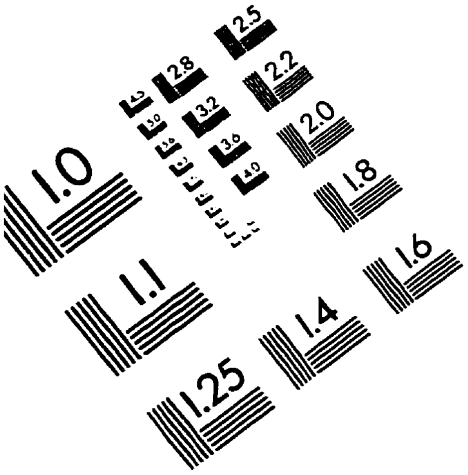

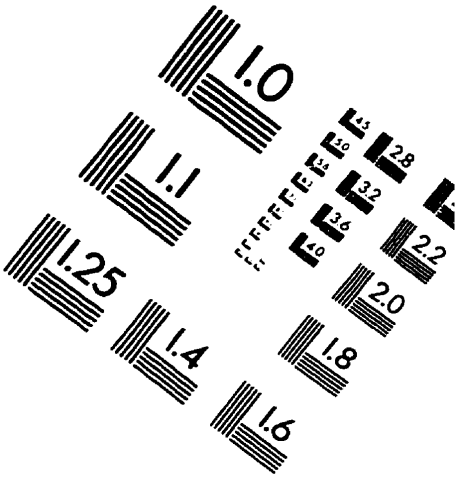

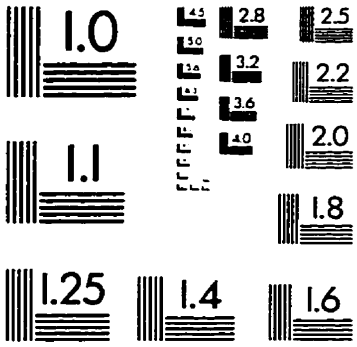

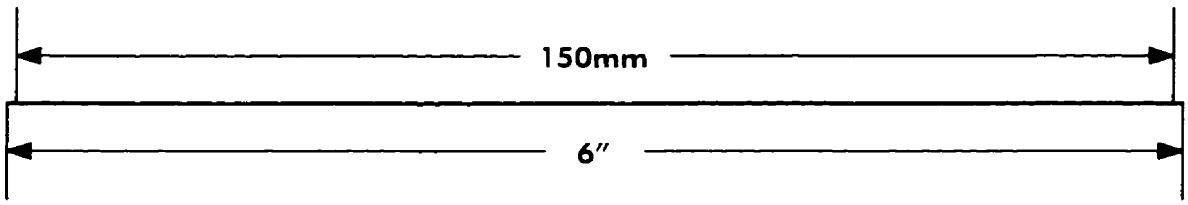

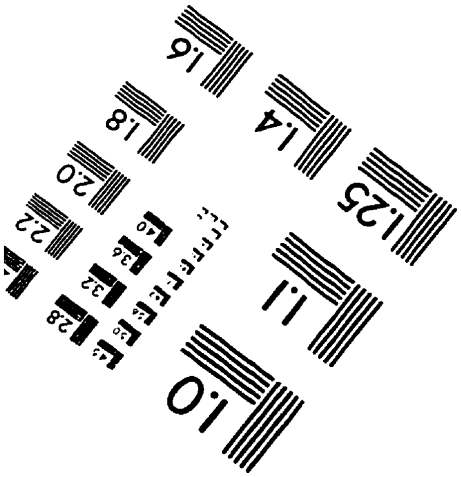

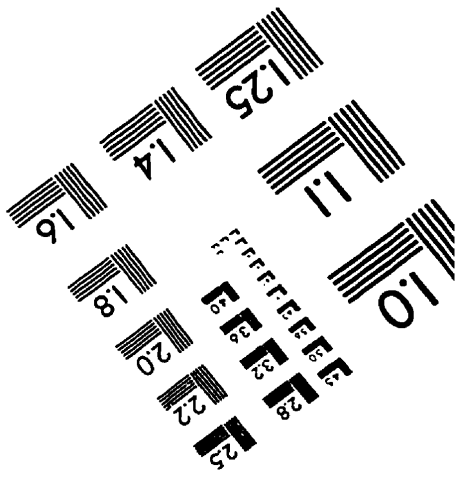

APPLIED IMAGE . Inc
1653 East Main Street
Rochester, NY 14609 USA
Phone: 716/482-0300
Fax: 716/288-5989